NUMERICAL SIMULATION OF ATMOSPHERIC THERMAL TIDES WITH A GENERAL CIRCULATION MODEL

by

Isamu Yagai

January 1991

Acknowledgements

The author wishes to express his sincere gratitude to Professor Susumu Kato for his interest and encouragement in this research and for the careful reading of the manuscript.

The author acknowledges his indebtedness to Professor Shoichiro Fukao, who invited him to attend [FY86 RASK, the First MU Radar] joint symposium took place at Kyoto University from April 19-20, 1986, where stimulating discussions provided useful insight.

The author thanks Dr. Takehiko Aso who provided the simulated results of atmospheric tides, and Dr. Toshitaka Tsuda for useful discussions.

Special thanks are due to Professor Robert Cess and Dr. Gerald Potter who invited the author to join the DOE (Department Of Energy) General Circulation Model Intercomparison. Discussions with Drs. Jean-Pierre Blanchet, David Randall and Lawrence Gates are especially useful to improve the Meteorological Research Institute General Circulation Model (MRI GCM). The author would like to thank Professor Jeffrey M. Forbes for his interest and useful comments.

The author wishes to acknowledge Drs. Tatsushi Tokioka, Koji Yamazaki and the members of the research group who participated in the construction and development of the MRI GCM.

Computations are made with the HITAC M280D, S810/10, of the MRI.

Abstract

The aim of atmospheric general circulation models (GCMs) is to simulate earth's atmosphere and exploit it for long-range prediction. If all relevant physical processes are correctly represented, then a GCM should provide a faithful simulation of the three dimensional circulation in the atmosphere. Therefore, the GCM can be used as an *experimental tool* in atmosphere research to test the adequacy of our understanding of various physical processes. A general circulation model has been developed at the Meteorological Research Institute (MRI GCM) to simulate climate of the earth's atmosphere and study climatic variations. To enhance the activities of the project, the supercomputer system is installed in the Meteorological Research Institute: HITAC M-280D as a global processor and S-810/10 a local processor. The S-810/10 has several characteristics to realize high performances in hardware and software systems: parallel pipeline processing and a high level of vectorization for programs.

The MRI GCM has twelve vertical layers (corresponding approximately to 1.39, 2.68, 5.18, 10.0, 19.3, 37.3, 72.0, 150, 300, 500, 700, and 900 mb) with the top level at 1 mb, and a horizontal resolution of 5° in longitude by 4° in latitude. The solar radiation incident at the top of the model atmosphere has both seasonal and diurnal variations. The solar flux under cloudless condition is depleted by ozone and water vapor absorption. Ozone prediction is based on a simplified photochemical model that includes Chapman reactions and the $NO\text{-}NO_2$ catalytic cycle in the stratosphere above 100 mb. The albedo of the earth's surface is determined diagnostically by the model as a simple function of surface conditions. Clouds are generated in the model and interact with radiation. Water vapor, ozone and carbon dioxide absorb and emit longwave radiation; however, above 10 mb, the longwave radiational cooling is calculated by a simple "Newtonian cooling type" parameterization. . The model includes the earth's topography. The distribution of sea surface temperature and sea ice are prescribed based on climatological data. Surface fluxes of sensible heat, water vapor and momentum are calculated by the bulk method. Ground temperature, snow depth and ground wetness are predicted in the model. The time step is 7.5 min. and all the physical processes are calculated at one hour intervals.

The 12 layer version of the MRI GCM had a serious westerly biases; the westerly jet in the stratosphere is too strong and the Aleutian low in the troposphere is too deep. The deficiency was mainly overcome by incorporating gravity wave drag in the northern hemisphere at middle to high latitudes, while almost the same in the southern hemisphere where land area is small compared to the northern hemisphere. The polar night jet is well separated from the mid-latitude tropospheric jet, and the lower stratospheric temperature around the 70 mb level at high latitudes rises up to about 10°K. Moreover, stratospheric sudden warmings appeared in the simulation, which have the same characteristics as the observation.

Non-migrating thermal tides, which do not move in synchrony with the sun, are detected in the analyses of FGGE (First GARP Global Experiment) Level IIIb data during the special observation period (SOP-1) of 10 January-9 February 1979. First is the westward moving diurnal mode with the zonal wavenumber five, and the second a eastward moving diurnal mode with the zonal wavenumber three. These modes are closely related to the wavenumber four of topography at low latitudes and have clear peaks in the space-time power spectra in the sea level pressure field. A maximum value of 0.2 mb is the same with both modes as expected from the theory, while maximum values of the background diurnal and semi-diurnal migrating modes are 0.6 mb and 1.2 mb, respectively. These non-migrating modes are essentially the same that Tokioka and Yagai [1987] reported in their analysis of GCM simulation in January.

By comparing FGGE IIIb data analysis and the Meteorological Research Institute (MRI) GCM-I simulation, diurnal and semi-diurnal migrating modes are simulated well in the sea level pressure field and relatively well at the lower troposphere in the geopotential field. The simulated non-migrating modes have horizontal structures similar to those observed in the sea level pressure field which is the most reliable data and based on a large enough number of observations to detect these modes. In the geopotential field, horizontal structure of the non-migrating modes is identified in the troposphere at low latitudes by simulation and observation.

Contents

List of Figures

List of Tables

Chapter 1

General Introduction

1.1 The general circulation of the atmosphere

The earth's atmosphere is full of various scale of waves in time or space. The general circulation of the atmosphere is usually considered to consist of motions that characterize the global scale atmospheric flow. Historically the zonally averaged circulation, that is, the latitude-height distribution of winds, temperatures, and other climatic elements are investigated from theoretical and observational viewpoint. In the eighteenth century, George Hadley noticed a zonally symmetric overturning in which the heated equatorial air rises and moves poleward where it cools, sinks, and moves back to equatorward; owing to the Coriolis force, the trade wind appears near the surface at low latitudes. However, in the earth's atmosphere, the Hadley circulation is not possible, that is, a zonal symmetric Hadley circulation is baroclinically unstable and disturbances are dominant in the actual atmosphere. This type of circulation can be seen in the zonally averaged field at low latitudes and now called a Hadley circulation. The feature of the general circulation is then developing in the following way [*e.g.*, Holton, 1975, 1979].

The fundamental process driving the earth's atmosphere is the heating by incoming shortwave solar radiation and the cooling by infrared longwave radiation to space by the planet. However, the solar heating is strongly dependent on latitude with a maximum at the equator and a minimum at the poles, especially at the winter pole. The outgoing longwave radiation, on the other hand, is weakly latitude dependent. As a result, there is a radiation excess in the equatorial region and a deficit in the polar region. The latitudinal gradient of heating drives currents in the atmosphere and ocean.

Figure 1.1 shows the overall radiation and heat balance of the atmosphere. The bulk of the net incoming solar radiation is absorbed not only by the atmosphere but underlying surface, which is in turn transfer to the atmosphere by the evaporation of moisture and the sensible heat flux from the surface. As shown in the figure, the latent

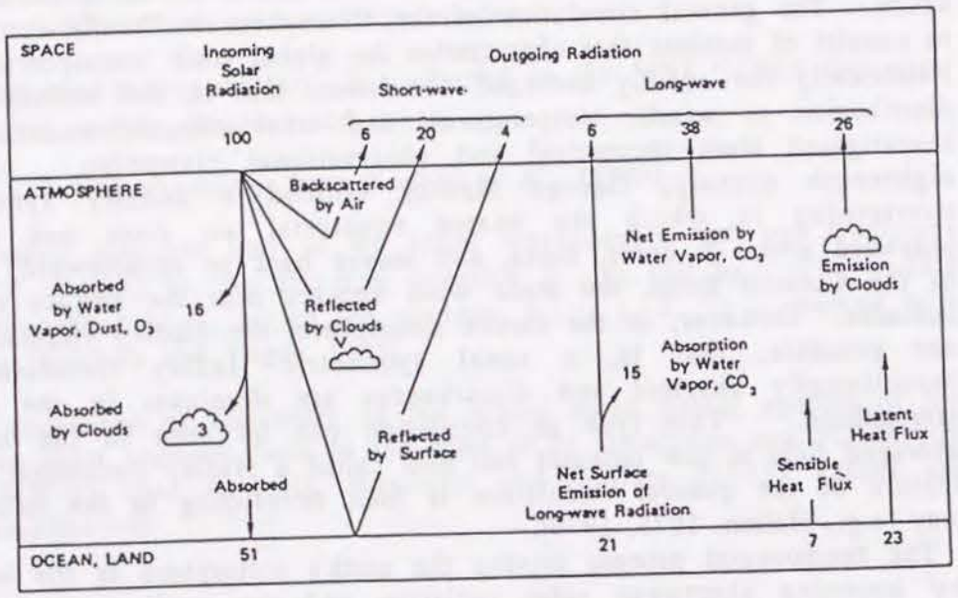

Figure 1.1: The mean annual radiation and heat balance of the atmosphere, relative to 100 units of incoming solar radiation [US National Academy of Sciences, 1975].

heat release is dominant in the direct heating of the atmosphere, especially in the tropics by the deep cumulus convection (qualitative estimate of heating profile from the observation is very difficult, however, the result by the general circulation model is presented in figure 3.6). The differential heating causes a pole to equator temperature gradient, then produces zonal wind. This relation can be described by the notation *geostrophic wind* v_g. If we assume that forcings acting on the atmosphere are comprised of the pressure gradient force, gravitation, and friction, we can write Newton's second low in a rotating system as

$$\frac{dv}{dt} + fkxv + \frac{1}{\rho}\nabla p = g + F, \qquad (1.1)$$

where f is the vertical component of Coriolis vector ($=2\Omega\sin\phi$), Ω is the angular velocity of the earth, ϕ the latitude, **k** the vertical unit vector, g gravitation, ρ the air density, p the pressure, and **F** is the frictional force. We can estimate each term in (1.1), in which for mid latitude synoptic scale disturbances the Coriolis force and the pressure gradient force are in approximate balance. Therefore, retaining only these two terms in (1.1), we obtain as a first approximation the *geostrophic* relationship

$$fkxv_g = -\frac{1}{\rho}\nabla p, \qquad (1.2)$$

or in components as

$$fv_g = -\frac{1}{\rho}\frac{\partial p}{\partial x}, \qquad fu_g = -\frac{1}{\rho}\frac{\partial p}{\partial y}, \qquad (1.3)$$

Thus, the large scale flow at mid latitudes are approximately determined by the pressure distribution. The geostrophic wind relation can be further extended. By estimating the last term in (1.1), hydrostatic relationship will turn out to be a good approximation for large scale motion. With the aid of the ideal gas law we can write the hydrostatic equation as

$$\frac{\partial\phi}{\partial p} = -\frac{1}{\rho} = -\frac{RT}{p}, \qquad (1.4)$$

Differentiating (1.2) with respect to pressure and applying (1.4) we obtain

$$\frac{\partial v_g}{\partial \ln p} = -\frac{R}{f}kx(\nabla_p T), \qquad (1.5)$$

or in components as

$$\frac{\partial v_g}{\partial \ln p} = -\frac{R}{f}\left(\frac{\partial T}{\partial x}\right)_p, \qquad (1.6)$$

$$\frac{\partial u_g}{\partial \ln p} = \frac{R}{f}\left(\frac{\partial T}{\partial y}\right)_p. \qquad (1.7)$$

The equation (1.5) is often referred as the *thermal wind* equation, which is actually a relationship for the vertical wind shear. Rigorously the term thermal wind refers to the vector difference between the geostrophic wind at two levels.

Figure 1.2 shows a schematic cross sections of the zonally averaged temperature at the solstices (the corresponding observations from the surface to 1 mb level for zonal wind and temperature for January 1983 are shown in Figures 3.3 and 3.4, respectively). The mean vertical temperature profile can be divided into three distinct layers: *troposphere, stratosphere, and mesosphere*, respectively. The troposphere accounts for more than 80% of the mass and almost all of water vapor, clouds, and precipitation in the atmosphere. The temperature generally decreases with height, a lapse rate of about 6°K/km, in this region. The thermal structure of the troposphere is maintained by a balance between infrared radiative cooling, vertical transport of sensible heat and latent heat by small scale convection and large scale heat transport by synoptic scale eddies. Planetary waves are forced in the troposphere and propagate into the stratosphere and main energy source of large scale disturbances lies in the troposphere. Therefore, when we construct a numerical model of the entire earth's atmosphere, the roll of the troposphere is quite important and the modeling has to be very complex. The transition from the troposphere to the stratosphere is usually associated with an abrupt change in the concentrations of some of the variable trace constituents; water vapor decreases sharply while ozone concentration often increases by an order of magnitude within the first few kilometers above the troposphere. This indicates relatively little mixing between dry, ozone-rich stratospheric air and relatively moist, ozone-poor tropospheric air. The stratosphere is characterized by very small vertical mixing and the temperature increases with height except in the winter at high latitudes; the temperature distribution is mainly determined by a balance between infrared radiative cooling and radiative heating due to the ozone absorption of solar ultraviolet radiation. Above the stratopause in the mesosphere the ozone heating rate as well as the ozone concentration decreases with height and so does the equilibrium temperature.

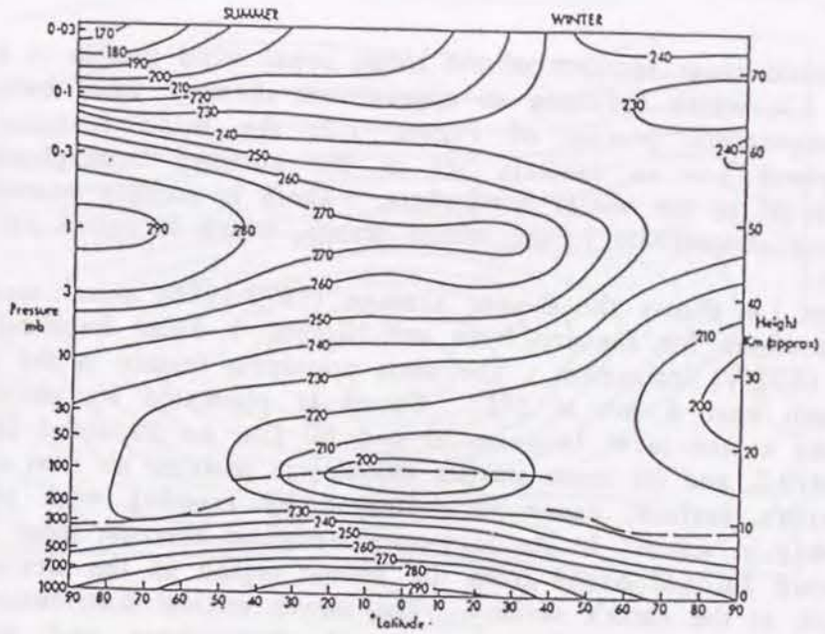

Figure 1.2: Schematic latitude-height section of zonal mean temperatures (K) at the solstices [Murgatroyd, 1969].

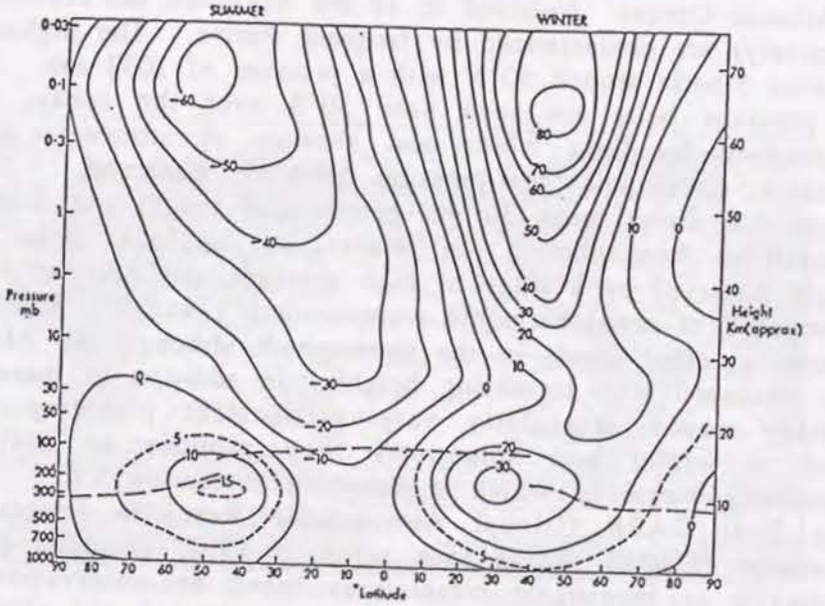

Figure 1.3: Schematic latitude-height section of zonal mean westerly winds (ms^{-1}) at the solstices [Murgatroyd, 1969].

Schematic cross sections of the mean zonal wind profile is shown in Figure 1.3, which indicates an approximate *thermal wind* balance with the temperature profile of Figure 1.2; the main features in the stratosphere are an easterly jet in the summer hemisphere and a westerly jet in the winter hemisphere. There is another westerly jet in the lower stratosphere in the winter season, which is called *polar night jet*.

Figure 1.4 shows the 8-year average (1979-1986) zonal mean ozone cross sections for January from the Nimbus 7 Solar Backscatter Ultra Violet (SBUV) instrument. The most prominent feature is the equatorial maximum near 8 mb at 5°S. Ozone is generated by photochemical reactions at the level between 20 and 60 km, as discussed in sections 2.4 and 3.2, and (in much smaller amount) in polluted air over cities. At the earth's surface, ozone is destroyed by reacting with plants and dissolving in water. In the long-term statistical average, there is a slow downward flux of ozone from the source region in the stratosphere to the sink at the earth's surface. The ozone vertical distribution roughly determines the thermal structures of stratosphere and mesosphere through the absorption of solar radiation.

The climatological January sea level pressure pattern is shown in Figure 1.5. The prominent low-pressure areas over the northern Pacific and Atlantic Oceans (referred to as the *Aleutian* and *Icelandic* lows, respectively) are characterized by frequent storms. The highest value is seen over Siberia around 50°N with a pressure of 1032 mb. Subtropical high pressure belts are seen near 30°S over the ocean, which are characterized by light winds and absence of storms. Around the Antarctica, circumpolar low-pressure belts are observed.

Figure 1.6 shows mean 30 mb geopotential height and temperature in the northern hemisphere. In winter, the cyclonic polar vortex is strongly distorted by a ridge of high pressure, the Aleutian high, which is composed of zonal harmonic wavenumbers 1 and 2. Similar patterns are seen at other levels in the stratosphere although the Aleutian high shifts westward with increasing height. In addition to these stationary planetary waves, irregularly varying transient planetary waves are forced in winter and sometimes they produce so called sudden stratospheric warmings, which is discussed in section 3.2.

The First GARP (Global Atmospheric Research Program) Global Experiment (FGGE), which took place in 1979, provided an excellent opportunity to investigate circulations based on observational data in the tropics and in the southern hemisphere. Global grid point data sets, so called FGGE Level IIIb data sets, are produced by the European Centre for Medium Range Weather Forecast (ECMWF) by the four-dimensional assimilation systems; these are integrated systems of

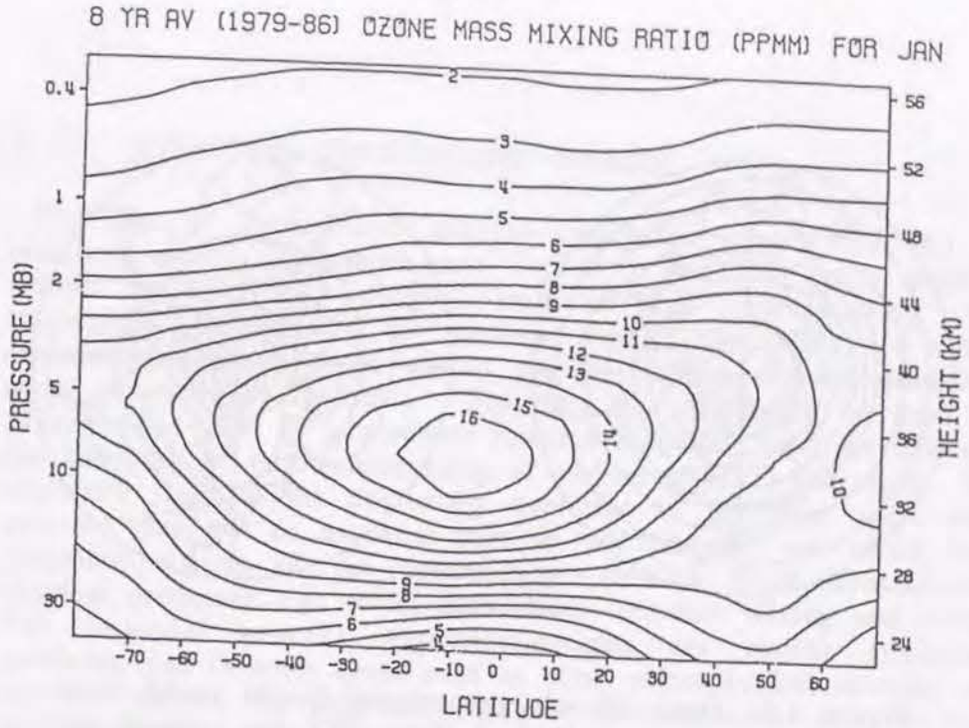

Figure 1.4: Zonally and monthly averaged ozone mixing ratio (μ gm/gm) for January (1979-1986) [Nagatani *et al.*, 1988].

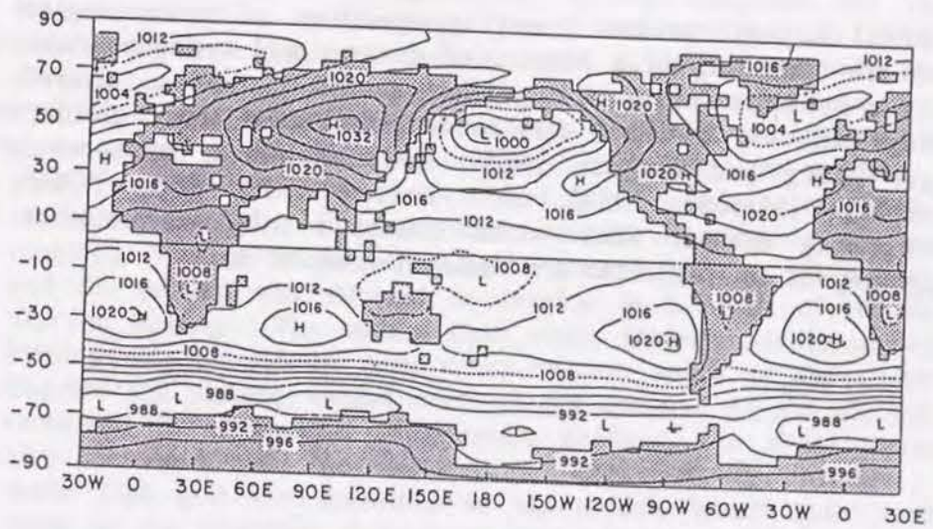

Figure 1.5: Observed sea level pressure field (mb) for January. The contour interval is 4 mb. [Schutz and Gates, 1971].

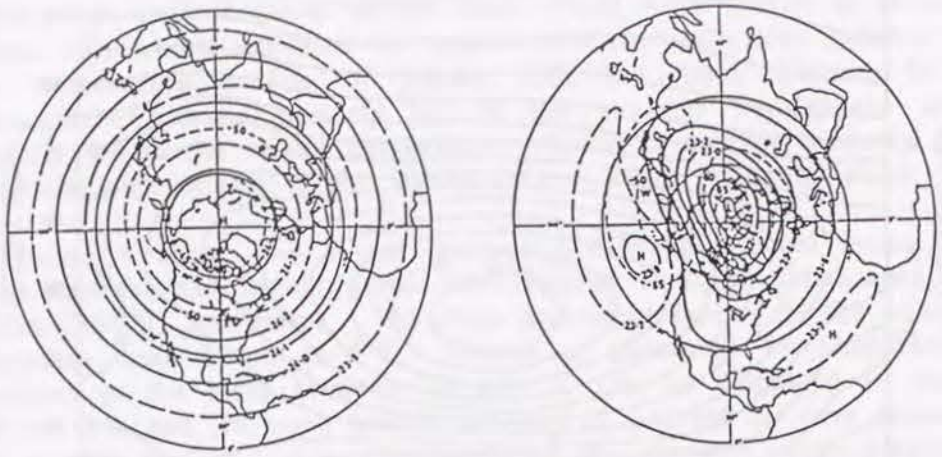

Figure 1.6: Mean 30 mb geopotential height (solid lines, km) and temperature (dashed lines, °K) for summer and winter northern hemisphere seasons [Hare, 1968].

numerical forecast process and interpolation of meteorological data which are consisting of a mixture of conventional synoptic observations and non-synoptic observations from satellites, buoys, aircraft, and drifting balloons. These data made possible to study global energy budget [Kung and Tanaka, 1983], meridional heat transport by the atmosphere [Masuda, 1988], and so forth. By using FGGE data, nonmigrating diurnal tides which relates to the wavenumber 4 of topography at low latitudes are detected (chapter 4).

1.2 general circulation model

The aim of atmospheric general circulation models (GCMs) is to simulate earth's atmosphere and exploit it for long-range prediction. GCMs can provide stringent tests of our understanding of the atmospheric system. If all relevant physical processes are correctly represented, then a GCM should provide a faithful simulation of the three dimensional circulation. Therefore, the GCM can be used as an *experimental tool* in atmosphere research including study of tide to test the adequacy of our understanding of various physical processes. GCMs explicitly simulate the day-to-day evolution of the large scale weather systems that are an essential part of the climate, and which include parameterizations of the predominant smaller scale dynamical and physical processes *e.g.* moist convection, turbulent mixing and radiation. The physical process parameterizations are recent fundamental problems, and in some cases such as cloud microphysical process, we do not yet confirm the possibility of parameterizations [*e.g.*, Washington and Parkinson, 1986]. Recent progress in numerical modeling of the general circulation has been to some degree dictated by the rate of development in the field of computer technology. Supercomputers and programming techniques relating to optimization are discussed in section 3.1.

The origins of general circulation modeling as considered here follow close behind the first application of the computer for short-range weather prediction by Charney, Fjörtoft and von Neuman [1950]. It was soon recognized that such models could be of use not only for weather forecasting but also for studying the behavior of the atmosphere. Phillips [1956] made the first attempt to model the general circulation numerically. His original model used the approximate "*quasi-geostrophic*" equations and a two layer vertical resolution, with a latitudinally varying but otherwise constant distribution of heating and cooling. The model atmosphere was started from an initial state of rest and the motion was allowed to develop as a result of the differential diabatic heating. The motion field which initially developed was a pure Hadley cell circulation with rising motion south of the center of the channel and sinking motion north of the center. As the diabatic heating increased the latitudinal temperature gradient, the zonal thermal wind also increased until the flow became baroclinically unstable. Phillips made high and low pressures in the model, which quite resemble to those of the observed features in mid-latitude weather chart.

Geostrophic relationship (1.1) as well as *quasi-geostrophic* equations are valid at mid-latitudes, however they cannot be used in low latitudes

where Coriolis factor is very small. Therefore, less restrictive modeling assumptions have been investigated. Since hydrostatic approximation is a very accurate for large scale motion, the equations can be written in pressure coordinates. The resulting system consists of horizontal components of the momentum equation, the thermodynamic energy equation, the continuity equation, the hydrostatic approximation and the equation of state. In the (x, y, p) system, basic forms of these equations can be written in vector notations as

$$\frac{d\mathbf{v}}{dt} + f\mathbf{k}\times\mathbf{v} = -\nabla_p\Phi + \mathbf{F}, \qquad (1.8)$$

$$C_p\frac{dT}{dt} = \omega\alpha + Q, \qquad (1.9)$$

$$\nabla_p\cdot\mathbf{v} + \frac{\partial\omega}{\partial p} = 0, \qquad (1.10)$$

$$\frac{\partial\Phi}{\partial p} = -\alpha, \qquad (1.11)$$

$$\alpha = RT/p, \qquad (1.12)$$

where

$$\frac{d}{dt} = \frac{\partial}{\partial t} + \mathbf{v}\cdot\nabla_p + \omega\frac{\partial}{\partial p}, \qquad (1.13)$$

and the horizontal ∇_p operator refers to differentiation at constant pressure, Φ the geopotential (=gz), g the acceleration of gravity, and z is height. ω ($\equiv\frac{dp}{dt}$) is the vertical p-velocity, T the temperature, α the specific volume, C_p the specific heat at constant pressure, R the gas constant, Q the heating rate per unit mass, and **F** is the frictional force. The set of six equations (1.8)-(1.12) contains the six independent scalar variables u, v, ω, T, Φ, α, making it in principle a solvable system, once the values of the constants and of Q and **F** are given. However, the above form of the equations is not the most convenient for practical solution when we incorporate orography in the model. In chapter 2, these equations are transformed from the pressure coordinate system to the so called *sigma* coordinate system. The important point here is that the six variables u, v, ω, T, Φ, and α are related in time and three-dimensional space in a compact system of six equations. Additional equations for water vapor and ozone are presented in chapter 2, which relate to the time change of water vapor and ozone with their sources and sinks within the atmosphere. The total system (1.8)-(1.12) is not closed, because the frictional term **F** and the diabatic heating term Q

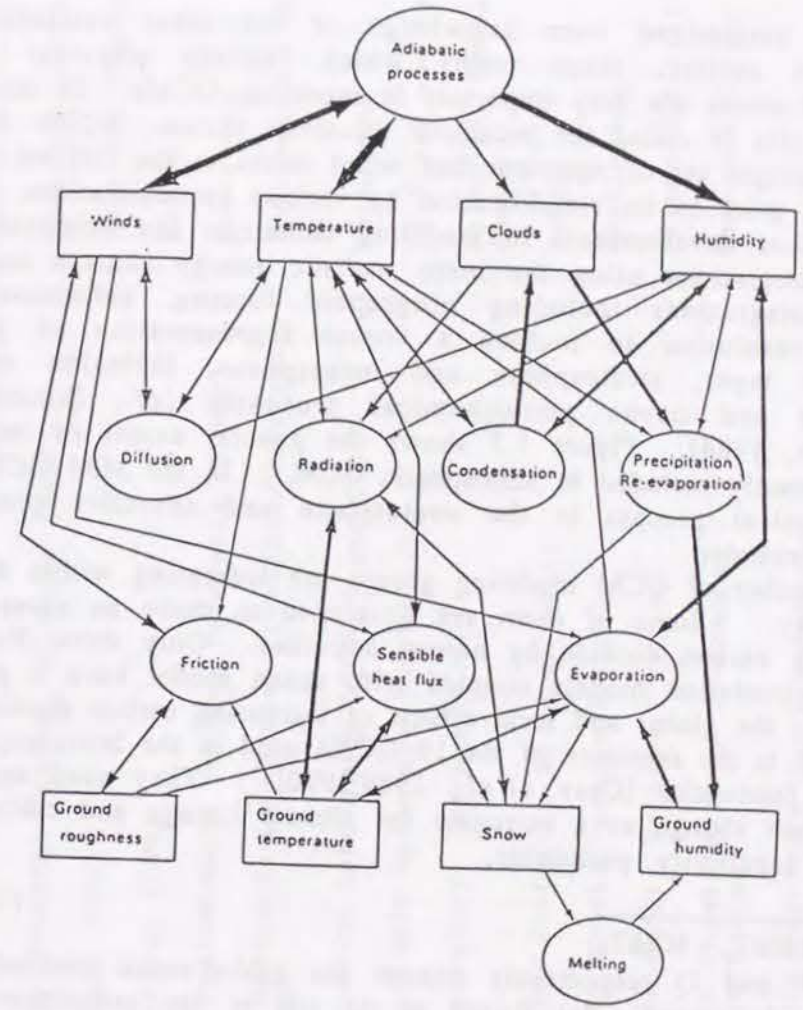

Figure 1.7: Schematic illustration of the processes commonly included in atmospheric general circulation models. The thickness of a particular arrow gives a qualitative indication of the importance of the interaction the arrow represents [Simmons and Bengtsson, 1984].

must be determined from knowledge of the other variables. As mentioned earlier, these terms which include physical process parameterizations are very important in modeling GCMs. In the current literature this is called the *primitive* equation system, which does not imply a simple set of equations but rather refers to the full set of basic equations, prior to its simplification by various approximations.

Subsequent developments in modeling technique and computer power led to integrations using the more realistic energy sources and sinks, global integrations including orographic forcing, enhancements in vertical resolution to include a coarse representation of planetary boundary layer, stratosphere and mesosphere, inclusion of moist processes and ozone photochemical processes [*cf.*, Simmons and Bengtsson, 1984]. Figure 1.7 shows the general extent of interactions that commonly included in atmospheric GCM. In the MRI GCM, ozone photochemical process in the stratosphere and advective process are further included.

The number of GCM modeling groups are increasing within the world community. Some of them are developed to make an assessment of increasing carbon dioxide by human activities. Only three dimensional general circulation models coupled with ocean model have a possibility to predict the global and local effects of increasing carbon dioxide Table 1.1 is the summary of the 19 GCMs used in the intercomparison of climate feedbacks [Cess *et.al.*, 1989,1990]. They used sea surface temperature change as a surrogate for climate change and calculated the climate sensitivity parameter,

$$\lambda = \frac{1}{\Delta F/\Delta T_s - \Delta Q/\Delta T_s}, \qquad (1.14)$$

where F and Q respectively denote the global-mean emitted infrared and net downward solar fluxes at the top of the atmosphere, T_s the global mean surface temperature, and Δ indicates the change of the variable in the sensitivity experiment. The equation (1.14) is also written as

$$\Delta T_s = \lambda (\Delta F - \Delta Q) . \qquad (1.15)$$

Thus, an increase in λ represents an increased climatic change due to a given climate forcing at the top of the atmosphere ($\Delta F - \Delta Q$). The value λ can be evaluated for the globe as a whole and also for "clear" and "overcast" conditions; *i.e.*, sensitivity parameters employing respectively clear and overcast fluxes. These results are shown in Figure 1.8. While the 19 GCMs exhibit notable agreement in the clear sensitivity parameter, a roughly threefold variation in the global climate sensitivity is found among the models. Cess *et.al.*, [1990] concluded that most of

Table 1.1 Summary of the GCMs used in the model intercomparison [Cess *et al.*, 1990]. There are two GFDL models.

Model	Investigator(s)
Bureau of Meteorology Research Centre, Melborne (BMRC)	McAvaney and Rikus
Canadian Climate Center (CCC)	Boer and Blanchet
Colorado State University (CSU)	Randall
European Centre for Medium Range Weather Forecasts (ECMWF)	Morcrette
European Centre for Medium-Range Weather Forecasts/University of Hamburg (ECMWF/UH)	Roeckner and Schese
Geophysical Fluid Dynamics Laboratory (GFDL I and II)	Wetherald
Laboratoire de Météorologie Dynamique (LMD)	Le Treut and Li
Main Geophysical Observatory, Leningrad (MGO)	Meleshko, Sokolov and Sheinin
Meteorological Research Institute of Japan (MRI)	Yagai
NCAR Community Climate Model, Version 0 (CCM0)	Washington
NCAR Community Climate Model, Version 1 (CCM1)	Slingo and Kiehl
NCAR Community Climate Model/Lawrence Livermore National Laboratory (CCM/LLNL)	Ghan and Taylor
Oregon State University/Institute for Atmospheric Physics, Beijing (OSU/IAP)	Liang
Oregon State University/Lawrence Livermore National Laboratory (OSU/LLNL)	Cess and Potter
United Kingdom Meteorological Office (UKMO)	Mitchell

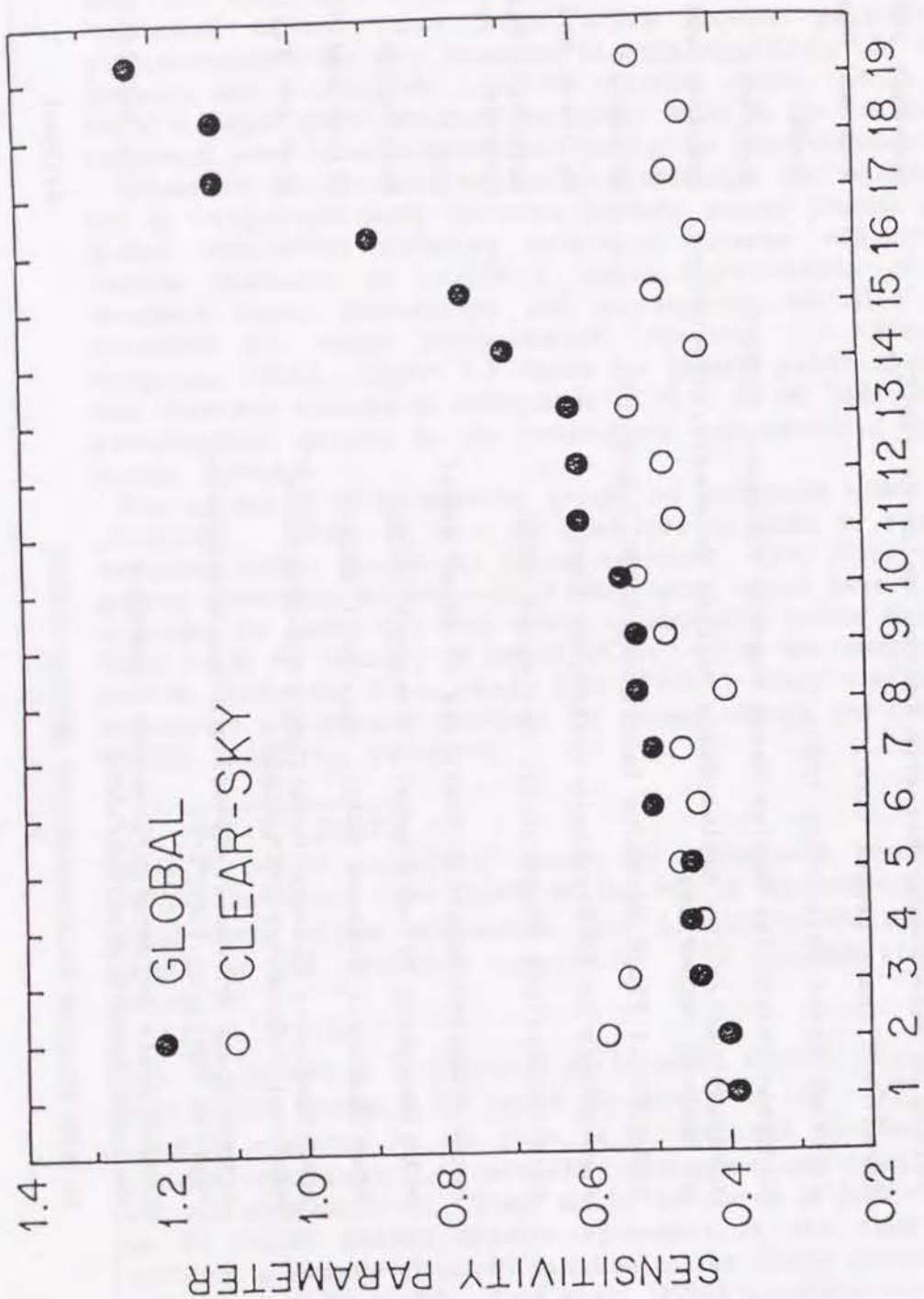

Figure 1.8: Clear-sky and global sensitivity parameters ($K\ m^2 W^{-1}$) for the 19 GCMs [Cess *et al.*, 1990].

this variation is attributable to differences in the model's depictions of cloud feedback. The MRI GCM is numbered 11 in the figure and the value of the sensitivity parameter is not so differ from the mean value. This suggests that the MRI GCM is well constructed within the current knowledge in the field of meteorology.

Apparently current GCM has its limitation to be used as a climatic predictor, however the GCM is one of the most useful *experimental tools* in atmosphere research. In chapter 3 simulated results of the Meteorological Research Institute GCM, one of the sophisticated models, are presented and compared with the observation.

1.3 Atmospheric thermal tides

Atmospheric tides are global-scale daily oscillations in any atmospheric field whose periods are integral fractions of either a lunar or a solar day. Of the various observed tidal modes only the thermally driven solar diurnal and semidiurnal components, which are primarily forced by the diurnal variations of solar heating are discussed. The lunar gravitational forcing that excite atmospheric tides is about 1/20 of magnitude smaller than the thermal forcings. Reviews of tidal theory and observations have been made by Chapman and Lindzen [1970], and more recently by Forbes and Garret [1979], Kato [1980], and Volland [1988].

Atmospheric tides were not recognized until the development of the barometer by Torricelli (ca. 1643). The most extensive observations of the atmospheric tides are have been made by using long time series of barometric measurements. Usually a continuous record of hourly pressure observations or the average values of the surface pressure at each hour of day is used to detect the diurnal variations. The classical work in this area is that of Haurwitz [1956, 1965]; he collected long time series of station data through out the world and calculated amplitude and phase of the diurnal and semidiurnal surface pressure oscillation. The semidiurnal component $S_2(p)$ dominates with maxima about 1.2 mb at around 10 A.M. and 10 P.M. local time. The diurnal component $S_1(p)$ is relatively small and irregular: the maximum amplitude of wavenumber 1 component is about 0.6 mb. Figure 1.9 shows the annual mean amplitude of the diurnal surface pressure oscillation $S_1(p)$ and the stations used for the computation by Haurwitz and Cowley [1973]. It can bee that $S_1(p)$ is strongly affected by surface conditions, especially by the distribution of ocean and continents. Then, they calculated spectrum distribution of wave amplitude of component waves. Figure 1.10 is the Fourier coefficients of $S_1(p)$ integrated over latitudes.

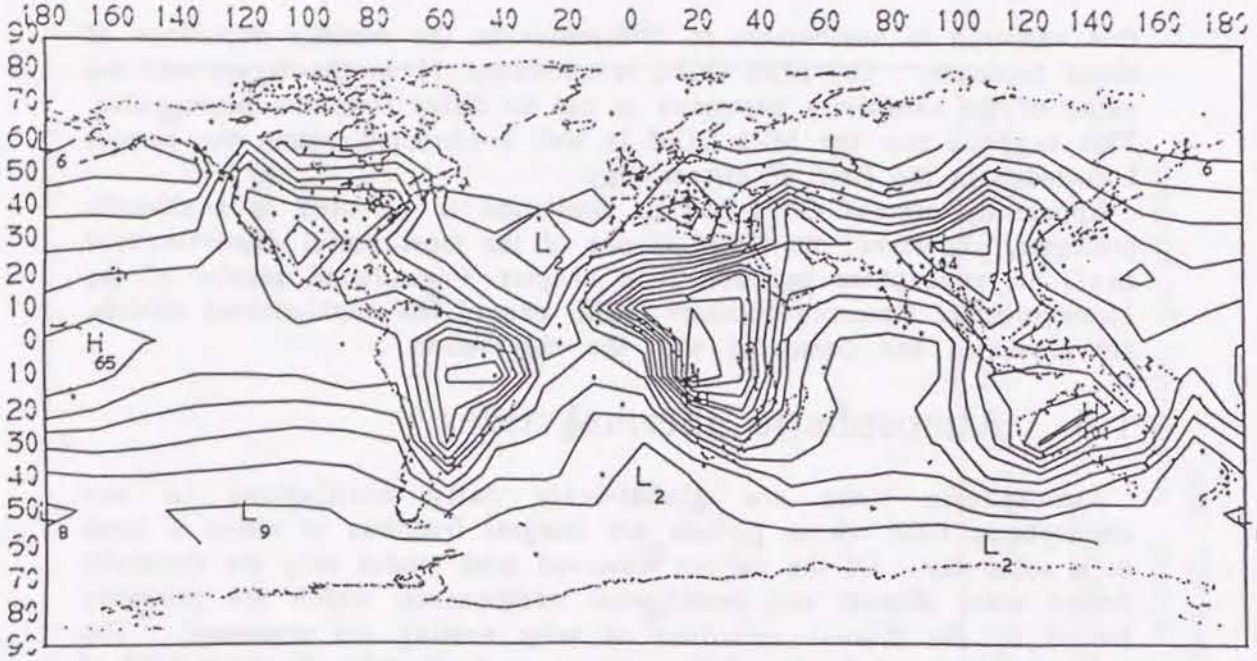

Figure 1.9: The annual mean amplitude of the diurnal surface pressure oscillation $S_1(p)$ and the stations. The contour interval is 0.1 mb. H and L show positions of maxima and minima; the adjoining numbers are amplitudes in units of 0.01 mb [Haurwitz and Cowley, 1973].

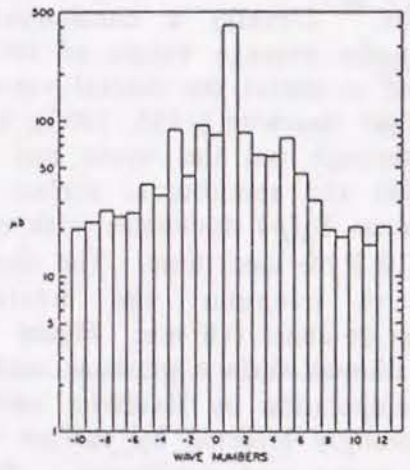

Figure 1.10: Fourier coefficients of the diurnal surface pressure oscillation $S_1(p)$ integrated over latitudes [Haurwitz and Cowley, 1973].

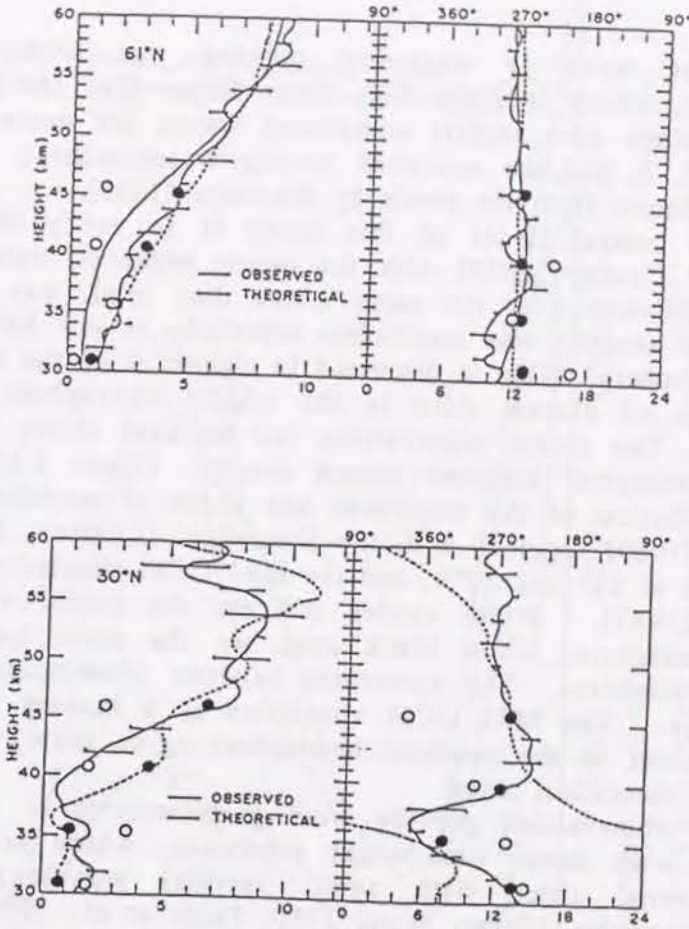

Figure 1.11: The vertical distribution of the amplitude (left) and phase (right) of meridional wind for the westward moving wavenumber 1 diurnal tide at 61°N (top) and 30°N (bottom). The results by the MRI GCM are plotted by circles on the figure reproduced from Reed *et al.* (1969). White and black circle indicate the values at the nearest grid points to 61° and 30° in the northern and southern hemispheres, respectively. The solid line shows the results by Reed *et al.* (1969), the dashed line by Lindzen (1967) and the thin solid line by Forbes (1982a) [Tokioka and Yagai, 1987].

The dominant wave is westward moving one with the zonal wavenumber 1, which is about four times larger than the next largest wave. The three next largest component waves are eastward moving wavenumber 1, 3, and the westward moving wavenumber 2. The order is slightly different from the result by Haurwitz [1965].

One of the central issues of this thesis is to verify the result by *Haurwitz and Cowley* [1973] with the recent improved data sets, since the data distribution over the earth which they used, was uneven and the number of stations was insufficient especially at low latitudes in the southern hemisphere. This is discussed in chapter 4 of the thesis.

Observations of diurnal tides in the middle atmosphere are sparser and limited. The rocket observations can be used above 30 km level where meteorological balloons cannot reach. Figure 1.11 shows the vertical distribution of the amplitude and phase of meridional wind by Reed *et al.* [1969] together with the theoretical (Lindzen, 1967; Forbes, 1982a) values at 61° and 30°N, and the MRI GCM simulation by Tokioka and Yagai [1987]. White circles indicate the model values in the northern hemisphere, while black ones are the same latitude in the southern hemisphere. The agreement between observation and theory is quite good. The MRI GCM simulation is a January case and the simulated values in the southern hemisphere agree quite well with the observed or theoretical ones.

The radar observations provide wind measurements in altitude range 70-110 km with dense time-height resolution, which are suitable to observe diurnal tides with small vertical wavelength such as nonmigrating modes [Fukao *et al.*, 1980; Tsuda *et al.*, 1985]. However, they are restricted in geographical coverage. In contrast with this, satellite techniques can obtain near-global tidal observations, but the vertical resolution is limited.

Atmospheric thermal tides are forced primarily by the radiative heating resulting from the absorption of solar radiation by ozone in the stratosphere and by water vapor in the troposphere. Ozone photochemical process is described in chapter 2 and the MRI GCM successfully simulates the climatic distribution (see Figure 3.5). Water vapor is highly variable both in space and time. In particular, there are large zonal asymmetrics in the water vapor heating due to the influence of continents and oceans. The condensational heating within an air column is proportional to the total precipitation. The MRI GCM simulates the geographical distribution of precipitation well (see Figure 7 of Tokioka *et al.* [1985]). The thermal forcings of diurnal and semidiurnal tides are usually expanded into Hough tidal components. Figure 1.12 shows the vertical distribution of the expanded coefficient of the diurnal mode heating by the MRI GCM, which are decomposed

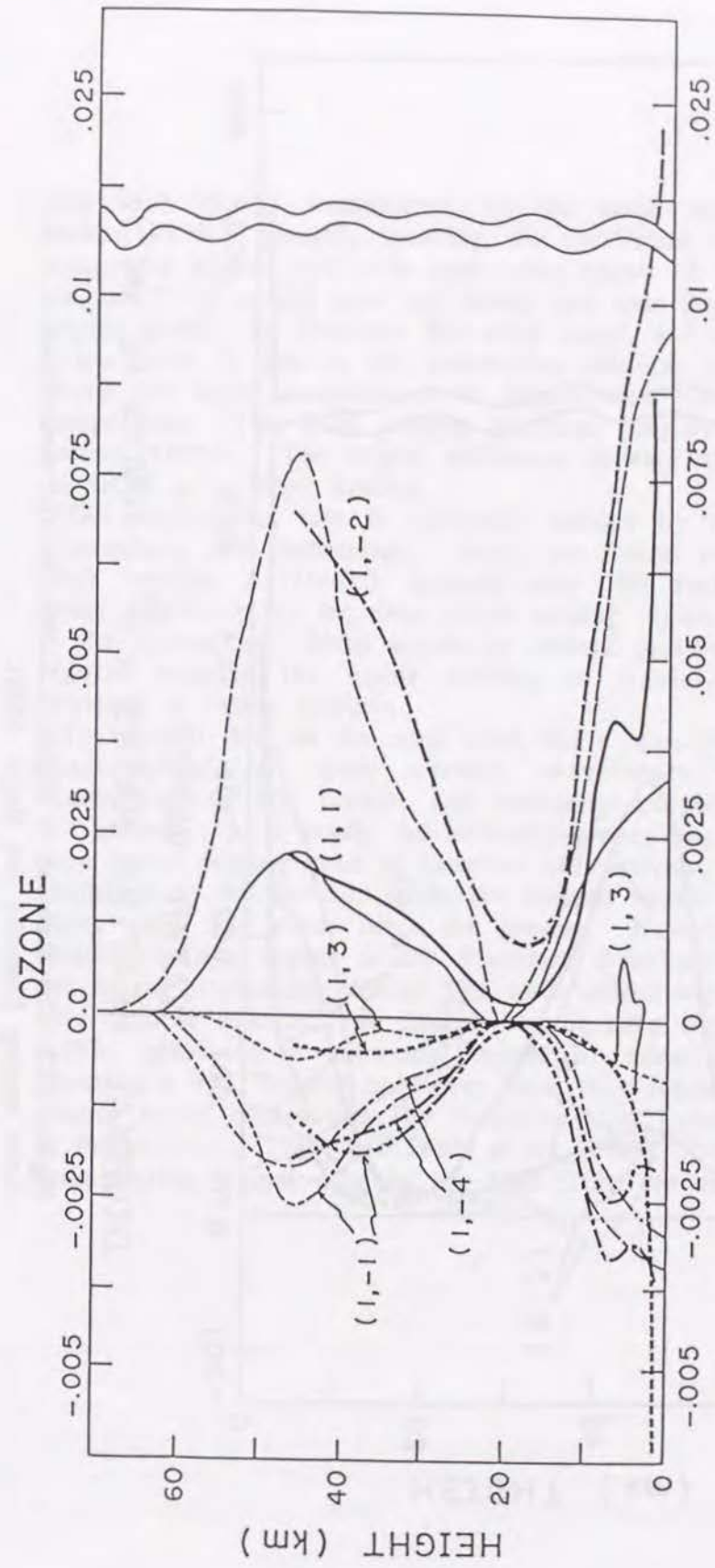

Figure 1.12: The vertical distribution of the coefficients of Hough tidal components as defined in Forbes [1982a]. The notation of Hough components also follows him. Thin lines correspond to the results of Forbes [1982a]. Each component is multiplied by the pressure factor $e^{-x/2}$, where $x=-\ln(p/p_0)$ and p_0 =1000 mb [Tokioka and Yagai, 1987].

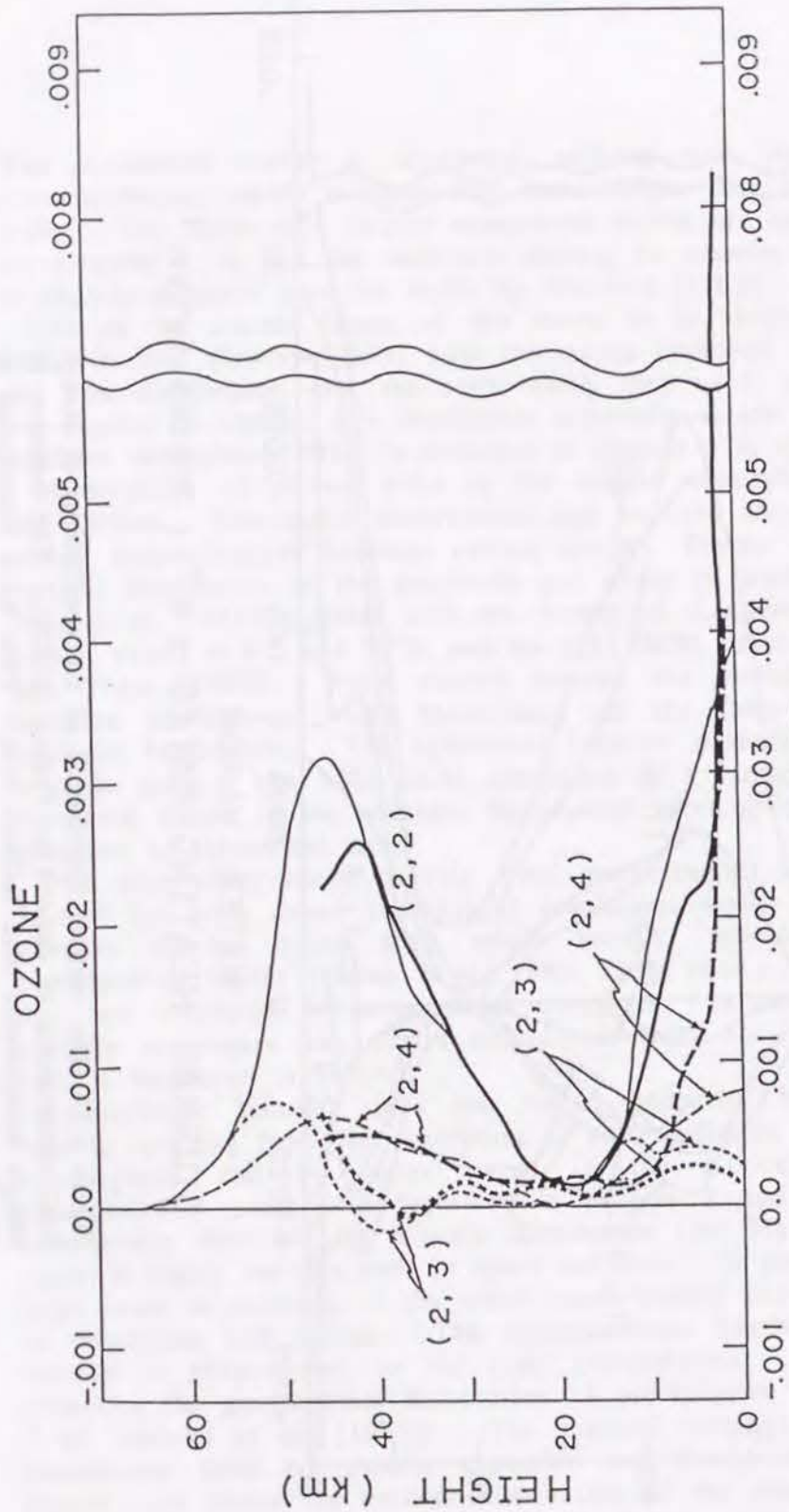

Figure 1.13: The same as in Figure 1.12 but for the semidiurnal mode heating [Tokioka and Yagai, 1987].

into each Hough components in the same way as was done by Forbes[1982a]. Roughly speaking, the coefficient of each Hough diurnal component agrees well with each other above 10 km level. Below 10 km, the GCM results have two peaks; one near the surface is due to the heating within the Planetary Boundary Layer, and the other around 7 to 8 km level is due to the penetrative cumulus heating. Figure 1.13 shows the same quantities as in Figure 1.12 but for the semi-diurnal components. The GCM heating functions roughly agree with those by Forbes [1982b]. The largest difference appears near the surface where the GCM gives larger heating.

The semidiurnal tide is primarily excited by ozone heating in the stratosphere and mesosphere. Since the forced semidiurnal tide has a large vertical wavelength (greater than 100 km), it can be excited rather efficiently by the deep ozone heating region and easily propagate to the ground and hence appear in surface pressure fluctuations. It is regular because the ozone heating is regular, and its latitudinal structure is rather uniform.

The diurnal tide, on the other hand, has a more complex behavior; it is characterized by short vertical wavelength propagating modes equatorward of 30° latitude and vertically trapped modes poleward of 30° latitude. As a result, the vertically propagating modes forced by the deep ozone heating tend to interfere destructively, and thus have small amplitude at the ground, while the trapped modes forced by the ozone decay away and never reach the ground. However, the comparatively shallow heating region in the Planetary Boundary Layer (Figure 1.12) can excite propagating diurnal tide quite effectively. The PBL heating over land is essential for diurnal nonmigrating tides. Tsuda and Kato [1989] presented a numerical model of nonmigrating thermal tides assuming a PBL heating only over land; their results are agree well with ground based observations by Haurwitz [1965] and Radar observations by Fukao *et al.*, [1980] and Tsuda *et al.*, [1985]. Simulated results of the nonmigrating diurnal tides by the MRI GCM are discussed in chapter 4.

1.4 Contents of the thesis

As described in the previous section, GCMs have been developed in many research groups in the world. The GCMs are closely related to the numerical prediction models for short and medium range weather forecast, but they are much concentrated on the improvement of model physical process parameterizations which are important for climate simulation and long-range prediction. Recently a GCM can be used not only as a simulator of the earth's atmosphere but also as an *experimental tool* in atmospheric research to test our understanding of various physical processes. An example is the orographically induced gravity wave drag, which has large impacts on the winter circulation in the model atmosphere, however the performance of the parameterization is far from complete. An important project which relates to an assessment of increasing carbon dioxide by GCMs is now going on [Cess *et al.*, 1990]. Only three dimensional general circulation models coupled with ocean model have a possibility to predict the global and local effects of increasing carbon dioxide by human activities.

Theoretical calculation of thermal tide has been done since Chapman and Lindzen [1970]. The fundamental problem is how to give thermal forcings in the theoretical model. Tokioka and Yagai [1987] analyzed the result of the GCM simulation in January and found detailed structure in the thermal forcings of diurnal and semidiurnal modes within the planetary boundary layer (PBL), which are not seen in the model by Forbes [1982a,b]. The thermal forcings resulted in the GCM simulation will be verified by comparing simulated results with the available observations, since no direct observations of thermal forcings are possible currently. Nonmigrating diurnal tides forced by the wavenumber 4 of topography are detected by the data analysis and the MRI GCM simulation, which are discussed in chapter 4 and comprise main issue in the thesis.

The plan of the thesis is as follows. In the present chapter we briefly review the observational features of the general circulation of the atmosphere, especially the zonally averaged circulations and ozone distributions. Basic equations for modeling of the general circulation of the atmosphere are described with the physical process parameterizations. A short review of thermal tides of the atmosphere are also presented.

In chapter 2, the Meteorological Research Institute general circulation model (MRI GCM-I) is described, which is based on the University of California at Los Angels (UCLA) model, described by Arakawa and Mintz [1974] and Arakawa and Lamb [1977]. Ozone photochemical process in

the stratosphere and radiative process which includes the heating by incoming shortwave solar radiation and the cooling by infrared longwave radiation, are described in detail; ozone distribution in the stratosphere as well as water vapor in the troposphere and resulted radiative forcings are essential to the thermal tides in the atmosphere. Moreover, the author contributed to the MRI GCM in the calculation of ozone photochemistry and radiation scheme which were originally developed by Schlesinger [1976] and Katayama [1972].

In chapter 3, the hardware and software of the supercomputer system installed in the Meteorological Research Institute are described. Without a supercomputer, the study with a sophisticated three dimensional GCM is almost impossible. The performance of the MRI GCM is also discussed in this chapter with emphasizing the effect of gravity wave drag. Actually, the model used in the study of tide is an old version of the MRI GCM which does not include gravity wave drag and has westerly biases; the westerly jet in the stratosphere is too strong, the Aleutian low in the troposphere too deep, and no stratospheric sudden warmings appear. The deficiencies are almost overcome by incorporating gravity wave drag which has pronounced effects on the circulations in the northern hemisphere. Since the model has its limitation, especially relating to the sub-grid scale topography, we made a model improvement trial by increasing surface drag coefficients in the tropospheric version of the MRI GCM (Yagai and Tokioka, 1987).

In chapter 4, observed and simulated nonmigrating diurnal tides are presented following Yagai [1989]. The analysis is made with FGGE (First GARP Global Experiment) Level IIIb data during the special observation period (SOP-1) of 10 January-9 February 1979. First is the westward moving diurnal mode with the zonal wavenumber five, and the second a eastward moving diurnal mode with the zonal wavenumber three. These modes are closely related to the wavenumber four of topography at low latitudes and have clear peaks in the space-time power spectra in the sea level pressure field. They are well simulated by the MRI GCM in the troposphere. Finally, in chapter 6 the summary and conclusion of this thesis are presented.

Chapter 2

The Meteorological Research Institute General Circulation Model

The general circulation model developed at the Meteorological Research Institute (MRI GCM-I) is basically identical to the University of California at Los Angels (UCLA) model, described by Arakawa and Mintz [1974] and Arakawa and Lamb [1977] with minor changes to both the dynamical and physical processes of the model.

The MRI GCM-I has twelve vertical layers (corresponding approximately to 1.39, 2.68, 5.18, 10.0, 19.3, 37.3, 72.0, 150, 300, 500, 700, and 900 mb) with the top level at 1 mb, and a horizontal resolution of 5° in longitude by 4° in latitude. The solar radiation incident at the top of the model atmosphere has both seasonal and diurnal variations. The solar flux under cloudless condition is depleted by ozone and water vapor absorption. Ozone prediction is based on a simplified photochemical model by Schlesinger and Mintz [1979], which includes Chapman reactions and the NO-NO_2 catalytic cycle in the stratosphere above 100 mb. The albedo of the earth's surface is determined diagnostically by the model as a simple function of surface conditions. Clouds are generated in the model and interact with radiation. Water vapor, ozone and carbon dioxide absorb and emit longwave radiation. The model includes the earth's topography. The distribution of sea surface temperature and sea ice are prescribed based on climatological data. Surface fluxes of sensible heat, water vapor and momentum are calculated by the bulk method with the transfer coefficients proposed by Deardorff [1972]. Ground temperature, snow depth and ground wetness are predicted in the model. The time step is 7.5 min. and all the physical processes are calculated at one hour intervals.

To simulate thermal tides with a general circulation model, it is essential to calculate ozone photochemical process and radiative heat process as well as dynamical process correctly. Therefore we will give a description of the dynamical part in section 2.1, ozone photochemistry in the stratosphere in section 2.2, and radiation calculation in 2.3. A detailed account of the model has been given by Tokioka *et al*, [1984].

2.1 Dynamical process

2.1.1 The vertical coordinate

Various vertical coordinates are proposed to improve treatment of orography in general circulation and numerical prediction models [Kasahara, 1974]. In the geometric height coordinate system, the ground surface does not coincide with the coordinate surface and a special procedure must be developed to handle the effect of the earth's orography. The handling of orographic blocking is especially cumbersome in the pressure coordinate system, since the surface pressure at the ground varies in time and space. Phillips [1957] introduced the so called sigma-coordinate system defined by $\sigma=p/p_s$, where p is pressure and p_s is the surface pressure. The ground is identified by $\sigma=1$ in the σ-coordinate system and easy to handle lower boundary conditions along the mountain surface. In the MRI GCM, a combination of the σ-coordinate for the lower part of the atmosphere and the pressure coordinate for the upper part of the atmosphere is used.

The vertical coordinate σ is defined as

$$\sigma = \frac{p-p_I}{\pi}, \tag{2. 1}$$

$$\pi = \begin{cases} p_s-p_I & \text{for } p \geq p_I \\ p_I-p_t & \text{for } p<p_I \end{cases}, \tag{2. 2}$$

where p_s is the variable pressure at the earth's surface and p_t the constant pressure at the top boundary of the model (1 mb). p_I is a constant and usually indicates the tropopause level. Therefore σ=-1, 0, 1 at $p=p_t$, p_I, and p_s. As π is constant above the level $p=p_I$, the σ-coordinate defined by (2.1) is nothing but the normalized pressure coordinate.

From (2.1), the individual time derivative of pressure, ω, is given by

$$\omega \equiv \frac{dp}{dt} = \pi\dot{\sigma} + \sigma\left(\frac{\partial\pi}{\partial t} + V\cdot\nabla\pi\right), \tag{2. 3}$$

where $\dot{\sigma}=d\sigma/dt$, V is the horizontal velocity and ∇ is the horizontal gradient operator.

In the σ-coordinate, the earth's surface is a coordinate surface as well as a material surface. The kinematical boundary condition at the surface is therefore,

$$\dot{\sigma} = 0 \quad \text{at} \quad \sigma = 1. \tag{2. 4}$$

At the top of the model, we assume that no air parcels cross the top boundary. Thus,

$$\dot{\sigma} = 0 \quad \text{at} \quad \sigma = -1 . \tag{2. 5}$$

2.1.2 Basic equations in the atmosphere

We assume that the model atmosphere is a perfect gas
Thus

$$\alpha = RT/p . \tag{2. 6}$$

where α is the specific volume, T the temperature, and R is the gas constant.

For large-scale motions of the atmosphere, the horizontal extent of motion is much larger than the vertical; therefore, the vertical acceleration term in the momentum equation may be neglected by scale analysis [Charney, 1948] and the hydrostatic approximation will be valid. The hydrostatic equation in the pressure coordinate system, $\delta\Phi = -\alpha\delta p$, is written as

$$\delta\Phi = -\pi\alpha\delta\sigma , \tag{2. 7}$$

where Φ is the geopotential (=gz), g the acceleration of gravity, and z is height. This equation may be transformed in to the following equivalent forms;

$$\delta\Phi = -RT\delta ln\, p \tag{2. 8}$$

$$= -C_p\theta\delta(p/p_0)^{\kappa} \tag{2. 9}$$

$$= -C_p \frac{d ln\theta}{d(\frac{1}{\theta})} \delta(p/p_0)^{\kappa} , \tag{2.10}$$

$$\delta(\Phi\sigma) = -(\pi\sigma\alpha - \Phi)\delta\sigma , \tag{2.11}$$

where C_p is the specific heat at constant pressure, $\kappa = R/C_p$, and θ is the potential temperature, $T(p/p_0)^{-\kappa}$, where p_0 is a standard pressure.

The equation of continuity in the pressure coordinate is

$$\nabla_p . v + \frac{\partial \omega}{\partial p} = 0 , \tag{2.12}$$

where ∇_p means ∇ operator on the constant pressure surface, which relates to ∇_σ as

$$\nabla_p = \nabla_\sigma + \nabla_p\sigma\frac{\partial}{\partial\sigma} = \nabla_\sigma - \frac{\sigma}{\pi}\nabla\pi\frac{\partial}{\partial\sigma} . \tag{2.13}$$

With the use of (2.3) and (2.13), (2.12) gives the continuity equation in the σ−coordinate system

$$\frac{\partial \pi}{\partial t} + \nabla_\sigma .(\pi v) + \frac{\partial}{\partial\sigma}(\pi\dot{\sigma}) = 0 . \tag{2.14}$$

By integrating (2.14) with respect to σ from $\sigma = -1$ to $+1$ and using (2.1), we obtain

$$\frac{\partial p_s}{\partial t} = -\int_{-1}^{1} \nabla .(\pi v) d\sigma , \tag{2.15}$$

as $\dot{\sigma} = 0$ at $\sigma = -1$.

The pressure gradient force in the pressure coordinate system, $-\nabla_p\phi$, is transformed into

$$-\nabla_p\Phi = -\nabla_\sigma\Phi + \frac{\sigma}{\pi}\nabla\pi\frac{\partial\Phi}{\partial\sigma} = -\nabla_\sigma\Phi - \sigma\alpha\nabla\pi , \tag{2.16}$$

with the use of (2.7) and (2.13). Then, the horizontal component of the equation of motion becomes

$$\frac{dv}{dt} + fkxv + \nabla_\sigma\Phi + \sigma\alpha\nabla\pi = F , \tag{2.17}$$

where

$$\frac{d}{dt} = \left(\frac{\partial}{\partial t}\right)_\sigma + v\cdot\nabla_\sigma + \dot{\sigma}\frac{\partial}{\partial\sigma} . \tag{2.18}$$

f is the vertical component of Coriolis vector ($=2\Omega\sin\phi$), Ω is the angular velocity of the earth, ϕ the latitude, k the vertical unit vector, and F is the frictional force. With the help of (2.11) and (2.14), we obtain the flux form of the equation of motion

$$\left(\frac{\partial}{\partial t}\right)_\sigma(\pi v) + \nabla_\sigma .(\pi v) + \frac{\partial}{\partial\sigma}(\pi\dot{\sigma}v) + fkx\pi v + \nabla_\sigma(\pi\Phi) - \frac{\partial(\Phi\sigma)}{\partial\sigma}\nabla\pi = \pi F . \tag{2.19}$$

The first law of thermodynamics is written as

$$C_p\frac{dT}{dt} = \omega\alpha + Q , \tag{2.20}$$

where Q is the heating rate per unit mass. With the use of (2.14), the flux form

$$\frac{\partial}{\partial t}(\pi C_p T) + \nabla_\sigma .(\pi v C_p T) + \frac{\partial}{\partial\sigma}(\pi\dot{\sigma}C_p T) = \pi(\omega\alpha + Q) , \tag{2.21}$$

is derived.

Let q be the mixing ratio of either water vapor or ozone. The continuity equation of q is written by

$$\frac{dq}{dt} = S , \tag{2.22}$$

where S is the source of q. The flux form of q is

$$\left(\frac{\partial}{\partial t}\right)_\sigma(\pi q) + \nabla_\sigma .(\pi v q) + \frac{\partial}{\partial\sigma}(\pi\dot{\sigma}q) = \pi S . \tag{2.23}$$

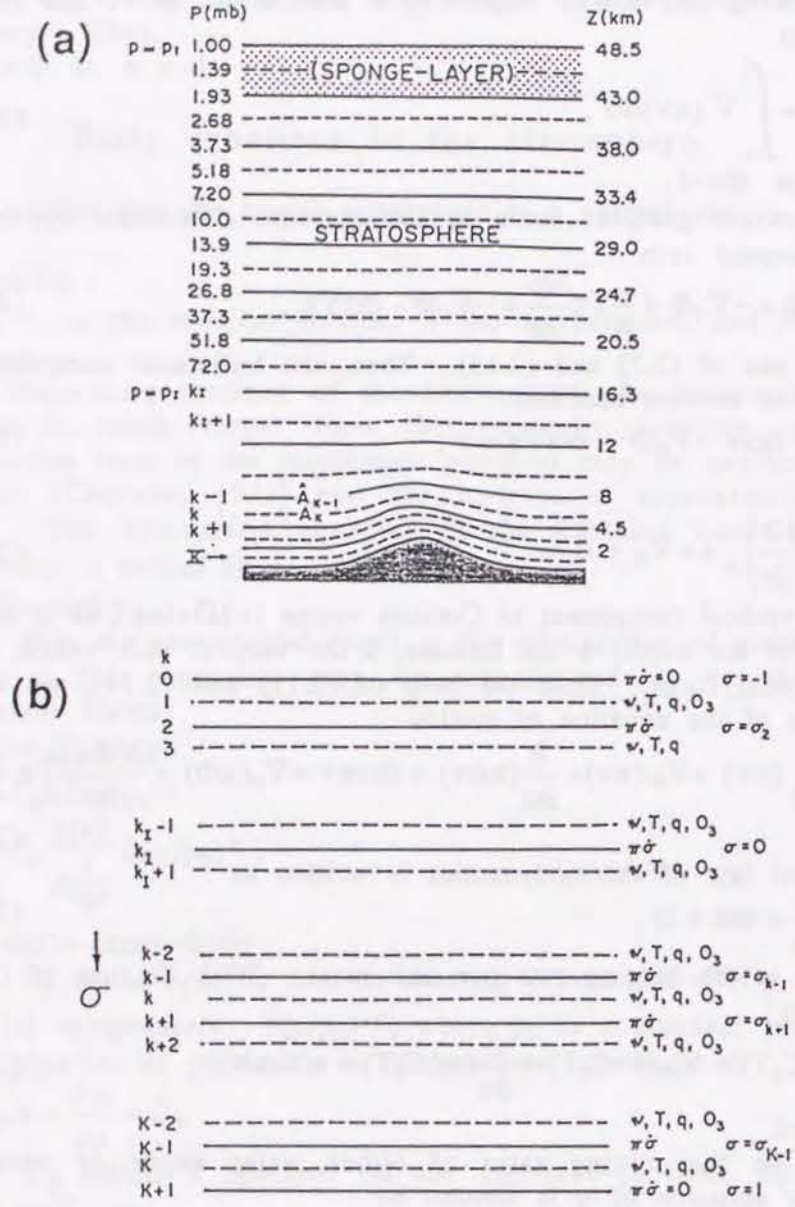

Figure 2.1: (a) The vertical discretization of the twelve layer version of the MRI GCM-I. (b) The vertical indices and the position of vertical levels for the model [Arakawa and Lamb, 1977]. Solid and dashed lines indicate even and odd levels, respectively. The lowest odd level is indicated as **K**. Approximate positions of the levels in km are shown when the surface pressure is 1000 mb.

Figure 2.2: Eight choices of distributing variables on vertical levels. ^ is a reminder that the variable is an interpolated value from the non-hat ones. Scheme C' is adopted in the MRI GCM-I [Tokioka *et al.*, 1984].

2.1.3 The vertical difference scheme

Figure 2.1 (a) and (b) show the vertical structure and indices of the model. The model atmosphere is divided into twelve layers. The lower boundary follows the earth's topography and the upper boundary is the 1 mb pressure surface, which is approximately at the height of the stratopause. In the twelve layer model, we adopt p_I = 100 mb and p_t =1 mb (see eq. (2.2)). From above 100 mb, these coordinate surfaces are also constant pressure surfaces, which are discretized into seven levels with the equal depth in *log p*. Horizontal wind v, mixing ratio of water vapor and ozone, and temperature T are defined at odd levels (midlevel of each layer), while geopotential ϕ and individual time derivative of sigma $\dot{\sigma}$ are defined at even levels (upper or lower surface of each layer). These choice of distributing variables over the vertical grid points are selected following Tokioka [1978].

There are eight choices of distribution of variables on the vertical levels as shown in Figure 2.2, provided that u and v are defined at the same level. Tokioka [1978] studied characteristics of the vertical wave propagations in a simplified situation where there is no basic flow and the basic temperature is uniform in the horizontal direction. By using Boussinesq approximation, a linearized system of equations is then written;

$$\lambda v\hat{u} - 2\Omega \sin\varphi\, \hat{v} = -\frac{\lambda s}{a\cos\varphi}\cdot\frac{\hat{\rho}}{\rho_{00}}, \tag{2.24}$$

$$\lambda v\, \hat{v} + 2\Omega \sin\varphi\, \hat{u} = -\frac{1}{a}\frac{\partial}{\partial\varphi}\left(\frac{\hat{\rho}}{\rho_{00}}\right), \tag{2.25}$$

$$0 = \frac{\partial\hat{p}}{\partial z} - \hat{\rho}g\,, \tag{2.26}$$

$$\lambda v\,\hat{\theta} + \frac{d\theta_0}{dz}\hat{w} = 0\,, \tag{2.27}$$

$$\frac{\lambda s}{a\cos\varphi}\hat{u} + \frac{1}{a\cos\varphi}\frac{\partial}{\partial\varphi}(\cos\varphi\hat{v}) + \frac{\partial\hat{w}}{\partial s} = 0\,, \tag{2.28}$$

$$\hat{\rho} = \frac{\mu}{g}\hat{\theta}\,, \tag{2.29}$$

with

$$\rho - (\rho_{00} + \rho_0) = -\frac{\mu}{g}\left[\theta - \theta_{00} + \theta_0\right], \tag{2.30}$$

where ρ is the air density, θ: the potential temperature, ρ_{00} and θ_{00}: representative values of ρ and θ, ρ_0 and θ_0: basic field of ρ and θ

deviated from ρ_{00} and θ_{00} respectively, and μ is a constant. An infinitesimal quantity ¶' deviated from the basic state is assumed from the following form;

$$¶' = R_e\left[\hat{¶}(\varphi,z)e^{\lambda(vt+s\lambda)}\right], \tag{2.31}$$

where λ is longitude, φ: latitude, z: height, v: frequency, s: zonal wavenumber, a: the radius of the earth, u, v and w are velocity components in λ, φ and z directions respectively. So called vertical structure equation is obtained from equations (2.24)-(2.29) as

$$\frac{d^2 w}{d^2 z} + n^2 w = 0\,, \tag{2.32}$$

where a solution of the form,

$$\hat{w} = W(z)\cdot G(\varphi)\,, \tag{2.33}$$

is assumed and

$$n^2 = \frac{\varepsilon}{4a^2\Omega^2}\cdot\frac{\mu\frac{d\theta_0}{dz}}{\rho_{00}} = \frac{\varepsilon}{4a^2\Omega^2}\left(\frac{-g\frac{d\rho_0}{dz}}{\rho_{00}}\right). \tag{2.34}$$

ε is Lamb's parameter which is often written as $4\Omega^2a^2/gh$, and h is called equivalent depth in the classical tidal theory. The equation (2.32) describes wave propagations, when n^2 is positive, and its solution is written as,

$$W = Ae^{\lambda nz} + Be^{-\lambda nz}\,, \tag{2.35}$$

provided that n is constant with height. Tokioka [1978] derived eight cases of difference analogs which correspond to the variable distributions shown in Fig.2.2 and the equation (2.32). By comparing each scheme with the continuous case (2.34), it is concluded that scheme C' is superior to other schemes since scheme C' describes internal modes as internal and no computational modes appear in the density (temperature) field. As a result, vertical differencing scheme has been derived, based on scheme C', in the MRI GCM-I.

In the upper most layer of the model, a special "sponge term" is included in the thermodynamic equation for suppressing artificial reflection of waves due to the rigid upper boundary condition.

Let A_k be a variable A defined at the odd level k and $\hat{A}_{k+1}$, an interpolated value of A at the even level k+1. We introduce a notation,

$$\frac{D}{Dt}(\pi_k * A_k) \equiv \frac{\partial}{\partial t}(\pi_k A_k) + \nabla\cdot(\pi_k v_k A_k) + \frac{1}{\Delta\sigma_k}\left[(\pi\dot{\sigma})_{k+1}\hat{A}_{k+1} - (\pi\dot{\sigma})_{k-1}\hat{A}_{k-1}\right] \tag{2.36}$$

where ∇ is the horizontal divergence operator and $\Delta\sigma_k \equiv \sigma_{k+1} - \sigma_{k-1}$. The above equation is a flux form of variable A and conserves mass weighted integral of A under the vertical boundary condition

$\dot{\sigma}_0 = \dot{\sigma}_{k+1} = 0$. We define $\widehat{A}_{k+1}$ as

$$\widehat{A}_{k+1} = \frac{(G'_{k+2}\, A_{k+2} - G_{k+2}) - (G'_k\, A_k - G_k)}{G'_{k+2} - G'_k} \tag{2.37}$$

where $G_k \equiv G(A_k)$ is an arbitrary function of variable A_k and $G'_k \equiv dG(A_k)/dA_k$. We can further conserve mass weighted integral of G by using this form. A vertical difference scheme can be constructed that maintains the property of the vertically integrated horizontal pressure gradient force to prevent spurious acceleration of a circulation, total energy conservation under adiabatic and frictionless processes, and conservation of potential temperature θ and $ln\,\theta$, integrated over the entire mass under adiabatic processes (Arakawa and Lamb, 1977).

a. The equation of continuity. The continuity equation, (2.14), may be expressed in a discretized form as

$$\frac{\partial \pi_k}{\partial t} + \nabla\cdot(\pi_k v_k) + \frac{1}{\Delta\sigma_k}[(\pi\dot{\sigma})_{k+1} - (\pi\dot{\sigma})_{k-1}]\,, \tag{2.38}$$

where k is odd and

$$\pi_k = \begin{cases} p_I - p_t\,, & \text{for } k < k_I \\ p_s - p_I\,, & \text{for } k > k_I\,. \end{cases}$$

The above equation is also expressed as

$$\frac{D}{Dt}(\pi_k * 1) = 0. \tag{2.39}$$

b. Pressure Gradient Force. Expression (2.16) becomes

$$\nabla(\pi_k \widehat{\Phi}_k) - \frac{1}{\Delta\sigma_k}(\Phi_{k+1}\,\sigma_{k+1} - \Phi_{k-1}\,\sigma_{k-1})\,\nabla\pi_k\,. \tag{2.40}$$

The above form guarantees that no spurious acceleration of a circulation may occur even in a discretized model with topography (see Arakawa and Lamb, 1977).

c. The first law of thermodynamics If we define temperature at the level k by

$$\left.\begin{aligned} T_k &= \theta_k \cdot P_k \\ P_k &= P_k(p_{k+1}, p_{k-1}) \end{aligned}\right\} \tag{2.41}$$

the following enthalpy equation is derived as a finite difference analog of (2.21);

$$\frac{D}{Dt}(\pi_k * c_p T_k) = \pi_k c_p T_k \frac{\partial \ln P_k}{\partial \pi_k}\left(\frac{\partial}{\partial t} + v\cdot\nabla\right)\pi_k$$

$$+ \frac{1}{\Delta\sigma_k}[(\pi\dot{\sigma})_{k+1}\, c_p(\widehat{T}_{k+1} - P_k\,\widehat{\theta}_{k+1}) - (\pi\dot{\sigma})_{k-1} c_p(P_k\,\widehat{\theta}_{k-1} - \widehat{T}_{k-1})] + \pi_k Q_k\,, \tag{2.42}$$

where P_k is an analog to $(p/p_0)^{\kappa}$ for the level k, $\kappa = R/c_p$, and p_0 is a reference pressure. This is identical to the expression

$$\frac{D}{Dt}(\pi_k * \theta_k) = \frac{Q}{c_p P_k}\,. \tag{2.43}$$

d. The Hydrostatic equation Finite-difference approximations of Equations (2.9) and (2.10) are

$$\widehat{\Phi}_{k+2} - \widehat{\Phi}_k = -\,c_p\,\widehat{\theta}_{k+1}(P_{k+2} - P_k)\,, \tag{2.44}$$

$$\widehat{\Phi}_K = \Phi_s + \sum_{k=k_I+1}^{K}{}' \pi_k c_p T_k \frac{\partial \ln P_k}{\partial \pi_k} - \sum_{k=k_I+1}^{K-2}{}' \sigma_{k+1}\, c_p\, \widehat{\theta}_{K+1}\,(P_{k+2} - P_k)\,, \tag{2.45}$$

where

$$\widehat{\theta}_{k+1} = \frac{\ln(\theta_k/\theta_{k+2})}{1/\theta_{k+2} - 1/\theta_k}\,. \tag{2.46}$$

Σ' in (2.45) represents a summation over odd k. The functional forms of $G(\theta)$ and P_k are

$$G(\theta) = \ln\theta\,, \tag{2.47}$$

$$P_k = (p_k^*/p_0)^{\kappa}, \tag{2.48}$$

$$\left(p_k^*\right)^a = \frac{1}{1+a}\cdot\frac{p_{k+1}^{a+1} - p_{k-1}^{a+1}}{p_{k+1} - p_{k-1}}\,, \tag{2.49}$$

where a=0.2 .

2.1.4 The horizontal difference scheme

The model uses the spherical coordinates, $\zeta=\lambda$ (longitude) and $\eta=\varphi$ (latitude). There are five ways of distributing the dependent variables over the grid points; we adopt so called "Scheme C" which gives the best dispersion relation for inertia-gravity waves [see Arakawa and Lamb, 1977]. Indices "i" and "j" indicate grid position in longitudinal and latitudinal directions respectively. Surface pressure p_s, geopotential ϕ, temperature T, mixing ratios of water vapor q and ozone O_3 , and vertical velocity $\dot{\sigma}$ are defined at the π-point in Fig. 2.3. Since the current grid interval is 4° in latitude and 5° in longitude, the π-grid consists of the points ±2, ±6, ±10, ...,±90 degrees latitude and 0, ±5, ±10, ..., ±180 degrees longitude.

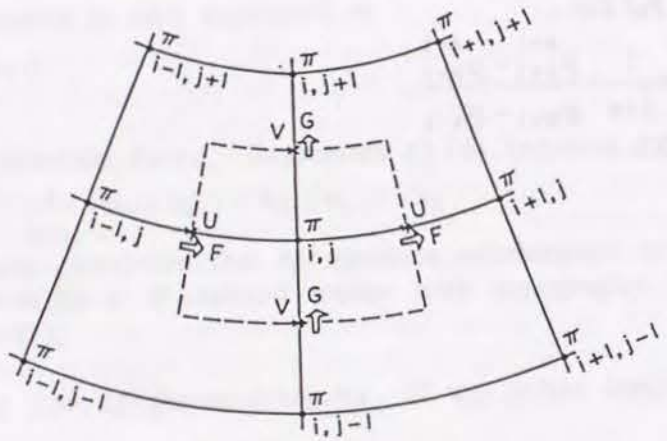

Figure 2.3: Horizontal indices and location of variables. At π-points, all thermodynamic variables, including water vapor and ozone, are calculated [Arakawa and Lamb, 1977].

a. The equation of continuity.

For the continuity equation (2.14), the following form of discretization is adopted

$$\frac{\partial \Pi_{i,j}}{\partial t} + F^k_{i+1/2,j} - F^k_{i-1/2,j} + G^k_{i,j+1/2} - G^k_{i,j-1/2} + \frac{1}{\Delta\sigma_k}(\dot{S}^{k+1}_{i,j} - \dot{S}^{k-1}_{i,j}) = 0 , \quad (2.50)$$

where

$$\Pi \equiv \pi \frac{\Delta\xi\Delta\eta}{m\,n}, \quad F \equiv \pi u \frac{\Delta\eta}{n}, \quad G \equiv \pi v \frac{\Delta\xi}{m}, \quad \dot{S} \equiv \Pi\dot{\sigma},$$

$$m = \frac{1}{a\cos\phi}, \text{ and } n = \frac{1}{a}. \quad (2.51)$$

"m" and "n" are metric factors, while "a" (= 6375 km) is the radius of the earth. The mass flux F and G are defined as follows;

$$\left.\begin{aligned} F^k_{i+1/2,j} &= \frac{1}{2}\overline{(u\frac{\Delta\eta}{n})}^k_{i+1/2,j}(\pi_{i+1,j}+\pi_{i,j}) . \\ G^k_{i,j+1/2} &= \frac{1}{2}\overline{\overline{(v\frac{\Delta\xi}{m})}}^k_{i,j+1/2}(\pi_{i,j+1}+\pi_{i,j}) . \end{aligned}\right\} \quad (2.52)$$

The shingle and the double superior bars are linear smoothing operators in ξ. These operators are introduced to the model to avoid short time interval for computational stability since the grid interval in the east-west direction decreases at high latitudes (see Arakawa and Lamb [1977] and Tokioka *et al.* [1984]).

b. The pressure gradient force.

As seen from (2.16), the pressure force in σ- coordinate is expressed by the sum of two terms; the individual terms are large but with opposite sign in regions with steep mountains. Therefore special attentions are paid to discretize these terms. The pressure gradient force in the ξ-direction is

$$-\frac{\pi}{n}\left[\frac{\partial\Phi}{\partial\xi} + \sigma\alpha\frac{\partial\pi}{\partial\xi}\right].$$

For the first term, we choose the form:

$$-\left(\frac{\pi}{n}\frac{\partial\Phi}{\partial\xi}\right)^k_{i+1/2,j} = \frac{1}{\Delta\xi\Delta\eta}\left(\frac{\Delta\eta}{n}\right)_j \frac{1}{2}(\pi_{i+1,j}+\pi_{i,j})(\hat{\Phi}^k_{i+1,j} - \hat{\Phi}^k_{i,j}) . \quad (2.53)$$

As for the second term, the following form is chosen to be consistent with (2.53),

$$-\left(\frac{\pi\sigma\alpha}{n}\frac{\partial\pi}{\partial\xi}\right)^k_{i+1/2,j}=\frac{1}{\Delta\xi\Delta\eta}\left(\frac{\Delta\eta}{n}\right)_j\frac{1}{2}\overline{\{(\pi\sigma\alpha)^k_{i+1,j}+(\pi\sigma\alpha)^k_{i,j}\}(\pi_{i+1,j}-\pi_{i,j})}\,. \quad (2.54)$$

By adding (2.53) and (2.54), we can show that the integral properties (2.40) are maintained.

Similarly, the pressure gradient force in the η-direction is

$$-\left(\frac{\Delta\xi}{m}\right)_{j+1/2}\cdot\frac{1}{2}\left[\overline{(\pi_{i,j+1}+\pi_{i,j})(\hat{\Phi}^k_{i,j+1}-\hat{\Phi}^k_{i,j})}+\overline{\{(\pi\sigma\alpha)^k_{i,j+1}+(\pi\sigma\alpha)^k_{i,j}\}(\pi_{i,j+1}-\pi_{i,j})}\right]. \quad (2.55)$$

c. Kinetic energy generation and the first law of thermodynamics

The contribution of the pressure gradient force to the kinetic energy generation, $\partial/\partial t\left(\Pi\frac{1}{2}u^2\right)^k_{i+1/2,j}$, is obtained by multiplying (2.53) and (2.54) by $u^k_{i+1/2,j}$. Then the kinetic energy generation is

$$-\frac{1}{2}\left(u\frac{\Delta\eta}{n}\right)^k_{i+1/2,j}\left[\overline{(\pi_{i+1,j}+\pi_{i,j})(\hat{\Phi}^k_{i+1,j}-\hat{\Phi}^k_{i,j})}+\overline{\{(\pi\sigma\alpha)^k_{i+1,j}+(\pi\sigma\alpha)^k_{i,j}\}(\pi_{i+1,j}-\pi_{i,j})}\right]. \quad (2.56)$$

As the superior bar indicates a linear smoothing operator in ξ, it can be shown that the summation of (2.56) over "i" is identical to

$$-\frac{1}{2}\overline{\left(u\frac{\Delta\eta}{n}\right)^k_{i+1/2,j}}\left[(\pi_{i+1,j}+\pi_{i,j})(\hat{\Phi}^k_{i+1,j}-\hat{\Phi}^k_{i,j})+\{(\pi\sigma\alpha)^k_{i+1,j}+(\pi\sigma\alpha)^k_{i,j}\}(\pi_{i+1,j}-\pi_{i,j})\right]. \quad (2.57)$$

By using the definition of F given by (2.52), the above equation becomes (2.57) =

$$-F^k_{i+1/2,j}(\hat{\Phi}^k_{i+1,j}-\hat{\Phi}^k_{i,j})-\frac{1}{2}\overline{\left(u\frac{\Delta\eta}{n}\right)^k_{i+1/2,j}}\{(\pi\sigma\alpha)^k_{i+1,j}+(\pi\sigma\alpha)^k_{i,j}\}(\pi_{i+1,j}-\pi_{i,j})\,.$$

Therefore we can show that

$$\sum_i(2.57)=\sum_i(F^k_{i+1/2,j}-F^k_{i-1/2,j})\hat{\Phi}^k_{i,j}$$
$$-\frac{1}{4}\overline{\left(u\frac{\Delta\eta}{n}\right)^k_{i+1/2,j}}\{(\pi\sigma\alpha)^k_{i+1,j}+(\pi\sigma\alpha)^k_{i,j}\}(\pi_{i+1,j}-\pi_{i,j})$$
$$-\frac{1}{4}\overline{\left(u\frac{\Delta\eta}{n}\right)^k_{i-1/2,j}}\{(\pi\sigma\alpha)^k_{i,j}+(\pi\sigma\alpha)^k_{i-1,j}\}(\pi_{i,j}-\pi_{i-1,j})\,. \quad (2.59)$$

Similarly, the contribution of the pressure gradient force to $\partial/\partial t\left(\Pi\frac{1}{2}v^2\right)^k_{i,j}$ is given by

$$\sum_j(G^k_{i,j+1/2}-G^k_{i,j-1/2})\hat{\Phi}^k_{i,j}-\frac{1}{4}\overline{\left(v\frac{\Delta\xi}{m}\right)^k_{i,j+1/2}}\{(\pi\sigma\alpha)^k_{i,j+1}+(\pi\sigma\alpha)^k_{i,j}\}(\pi_{i,j+1}-\pi_{i,j})$$
$$-\frac{1}{4}\overline{\left(v\frac{\Delta\xi}{m}\right)^k_{i,j-1/2}}\{(\pi\sigma\alpha)^k_{i,j}+(\pi\sigma\alpha)^k_{i,j-1}\}(\pi_{i,j}-\pi_{i,j-1})\,. \quad (2.60)$$

Then $\sum_j(2.59)+\sum_i(2.60)$ give the discrete form of the total kinetic energy generation by the pressure gradient force, $-\pi v\cdot\left[\nabla_\sigma\Phi+\sigma\alpha\nabla\pi\right]$.

The thermodynamic energy equation (2.42) may be written in a discretized form by using the continuity equation as

$$\frac{\partial}{\partial t}\left(\Pi_{i,j}T^k_{i,j}\right)+F^k_{i+1/2,j}\frac{T^k_{i+1,j}+T^k_{i,j}}{2}-F^k_{i-1/2,j}\frac{T^k_{i,j}+T^k_{i-1,j}}{2}$$
$$+G^k_{i,j+1/2}\frac{T^k_{i,j+1}+T^k_{i,j}}{2}-G^k_{i,j-1/2}\frac{T^k_{i,j}+T^k_{i,j-1}}{2}+\frac{1}{\Delta\sigma_k}[\dot{S}^{k+1}_{i,j}P^k_{i,j}\hat{\theta}^{k+1}_{i,j}-\dot{S}^{k-1}_{i,j}P^k_{i,j}\hat{\theta}^{k-1}_{i,j}]$$
$$=\frac{1}{c_p}\left[(\pi\sigma\alpha)^k_{i,j}\frac{\partial\Pi_{i,j}}{\partial t}+\frac{1}{4}\overline{\left(u\frac{\Delta\eta}{n}\right)}_{i+1/2,j}\{(\pi\sigma\alpha)^k_{i+1,j}+(\pi\sigma\alpha)^k_{i,j}\}(\pi_{i+1,j}-\pi_{i,j})\right.$$
$$+\frac{1}{4}\overline{\left(u\frac{\Delta\eta}{n}\right)}_{i-1/2,j}\{(\pi\sigma\alpha)^k_{i,j}+(\pi\sigma\alpha)^k_{i-1,j}\}(\pi_{i,j}-\pi_{i-1,j})$$
$$+\frac{1}{4}\overline{\overline{\left(v\frac{\Delta\xi}{m}\right)}}_{i,j+1/2}\{(\pi\sigma\alpha)^k_{i,j+1}+(\pi\sigma\alpha)^k_{i,j}\}(\pi_{i,j+1}-\pi_{i,j})$$
$$\left.+\frac{1}{4}\overline{\overline{\left(v\frac{\Delta\xi}{m}\right)}}_{i,j-1/2}\{(\pi\sigma\alpha)^k_{i,j}+(\pi\sigma\alpha)^k_{i,j-1}\}(\pi_{i,j}-\pi_{i,j-1})+\Pi_{i,j}Q^k_{i,j}\right] \quad (2.61)$$

d. Momentum fluxes

From the flux form of the equation of motion (2.19), we choose for

$$\frac{\partial}{\partial t}\left(\pi\frac{\Delta\xi\Delta\eta}{m\,n}u\right)+\Delta\xi\frac{\partial}{\partial\xi}\left(\pi u\frac{\Delta\eta}{n}u\right)+\Delta\eta\frac{\partial}{\partial\eta}\left(\pi v\frac{\Delta\xi}{m}u\right)+\frac{\partial}{\partial\sigma}\left(\pi\dot{\sigma}\frac{\Delta\xi\Delta\eta}{m\,n}u\right)$$

the form,

$$\frac{\partial}{\partial t}(\Pi^{(u)}_{i,j}u^k_{i,j})+\frac{1}{2}\left[F^{(u)}_{i+1/2,j}(u_{i+1,j}+u_{i,j})-F^{(u)}_{i-1/2,j}(u_{i,j}+u_{i-1,j})\right.$$
$$+G^{(u)}_{i,j+1/2}(u_{i,j+1}+u_{i,j})-G^{(u)}_{i,j-1/2}(u_{i,j}+u_{i,j-1})$$
$$\left.+\tilde{F}^{(u)}_{i+1/2,j+1/2}(u_{i+1,j+1}+u_{i,j})-\tilde{F}^{(u)}_{i-1/2,j-1/2}(u_{i,j}+u_{i-1,j-1})\right.$$

$$+\tilde{G}^{(u)}_{i-1/2,j+1/2}(u_{i-1,j+1}+u_{i,j})-\tilde{G}^{(u)}_{i+1/2,j-1/2}(u_{i,j}+u_{i+1,j-1})\Big]^k$$
$$+\frac{1}{\Delta\sigma_k}\cdot\frac{1}{2}\Big[\dot{S}^{(u)\ k+1}_{i,j}(u^{k+2}_{i,j}+u^{k}_{i,j})-\dot{S}^{(u)\ k-1}_{i,j}(u^{k}_{i,j}+u^{k-2}_{i,j})\Big], \quad (2.62)$$

where $\Pi^{(u)}$, $\dot{S}^{(u)}$, $F^{(u)}$, $G^{(u)}$, $\tilde{F}^{(u)}$ and $\tilde{G}^{(u)}$ are not defined yet. When u is constant both in space and time, (2.62) should be zero. Then we get a continuity equation,

$$\frac{\partial\Pi^{(u)}_{i,j}}{\partial t}+\left(F^{(u)}_{i+1/2,j}-F^{(u)}_{i-1/2,j}+G^{(u)}_{i,j+1/2}-G^{(u)}_{i,j-1/2}\right)^k$$
$$+\left(\tilde{F}^{(u)}_{i+1/2,j+1/2}-\tilde{F}^{(u)}_{i-1/2,j-1/2}+\tilde{G}^{(u)}_{i-1/2,j+1/2}-\tilde{G}^{(u)}_{i+1/2,j-1/2}\right)^k+\frac{1}{\Delta\sigma_k}\left(\dot{S}^{(u)\ k+1}_{i,j}-\dot{S}^{(u)\ k-1}_{i,j}\right)=0. \quad (2.63)$$

Let us define F^* and G^*, at π-points, by

$$\left.\begin{aligned}F^*_{i,j}&=\frac{1}{2}(F_{i+1/2,j}+F_{i-1/2,j})\\ G^*_{i,j}&=\frac{1}{2}(G_{i,j+1/2}+G_{i,j-1/2})\end{aligned}\right\}. \quad (2.64)$$

Arakawa proposed the following forms based on two dimensional nondivergent flow (see Arakawa and Lamb, 1977).

$$\left.\begin{aligned}F^{(u)}_{i+1/2,j}&=\frac{1}{6}(F^*_{i+1/2,j+1}+2F^*_{i+1/2,j}+F^*_{i+1/2,j-1})\\ G^{(u)}_{i,j+1/2}&=\frac{1}{6}(G^*_{i+1/2,j}+G^*_{i+1/2,j+1}+G^*_{i-1/2,j}+G^*_{i-1/2,j+1})\\ \tilde{F}^{(u)}_{i+1/2,j+1/2}&=\frac{1}{12}(G^*_{i+1/2,j}+G^*_{i+1/2,j+1}+F^*_{i+1/2,j}+F^*_{i+1/2,j+1})\\ \tilde{G}^{(u)}_{i-1/2,j+1/2}&=\frac{1}{12}(G^*_{i-1/2,j}+G^*_{i-1/2,j+1}-F^*_{i-1/2,j}-F^*_{i-1/2,j+1})\end{aligned}\right\}. \quad (2.65)$$

By using (2.64) and (2.65), equation (2.63) is consistent with the continuity equation (2.50) provided that

$$\Pi^{(u)}_{i+1/2,j}=\frac{1}{8}\left[\Pi_{i+1,j+1}+\Pi_{i,j+1}+\Pi_{i,j-1}+\Pi_{i+1,j-1}+2(\Pi_{i+1,j}+\Pi_{i,j})\right], \quad (2.66)$$

and

$$\dot{S}^{(u)}_{i+1/2,j}=\frac{1}{8}\left[\dot{S}_{i+1,j+1}+\dot{S}_{i,j+1}+\dot{S}_{i,j-1}+\dot{S}_{i+1,j-1}+2(\dot{S}_{i+1,j}+\dot{S}_{i,j})\right]. \quad (2.67)$$

As a result, the conservation of kinetic energy under a pure advective process is maintained with above momentum flux forms.

For v-component, we use a form identical to (2.62), but u replaced by v. The definition corresponding to (2.65)–(2.67) are then

$$\left.\begin{aligned}F^{(v)}_{i+1/2,j}&=\frac{1}{6}(F^*_{i+1,j+1/2}+F^*_{i+1,j-1/2}+F^*_{i,j+1/2}+F^*_{i,j-1/2})\\ G^{(v)}_{i,j+1/2}&=\frac{1}{6}(G^*_{i+1,j+1/2}+2G^*_{i,j+1/2}+G^*_{i,j-1/2})\\ \tilde{F}^{(v)}_{i+1/2,j+1/2}&=\frac{1}{12}(G^*_{i+1,j+1/2}+G^*_{i,j+1/2}+F^*_{i+1,j+1/2}+F^*_{i,j+1/2})\\ \tilde{G}^{(v)}_{i-1/2,j+1/2}&=\frac{1}{12}(G^*_{i,j+1/2}+G^*_{i-1,j+1/2}-F^*_{i,j+1/2}-F^*_{i-1,j+1/2})\end{aligned}\right\}, \quad (2.68)$$

$$\Pi^{(v)}_{i,j+1/2}=\frac{1}{8}\left[\Pi_{i+1,j+1}+\Pi_{i+1,j}+\Pi_{i-1,j+1}+\Pi_{i-1,j}+2(\Pi_{i,j+1}+\Pi_{i,j})\right], \quad (2.69)$$

$$\dot{S}^{(v)}_{i,j+1/2}=\frac{1}{8}\left[\dot{S}_{i+1,j+1}+\dot{S}_{i+1,j}+\dot{S}_{i-1,j+1}+\dot{S}_{i-1,j}+2(\dot{S}_{i,j+1}+\dot{S}_{i,j})\right]. \quad (2.70)$$

In case of two-dimensional incompressible flow, some of the important integral constraints, such as the conservation of (global) mean kinetic energy, mean square vorticity, and mean vorticity, can be maintained by the flux form described above; they inhibit spurious energy cascade to smaller scale disturbances, thereby preventing nonlinear computational instability.

e. Coriolis force

Coriolis force plus the metric term which contributes to $\frac{\partial}{\partial t}(\Pi u)$ is

$$\left[f\frac{\Delta\xi\Delta\eta}{m\,n}-u\Delta\xi\Delta\eta\frac{\partial}{\partial\eta}\left(\frac{1}{m}\right)\right]\pi v \quad (2.71)$$

and the Coriolis force which contributes to $\frac{\partial}{\partial t}(\Pi v)$ is

$$-\left[f\frac{\Delta\xi\Delta\eta}{m\,n}-u\Delta\xi\Delta\eta\frac{\partial}{\partial\eta}\left(\frac{1}{m}\right)\right]\pi u \quad (2.72)$$

Defining $C^k_{i,j}$ at π-point as follows,

$$C^k_{i,j}=f_j\left(\frac{\Delta\xi\Delta\eta}{m\,n}\right)_j-\frac{1}{2}\left(u_{i+1/2,j}+u_{i-1/2,j}\right)^k\left\{\left(\frac{\Delta\xi}{m}\right)_{j+1/2}-\left(\frac{\Delta\xi}{m}\right)_{j-1/2}\right\}. \quad (2.73)$$

we express (2.71), at u-point (i+1/2, j), in the following way,

$$\frac{1}{4}\left[\pi_{i+1,j}C^k_{i+1,j}\left(v_{i+1,j+1/2}+v_{i+1,j-1/2}\right)^k+\pi_{i,j}C^k_{i,j}\left(v_{i,j+1/2}+v_{i,j-1/2}\right)^k\right]. \quad (2.74)$$

(2.72), at v-point (i, j+1/2), is expressed as

$$-\frac{1}{4}\left[\pi_{i,j+1}C^{k}_{i,j+1}\left(u_{i+1/2,j+1}+u_{i-1/2,j+1}\right)^{k}+\pi_{i,j}C^{k}_{i,j}\left(u_{i+1/2,j}+u_{i-1/2,j}\right)^{k}\right]\cdot \quad (2.75)$$

It can be confirmed from (2.74) and (2.75) that the choice of differencing does not lead any false generation of kinetic energy through Coriolis force.

2.1.5 Time integration

Various time difference schemes have been developed to carry out time integration correctly and stably [see Haltiner, 1980]. To explain the procedure adopted in the MRI GCM, we write the equations symbolically in the following form:

$$\frac{dA}{dt}=f(A)\,. \quad (2.76)$$

As shown in Figure 2.4, the time integration scheme consists of *leapfrog step* (L),

$$\frac{\left(A^{\tau+1}-A^{\tau-1}\right)}{2\Delta t}=f(A^{\tau})\,, \quad (2.77)$$

and the Matsuno (Euler backward) step (M),

$$\frac{\left(A^{*\tau+1}-A^{\tau}\right)}{\Delta t}=f(A^{\tau})\,, \quad (2.78)$$

$$\frac{\left(A^{\tau+1}-A^{\tau}\right)}{\Delta t}=f(A^{*\tau+1})\,. \quad (2.79)$$

Equation (2.76) states that the value of A at a future time (τ+1) can be obtained from present (τ) and previous (τ-1) values of A. Therefore the central difference scheme (2.76) is commonly referred as the *leapfrog method*. Equation (2.78) indicates the forward time step while equation (2.79) is the backward time step which tends to suppress the high-frequency inertial-gravitational oscillations. $A^{*\tau+1}$ is a value to be estimated at the first time step just after the calculation of diabatic processes and used only in the Matsuno step. The *leapfrog scheme* is quite accurate and has some desirable characteristics; however, its solution at adjacent time steps tends to become decoupled, primarily because of the computational mode which changes phase at every time step. Therefore, Matsuno scheme is inserted, which has damping effect and suppresses "noise" generated by the diabatic process [*e.g.*, Haltiner, 1980].

. In this study the basic time step Δt is 7.5 minutes. The calculations of the diabatic terms (Q) including ozone source and sink, and the vertical advection of ozone and water vapor are done in every eight time steps, that is one hour (Δt_d), as shown by the arrows.

In this study the basic time step Δt is 7.5 minutes. The calculations of the diabatic terms (Q) including ozone source and sink, and the vertical advection of ozone and water vapor are done in every eight time steps, that is one hour (Δt_d), as shown by the arrows.

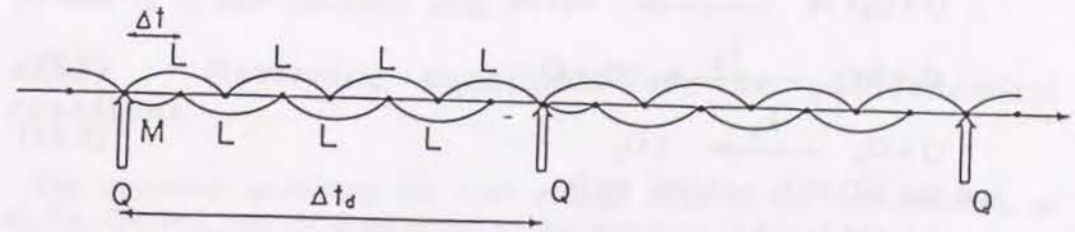

Figure 2.4: Time integration scheme. M indicates Matsuno step and L, leapfrog step.

2.2 Ozone photochemistry and surface destruction

In this section ozone photochemical process in the stratosphere and the ozone destruction by heterogeneous chemical reactions near the earth's surface are described.

2.2.1 Photochemical reactions

The photochemical production and destruction of ozone in the stratosphere is comprised of both the Chapman reactions

$$O_2 + h\nu \xrightarrow{j_1} 2O \qquad (2.80)$$

$$O + O_2 + M \xrightarrow{k_1} O_3 + M \qquad (2.81)$$

$$O_3 + h\nu \xrightarrow{j_2} O_2 + O \qquad (2.82)$$

$$O + O_3 \xrightarrow{k_2} 2\,O_2 \qquad (2.83)$$

and the NO-NO_2 catalytic cycle

$$NO + O_3 \xrightarrow{k_3} NO_2 + O_2 \qquad (2.84)$$

$$NO_2 + O \xrightarrow{k_4} NO + O_2 \qquad (2.85)$$

$$NO_2 + h\nu \xrightarrow{j_3} NO + O. \qquad (2.86)$$

The chemical reaction rates k_i are

$$\begin{aligned} k_1 &= 1.1\times 10^{-46} \exp(520/T) && m^6\,s^{-1}, \\ k_2 &= 1.9\times 10^{-17} \exp(-2300/T) && m^3\,s^{-1}, \\ k_3 &= 2.1\times 10^{-18} \exp(-1450/T) && m^3\,s^{-1}, \\ k_4 &= 9.1\times 10^{-18} && m^3\,s^{-1}, \end{aligned} \qquad (2.87)$$

and the photodissociation rate $j_n(p)$ of species n at pressure p is given by

$$j_n(p) = \int_0^\infty \alpha_n(\lambda)\, I_0(\lambda) \exp\left[-M_F \sum_{m=1}^{2} \alpha_m(\lambda)\, U_m(p)\right] d\lambda . \qquad (2.88)$$

Here $\alpha_n(\lambda)$ is the absorption cross section of species n(1: O_2 , 2: O_3 , 3: NO_2) at wavelength λ, $I_0(\lambda)$ is the extraterrestrial monochromatic photon flux per unit wavelength. M_F is a magnification factor to account for the departure from the plane parallel atmosphere, which will define by (2.139) in section 2.3.6, and U_m is the absorber amount of species m(1: O_2 , 2: O_3) in a vertical column above pressure p, and the summation extends over all species m. To calculate the photodissociation rate $j_n(p)$, the value of $\alpha_1(\lambda)$, $\alpha_2(\lambda)$, and $I_0(\lambda)$ are taken from Ackerman [1971], Kockarts [1971], and $\alpha_3(\lambda)$ from the data of The natural Stratosphere of 1974, CIAP Monograph 1. Currently $j_n(p)$ is computed by a linear bivariate interpolation of precomputed values of $j_n(p)$ as a function of U_1 and U_2 to save computer time.

2.2.2 Governing equations for the photochemical reactions

The equations governing the time change rates of the concentration of O, O_2, O_3, NO, and NO_2 are given by the reactions (2.80)-(2.86), *i.e.*,

$$\frac{\partial[O]}{\partial t} = 2j_1[O]_2 - k_1[O][O]_2[M] + j_2[O]_3 - k_2[O][O]_3 - k_4[O][NO]_2 + j_3[NO]_2 , \qquad (2.89)$$

$$\frac{\partial[O_2]}{\partial t} = -j_1[O]_2 - k_1[O][O]_2[M] + j_2[O]_3 + 2k_2[O][O]_3 + k_3[NO][O]_3 + k_4[NO]_2[O] , \qquad (2.90)$$

$$\frac{\partial[O_3]}{\partial t} = k_1[O][O]_2[M] - j_2[O]_3 - k_2[O][O]_3 - k_3[NO][O]_3 \qquad (2.91)$$

$$\frac{\partial[NO]}{\partial t} = -k_3[NO][O]_3 - k_4[NO]_2[O] + j_3[NO]_2 , \qquad (2.92)$$

$$\frac{\partial[NO_2]}{\partial t} = k_3[NO][O]_3 - k_4[NO]_2[O] - j_3[NO]_2 , \qquad (2.93)$$

where [X] denotes the concentration of species X in molecules m^{-3} and M represents that of air. The equilibrium concentration of atomic oxygen O and nitric monoxide NO are calculated from (2.89) and (2.92), *i.e.*,

$$[O]_e = \frac{2j_1[O]_2 + j_2[O]_3 + j_3[NO]_2}{k_1[O]_2[M] + k_2[O]_3 + k_4[NO]_2} , \qquad (2.94)$$

$$[NO]_e = \frac{k_4[NO]_2\,[O] + j_3[NO]_2}{k_3[O]_3}, \qquad (2.95)$$

where the subscript " e" indicates the equilibrium value.

The relaxation times are approximately given by $\tau_0 \approx (k_1[O_2][M])^{-1}$ and $\tau_{NO} \approx (k_3[O_3])^{-1}$; their representative values are order 1 minute and 10 minutes, respectively. Then, it can be assumed that O and NO are in euilibrium with other constituents, and we can approximate $[O]_e$ and $[NO]_e$ instead of [O] and [NO].

Substituting (2.94) and (2.95) into (2.91) gives,

$$\frac{\partial[O_3]}{\partial t} = A - B\,[O_3] - C\,[O_3]^2, \qquad (2.96)$$

where

$$A = 2\frac{k_1 j_1[O_2]^2[M] - k_4 j_1[O_2][NO_2] - k_4 j_3[NO_2]^2}{k_1[O_2][M] + k_2[O_3] + k_4[NO_2]},$$

$$B = 2\frac{k_2 j_1[O_2] + (k_2 j_3 + k_4 j_2)[NO_2]}{k_1[O_2][M] + k_2[O_3] + k_4[NO_2]},$$

$$C = 2\frac{k_2 j_2}{k_1[O_2][M] + k_2[O_3] + k_4[NO_2]}.$$

$[O_2]$ can be given as $[O_2] = 0.21[M]$, and $[NO_2]$ is prescribed to vary only in the vertical with the relation

$$[NO_2](z) = \beta\,[NO_2]_{McElroy}(z), \qquad (2.97)$$

where $[NO_2]_{McElroy}(z)$ is the one-dimensional profile calculated by McElroy et al.[1974], and β is an empirical constant to adjust the simulated O_3 mixing ratio to the observed value at 10 mb in the tropics. Currently β is set to 1.62.

2.2.3 Ozone destruction at the earth's surface

Ozone is destroyed at the earth's surface by heterogeneous chemical reactions. The rate of destruction D_{O3} may be expressed as

$$D_{O3} = \rho\,K\,(q_{O3})_S, \qquad (2.98)$$

where ρ is the air density, K the reaction rate constant, $(q_{O3})_S$ the surface ozone mixing ratio. We assume that the destruction D_{O3} is approximately compensated by the downward ozone flux at the top of the planetary boundary layer, $(F_{O3})_B$, which may be approximated as

$$(F_{O3})_B = \rho D\frac{\partial q_{O3}}{\partial Z} \approx \rho D\frac{(q_{O3})_{LM} - (q_{O3})_S}{Z_{LM} - Z_S}, \qquad (2.99)$$

where D is the eddy diffusivity at the top of the planetary boundary layer, Z the altitude, and subscript LM denotes the midlevel of the

lowest layer. $(q_{O3})_S$ is determined by equating (2.98) with (2.99) as

$$(q_{O3})_S = \frac{D}{D + K(Z_{LM} - Z_S)}\,(q_{O3})_{LM}. \qquad (2.100)$$

The constants K and D are currently assigned to 0.0008 m sec^{-1} and 10 m^2 sec^{-1} after Cunnold *et al.* [1975].

2.3 Radiation

Diurnal variations in GCMs as well as tidal forcings are resulted from radiational processes in each model. To calculated radiative fluxes, we should have to solve radiative transfer equations in various conditions appeared in the model. This is, however, quite time-consuming process and have to be parameterized especially in three dimensional models. The radiation calculation scheme adopted in the MRI GCM-I closely follows the one described Arakawa and Mintz [1974]. The solar radiation incident on the top of the model atmosphere has both seasonal and diurnal variations. In the model, the solar flux under cloudless conditions is depleted by ozone absorption, water vapor absorption, and Rayleigh scattering. The model forms interactive clouds, such as clouds by large scale condensation and cirrus. They influence the radiational heating fields strongly by absorption and reflection. The albedo of the earth's surface is determined diagnostically by the model as a simple function of surface conditions.

The parameterization of the solar radiation is based on Katayama [1972]. The solar radiation is divided into two parts at the wavelength $\lambda = \lambda_c \equiv 0.9\ \mu$.

i) The part $\lambda > \lambda_c$ is called "scattered" part, where Rayleigh scattering is considered above the 200 mb level.

ii) The part $\lambda < \lambda_c$ is called "absorbed" part, where absorption by water vapor is dominant and Rayleigh scattering is negligible below the 200 mb level.

For the longwave (terrestrial) radiation, we adopt a hybrid scheme proposed by Schlesinger [1976]; the scheme consist of two different methods which are connected with each other at the 10 mb (≈ 30 km) level.

1) From the surface up to the 30 km level, we use the method developed by Katayama [1972]; weighted mean transmission function defined for the entire band are used to calculate longwave flux and its flux divergence. Water vapor, carbon dioxide and ozone are treated as absorbers.

2) Above the 30 km level, we adopt the longwave radiative cooling parameterization developed by Dickinson [1973].

2.3.1 Terrestrial radiation

The upward and the downward fluxes of terrestrial (longwave)

radiation, $R_z^{\uparrow}$, and $R_z^{\downarrow}$ are given by;

$$R_z^{\downarrow} = \int_0^{\infty} \pi B_\nu(T_z)\, d\nu + \int_0^{\infty} d\nu \int_{T_z}^{T_T} \pi \frac{dB_\nu(T)}{dT} \tau_f \left\{\ell_\nu (u - u_z)\right\} dT - \int_0^{\infty} \pi B_\nu(T_T)\, \tau_f \left\{\ell_\nu (u_\infty - u_z)\right\} d\nu , \tag{2.101}$$

$$R_z^{\uparrow} = \int_0^{\infty} \pi B_\nu(T_z)\, d\nu + \int_0^{\infty} d\nu \int_{T_z}^{T_g} \pi \frac{dB_\nu(T)}{dT} \tau_f \left\{\ell_\nu (u_z - u)\right\} dT . \tag{2.102}$$

where u_z (= $u(T_z)$) is the effective amount of absorbing medium (water vapor, carbon dioxide, and ozone) in the vertical air column from the earth's surface to the level z, T_z the temperature at level z, T_g the ground temperature, B_ν the Plank's radiation function expressed in terms of frequency ν, ℓ_ν the absorption coefficient, τ_f the transmission function of a slab at frequency ν, T_T the temperature of the effective lid of the model atmosphere. In the 12 layer version of the MRI GCM-I, the longwave flux is calculated up to the 10 mb level, therefore T_T is defined as the vertical mean temperature above 10 mb level.

The net upward flux R_z is defined as

$$R_z = R_z^{\uparrow} - R_z^{\downarrow} . \tag{2.103}$$

The longwave radiational heating rate is, therefore given by

$$\left(\frac{\partial T}{\partial t}\right)_{tr} = \frac{g}{C_p} \frac{\partial R_z}{\partial p} , \tag{2.104}$$

where g is the acceleration of gravity and C_p is the specific heat of air at constant pressure.

In order to simplify the computation of equation (2.101) and (2.102), Yamamoto [1952] introduced the following weighted mean transmission functions.

$$\tau(u^*,T) \equiv \left[\pi \frac{dB(T)}{dT}\right]^{-1} \int_0^{\infty} \pi \frac{dB_\nu(T)}{dT} \tau_f \left\{\ell_{\nu,0} u^*\right\} d\nu , \tag{2.105}$$

and

$$\tilde{\tau}(u^*,T) \equiv \left[\pi B(T)\right]^{-1} \int_0^{\infty} \pi B_\nu(T)\, \tau_f \left\{\ell_{\nu,0} u^*\right\} d\nu , \tag{2.106}$$

where

$$\pi B(T) = \int_0^\infty \pi B_\nu(T)\, d\nu = \sigma T^4 ,$$

$$\ell_{\nu,0} u^* = \ell_\nu u ,$$

and σ is the Stefan-Boltzmann constant, $\ell_{\nu,0}$ the absorption coefficient at the standard pressure p_0. The effective absorber amount u^* is given by

$$u_n^*(p) = \frac{1}{g}\int_p^{p_s} q_n(p')\left(\frac{p'}{p_0}\right)^{\alpha_n} dp' , \qquad (2.107)$$

where p_s is the surface pressure, q_n the absorber mixing ratio, and n is a symbol of either H_2O, CO_2, or O_3. Pressure scaling lows were originally incorporated to replace an inhomogeneous optical path with an equivalent homogeneous optical path. Since this is an empirical method, there is some uncertainty in the value of the pressure scaling factor α_n ; the value used in the MRI GCM-I is given in Table 2.1.

Table 2.1. Pressure scaling factors, α_n, adopted in the MRI GCM-I for water vapor, carbon dioxide, and ozone.

α_{H_2O}	0.9	McClatchey *et al.* [1972]
α_{CO_2}	0.86	Manabe and Möller [1961]
α_{O_3}	0.3	Manabe and Möller [1961]

Yamamoto [1952] found for water vapor that the dependence of $\tau(u^*,T)$ on temperature is weak in between 210°K and 320°K. Furthermore, according to Schlesinger [1976], the temperature dependence of τ on carbon dioxide and ozone is weak in between 190°K and 310°K. Therefore we introduce the following approximation,

$$\tau(u^*,T) \approx \tau(u^*,\overline{T}) \qquad \text{for } T \geq T_c = 220°K , \qquad (2.108)$$

where $\overline{T} = 260°K$.

With the use of (2.108), equations (2.101) and (2.102) are transformed into the following form,

$$R_z^{\downarrow} = \pi B_z - \pi B_c\, \tilde{\tau}(u_\infty^* - u_z^*, T_c) - (\pi B_T - \pi B_c)\, \tau(u_\infty^* - u_z^*, T) + \int_{\pi B_z}^{\pi B_T} \tau(u^* - u_z^*, \overline{T})\, d(\pi B) , \qquad (2.109)$$

and

$$R_z^{\uparrow} = \pi B_z + \int_{\pi B_z}^{\pi B_g} \tau(u_z^* - u^*, \overline{T})\, d(\pi B) , \qquad (2.110)$$

where $B_z=B(T_z)$, $B_c=B(T_c)$, and $B_T=B(T_T)$. Following Yamamoto [1952], the transmission functions of a mixture of water vapor, carbon dioxide, and ozone may be approximated by the product of their respective transmission functions, *i.e.*,

$$\tau(u^*, \overline{T}) = \tau_{H_2O}(u_{H_2O}^*, \overline{T})\, \tau_{CO_2}(u_{CO_2}^*, \overline{T})\, \tau_{O_3}(u_{O_3}^*, \overline{T}) , \qquad (2.111)$$

and

$$\tilde{\tau}(u^*, \overline{T}_c) = \tilde{\tau}_{H_2O}(u_{H_2O}^*, \overline{T}_c)\, \tau_{CO_2}(u_{CO_2}^*, \overline{T}_c)\, \tau_{O_3}(u_{O_3}^*, \overline{T}_c) . \qquad (2.112)$$

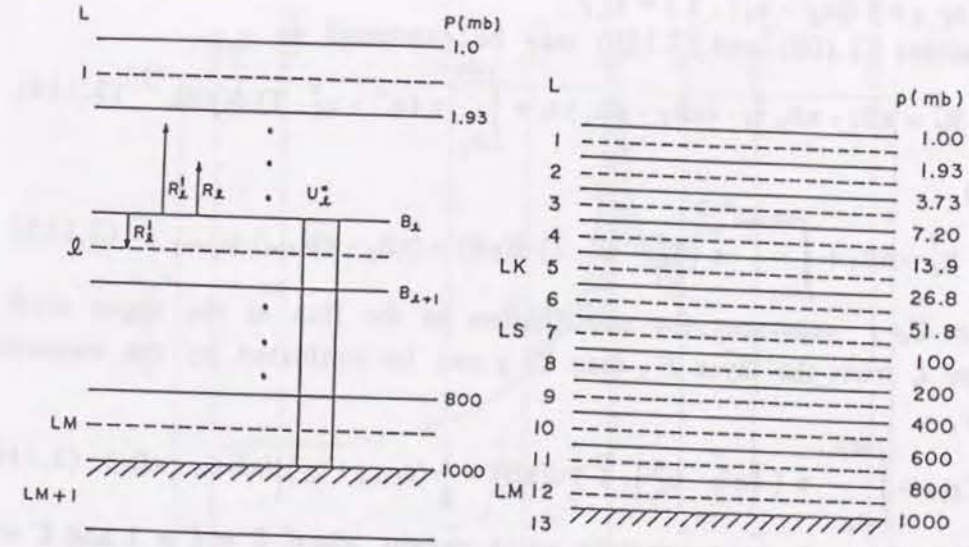

Figure 2.5: (a) Indexing scheme for the longwave radiation calculation. (b) Vertical discretization of the 12-layer model. LM is the index of the middle level of the lowest layer and LS is that of the lowest stratospheric layer. LK defines the level above which we use Dickinson [1973]'s longwave cooling parameterization. Currently we adopt the value LM=12, LS=7, and LK=5 for the 12-layer model.

2.3.2 Cloudless atmosphere

To calculate longwave fluxes numerically, we have to discretize equations (2.109) and (2.110). Vertical layers are denumerated by the index ℓ as shown in Figure 2.5. The effective absorber amount u^*_ℓ is defined between the earth's surface and the top level of layer ℓ, (see eq. (2.107)). The upward and the downward fluxes of longwave radiation, $R^{\uparrow}_z$, and $R^{\downarrow}_z$ are defined at the upper surface of layer ℓ. With the use of the notation,

$$\tilde{\tau}_\ell \equiv \tilde{\tau}\,(u^*_\infty - u^*_\ell\,,\ T_c\,),$$
$$\tau_\ell \equiv \tau\,(u^*_\infty - u^*_\ell\,,\ \overline{T}\,), \qquad (2.113)$$
$$\tau_{\ell',\ell} \equiv \tau\,(|u^*_{\ell'} - u^*_\ell|\,,\ \overline{T}\,) = \tau_{\ell,\ell'},$$

equations (2.109) and (2.110) may be expressed as

$$R^{\downarrow}_\ell = \pi B_\ell - \pi B_c\,\tilde{\tau}_\ell - (\pi B_T - \pi B_c)\,\tau_\ell + \int_{\pi B_\ell}^{\pi B_T} \tau\,(u^* - u^*_\ell\,,\ \overline{T})\,d(\pi B), \qquad (2.114)$$

and

$$R^{\uparrow}_\ell = \pi B_\ell + \int_{\pi B_\ell}^{\pi B_{LM+1}} \tau\,(u^*_\ell - u^*\,,\ \overline{T})\,d(\pi B) + (\pi B_g - \pi B_{LM+1})\,\tau_{\ell,\,LM+1}\ . \qquad (2.115)$$

Let $C_{\ell',\ell}$ represent the contribution to the flux at the upper level of layer ℓ from the layer ℓ', then $C_{\ell',\ell}$ can be evaluated by the trapezoidal low,

$$C_{\ell',\ell} = \int_{\pi B_{\ell'}}^{\pi B_{\ell'+1}} \tau\,(\,|u^* - u^*_\ell\,|,\ \overline{T}\,)\,d(\pi B) = \frac{1}{2}\,(\tau_{\ell'+1,\ell} - \tau_{\ell',\ell})(\pi B_{\ell'+1} - \pi B_{\ell'})\ . \qquad (2.116)$$

This form is approximately valid except when $\ell' = \ell + 1$ and $\ell' = \ell$. When the two layers are adjacent to each other, τ does not vary linearly with πB. Therefore, following Katayama [1972], two bulk transmission functions $\tilde{\tau}^{\pm}_\ell$ are defined as follows,

$$\tilde{\tau}^{-}_\ell \equiv (\pi B_\ell - \pi B_{\ell-1})^{-1}\,C_{\ell-1,\ell}\ , \qquad (2.117)$$
$$\tilde{\tau}^{+}_\ell \equiv (\pi B_{\ell+1} - \pi B_\ell)^{-1}\,C_{\ell,\ell}\ . \qquad (2.118)$$

Figure 2.6 shows a schematic representation of $\tau\,(\,|u^* - u^*_\ell\,|,\ \overline{T}\,)$ and $\tilde{\tau}^{\pm}_\ell$. Katayama defined these bulk transmission functions $\tilde{\tau}^{\pm}_\ell$ experimentally. Substituting (2.116), (2.117), and (2.118) into (2.114) and (2.115), we

obtain,

$$R^{\downarrow}_\ell = \pi B_\ell - (\pi B_\ell - \pi B_{\ell-1})\,\tilde{\tau}^{-}_\ell - \frac{1}{2}\sum_{\ell'=\ell-2}^{LK} (\tau_{\ell'+1,\ell} + \tau_{\ell',\ell})(\pi B_{\ell'+1} - \pi B_{\ell'})$$
$$- (\pi B_{LK} - \pi B_T)\,\tau_{LK,\ell} - (\pi B_T - \pi B_c)\,\tau_\ell - \pi B_c\,\tilde{\tau}_\ell \qquad (2.119)$$

and

$$R^{\uparrow}_\ell = \pi B_\ell + (\pi B_{\ell+1} - \pi B_\ell)\,\tilde{\tau}^{+}_\ell + \frac{1}{2}\sum_{\ell'=\ell+1}^{LK} (\tau_{\ell'+1,\ell} + \tau_{\ell',\ell})(\pi B_{\ell'+1} - \pi B_{\ell'})$$
$$+ (\pi B_g - \pi B_{LM+1})\,\tau_{\ell,\,LM+1}\ . \qquad (2.120)$$

Currently LK=5 and LM=12 in the twelve layer version of the model. Above the level LK, we use Dickinson[1973]'s parameterization of longwave radiative cooling described in section 2.3.5.

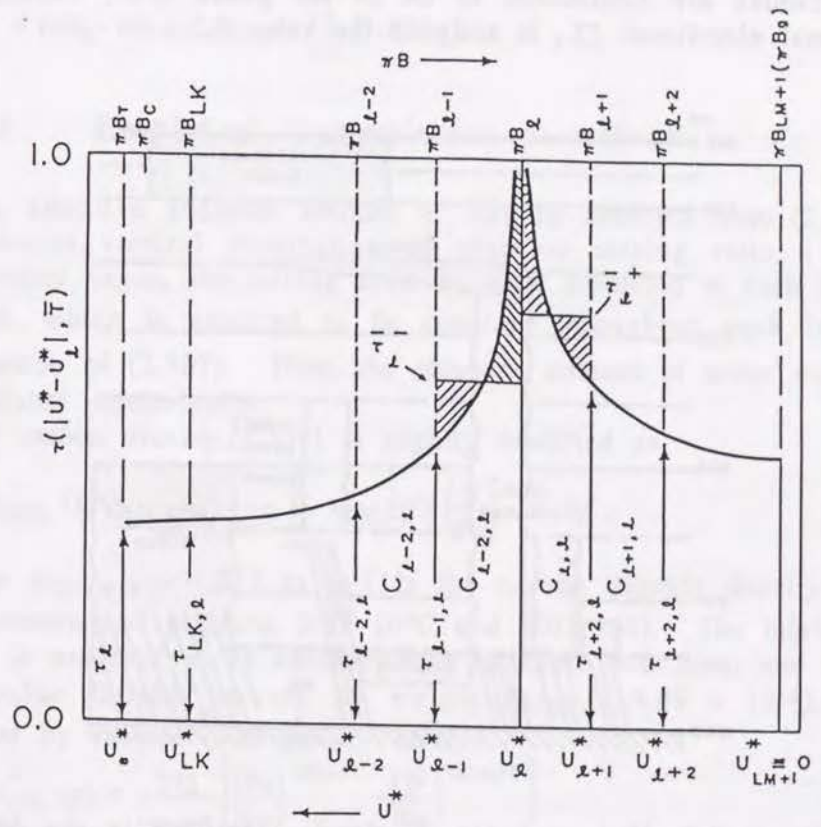

Figure 2.6: Schematic representation of the transmission functions $\tau\,(\,|u^* - u^*_\ell\,|,\ \overline{T}\,)$ and $\tilde{\tau}^{\pm}_\ell$ at layer ℓ.

2.3.3 Cloudy atmosphere

Five types of clouds are identified in the model currently. They are schematically shown in Fig. 2.7 and are classified as 1) clouds associated with large-scale condensation, 2) cirrus associated with subgrid-scale deep cumulus convection, 3) subgrid-scale penetrative cumulus convection, 4) clouds associated with middle level convection, and 5) stratus clouds associated with supersaturation within the planetary boundary layer. Currently only the first two types of clouds explicitly interact with radiative processes. Clouds are treated as black body radiators with a fractional cloudiness CL_ℓ equals to unity, except when the cloud layers are above 400 mb or colder than -40°C. In the latter case, clouds are considered to be in ice phase (*i.e.*, cirrus), and the fractional cloudiness CL_ℓ is assigned the value 0.5.

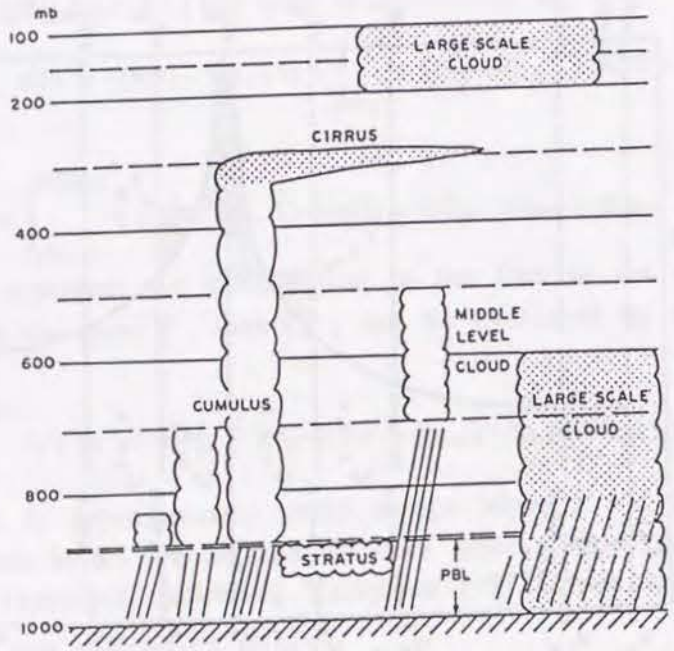

Figure 2.7: Various types of clouds identified in the MRI GCM-I. Radiatively interactive clouds are shaded.

Thus for a cloudy atmosphere (2.119) and (2.120) are modified to,

$$R_\ell^{\downarrow} = \pi B_\ell - (\pi B_\ell - \pi B_{\ell-1})\,\bar{\tau}_\ell^{\,\downarrow}\,(1-CL_{\ell-1})$$
$$-\frac{1}{2}\sum_{\ell'=\ell-2}^{LK}(\tau_{\ell'+1,\ell}+\tau_{\ell',\ell})(\pi B_{\ell'+1}-\pi B_{\ell'})\prod_{K=\ell-1}^{\ell'}(1-CL_K)$$
$$-[(\pi B_{LK}-\pi B_T)\,\tau_{LK,\ell}+(\pi B_T-\pi B_c)\,\tau_\ell+\pi B_c\,\bar{\tau}_\ell]\prod_{K=\ell-1}^{LK}(1-CL_K)\,, \qquad (2.121)$$

$$R_\ell^{\uparrow} = \pi B_\ell + (\pi B_{\ell+1}-\pi B_\ell)\,\bar{\tau}_\ell^{\,\uparrow}\,(1-CL_\ell)$$
$$+\frac{1}{2}\sum_{\ell'=\ell+1}^{LM}(\tau_{\ell'+1,\ell}+\tau_{\ell',\ell})(\pi B_{\ell'+1}-\pi B_{\ell'})\prod_{K=\ell}^{\ell'}(1-CL_K)$$
$$+(\pi B_g-\pi B_{LM+1})\,\tau_{\ell,LM+1}\prod_{K=\ell}^{LM}(1-CL_K)\,. \qquad (2.122)$$

2.3.4 Empirical transmission functions

The effective absorber amount u^* can be obtained from (2.107) if the continuous vertical distribution of absorber mixing ratio q is known. For water vapor, the mixing ratio q_{H_2O} is predicted at each level in the model, which is assumed to be constant throughout each layer in the evaluation of (2.107). Then, the effective amount of water vapor $u^*_{H_2O}$ is calculated numerically.

For carbon dioxide,(2.107) is slightly modified as,

$$u^*_{CO_2}(p) = \frac{1}{g\rho_{CO_2,NTP}}\int_p^{p_s} q_{CO_2}(p')\left(\frac{p'}{p_0}\right)^{\alpha_{CO_2}} dp'\,, \qquad (2.123)$$

where $\rho_{CO_2,NTP} = 1.977$ kg m^{-3} is the carbon dioxide density at normal temperature and pressure, NTP (0°C and 1013 mb). The mixing ratio of CO_2 is assumed to be constant both in space and time, and is assigned the value 0.0489 percent by weight ($q_{CO_2} = 4.89 \times 10^{-4}$), or 0.032 percent by volume (320 ppm). Thus,

$$u^*_{CO_2}(p) = \frac{252}{\alpha_{CO_2}+1}\left[\left(\frac{p_s}{p_0}\right)^{\alpha_{CO_2}+1}-\left(\frac{p}{p_0}\right)^{\alpha_{CO_2}+1}\right]. \qquad (2.124)$$

Following Manabe and Möller [1961], α_{CO_2} is taken as 0.86.

The ozone mixing ratio q_{O_3} is also predicted and the effective absorber amount of ozone is given by (2.123) by replacing $\rho_{CO_2,NTP}$ and $\alpha_{CO_2,NTP}$ with $\rho_{O_3,NTP} = 2.144$ kg m^3 and $\alpha_{CO_2,NTP} = 0.3$ respectively, after Manabe

and Möller [1961]. Thus,

$$u^*_{O_3,\ell}(p) = \frac{1}{g\rho_{O_3,NTP}} \sum_{\ell'=\ell}^{LM} q_{O_3,\ell} \int_{p_{\ell'}}^{p_{\ell'+1}} \left(\frac{p'}{p_0}\right)^{\alpha_{O_3}} dp' . \qquad (2.125)$$

Total transmission function of a mixture of gasses is given by (2.111) and (2.112). Yamamoto [1952] calculated τ and $\tilde{\tau}$ for water vapor from experimental laboratory data. Katayama [1972] obtained the empirical transmission functions for $\tau_{H_2O}(u^*_{H_2O}, \bar{T})$ by taking an average of τ given by Yamamoto for T = 220°K, 260°K, and 300°K, *i.e.*,

$$\tau_{H_2O}(u^*_{H_2O}, \bar{T}) = \begin{cases} 0.373 - 0.274Z + 0.035Z^2 & (u^* \geq 1) \\ 0.373 - 0.2595Z - 0.0275Z^2 & (1 > u^* \geq 10^{-4}) \\ F(298.7, 1.0) & (10^{-4} > u^*) \end{cases}, \qquad (2.126)$$

where $F(a, b) = 1/(1 + au^{*b})$ and $Z = \log_{10}u^*$. And for $\tilde{\tau}^*_{H_2O}(u^*_{H_2O}, T_c)$,

$$\tilde{\tau}^*_{H_2O}(u^*, 220°K) = \begin{cases} 0.254 - 0.1985Z + 0.0205Z^2 & (u^* \geq 0.1) \\ 0.216 - 0.2827Z - 0.0258Z^2 & (0.1 > u^* \geq 10^{-4}) \\ F(2.56, 0.39) & (10^{-4} > u^*) \end{cases} . \qquad (2.127)$$

Further, we adopt empirical transmission function equations derived by Schlesinger [1976] both for 15 μ band of carbon dioxide and for 9.6 μ band of ozone based on the experimental laboratory measurements by Elsasser [1960].

$$\tau_{CO_2}(u^*_{CO_2}, T) = 0.924 - 0.0390Z - 0.00466Z^2, \qquad (2.128)$$

$$\tau_{O_3}(u^*_{O_3}, T) = 0.919 - 0.0252Z - 0.000998Z^2, \qquad (2.129)$$

where Z equals to $\log_{10}u^*_{CO_2}$ for (2.128) and $\log_{10}u^*_{O_3}$ for (2.129). Values of $\tau_{CO_2}(u^*_{CO_2}, \bar{T})$ and $\tau_{O_3}(u^*_{O_3}, \bar{T})$ are defined as the arithmetic mean of τ_{CO_2} and τ_{O_3} over -80°C to 40°C.

2.3.5 Longwave radiative cooling in the upper stratosphere

Although Katayama's method of using mean transmission functions (2.105) and (2.106) is good in the troposphere and also in the lower stratosphere, it is less so in the upper stratosphere where anisotropy of radiative flux dominates. As a substitute of Katayama's method, we adopt Dickinson [1973]'s longwave radiative cooling parameterization in the upper stratosphere (*i.e.* the region above 13.9 mb in the current 12 layer version). That is,

$$\left(\frac{\partial T_\ell}{\partial t}\right)_{tr} = - C_{0,\ell} - a_{0,\ell}(T_\ell - T_{0,\ell})\beta_\ell, \qquad (2.130)$$

where

$$\beta_\ell = \begin{cases} 1, & \text{if } |T_\ell - T_{0,\ell}| \leq 5°K \\ 1 + \dfrac{0.0033(T_\ell - T_{0,\ell})}{T_{0,\ell} - 135}, & \text{if } |T_\ell - T_{0,\ell}| > 5°K \text{ and } T_\ell \geq 130°K \\ \dfrac{e^{-960/T_\ell} - e^{-960/T_{0,\ell}}}{960e^{-960/T_{0,\ell}}(T_\ell - T_{0,\ell})} T^2_{0,\ell}, & \text{if } |T_\ell - T_{0,\ell}| > 5°K \text{ and } T_\ell < 130°K \end{cases} \qquad (2.131)$$

$C_{0,\ell}$ is the cooling rate expected for the reference temperature profile $T_{0,\ell}$, and $a_{0,\ell}$ is a Newtonian cooling coefficient. As for the reference temperature $T_{0,\ell}$, the 1962 standard atmosphere profile is adopted. β_ℓ is a modification factor introduced by Dickinson and revised by Schlesinger [1976]. The values of $T_{0,\ell}$, $C_{0,\ell}$, and $a_{0,\ell}$ are presented in Tokioka *et al.* [1984, table 13.2].

2.3.6 Solar radiation

The extraterrestrial solar flux incident on a horizontal surface is given by,

$$S = \bar{S}_0 \left(\frac{\bar{\gamma}_E}{\gamma_E}\right)^2 \cos\zeta , \qquad (2.132)$$

$$\cos\zeta = \sin\phi \sin\delta + \cos\phi \cos\delta \cos h , \qquad (2.133)$$

where $\bar{S}_0$ (= 1345 watt m^{-2}) is the solar constant at one astronomical unit $\bar{\gamma}_E$, γ_E the earth-sun distance, ζ the solar zenith angle, ϕ the latitude, δ the solar declination and h is the hour angle of the sun. As shown in Tokioka *et al.* [1984, Appendix A13.1], δ and γ_E can be determined by a perturbation of Kepler's second low. The hour angle at each grid point is updated at every diabatic time step (one hour), and the solar declination and earth-sun distance are updated once a simulated day.

In the solar radiation parameterization developed by Katayama [1972]

and Schlesinger [1976], the solar flux under cloudless condition is depleted only by water vapor and ozone absorption and Rayleigh scattering. The effective absorption bands of water vapor for the solar spectrum exist in the wavelength range $\lambda > 0.9\mu$. As the amount of Rayleigh scattering varies as λ^{-4}, the scattering in that range can be neglected. As for ozone, the absorption bands exist in the wavelength $\lambda < 0.8\mu$. Since the amount of Rayleigh scattering increases exponentially with pressure, and because the heating by ozone absorption below 200 mb is negligible compared to the heating by water vapor absorption, we can neglect the effect of Rayleigh scattering on ozone absorption above 200 mb and also neglect the effect of ozone absorption on Rayleigh scattering below 200 mb.

Following Joseph [1966, 70] and based upon above considerations, the solar radiation is divided into two parts. One is "scattered part",

$$S_0^s = 0.634\ S_0 \cos\zeta\ , \qquad 0.9\mu > \lambda \qquad (2.134)$$

and the other "absorbed part",

$$S_0^a = 0.366\ S_0 \cos\zeta\ . \qquad \lambda > 0.9\mu \qquad (2.135)$$

Schlesinger [1976] calculated water vapor absorptivity A_{H_2O} from the data of McClatchey *et al.* [1972] and approximated the absorptivity piecewisely by quadratic polynomials;

$$A'_{H_2O}(X) = a_i + b_i X + c_i X^2\ , \qquad X_{i-1} \le X < X_i \qquad (2.136)$$

$$A_{H_2O}(X) = A'_{H_2O}(X)/0.366\ , \qquad (2.137)$$

$$X = u^* M\ , \qquad (2.138)$$

where the effective water vapor amount u^* is given by (2.107)

$$M = 35 \sec\zeta / \sqrt{1224 + \sec^2\zeta}\ , \qquad (2.139)$$

is the magnification factor to account of sphericity of the atmosphere after Rodgers [1967]. $A_{H_2O}(X)$ is the absorptivity for the "absorbed" part, and $A'_{H_2O}(X)$ is the absorptivity for the total solar spectrum. The coefficients a_i , b_i , and c_i are presented in Tokioka *et al.* [1984, Appendix A13.2].

By letting $y = A'_{H_2O}(X)$, the inverse function $X = A'^{-1}_{H_2O}(y)$ is fitted into quadratic polynomials;

$$X = A'^{-1}_{H_2O}(y) = d_i + e_i y + f_i y^2\ , \qquad y_{j-1} \le y < y_j \qquad (2.140)$$

The coefficients d_i , e_i , and f_i are also presented in Tokioka *et al.* [1984].

Absorptivity function of ozone for the total solar spectrum, $A_{O_3}(X)$ was calculated by Schlesinger [1976] in a similar way. In the calculation of solar radiation, the effective ozone amount $u^*_{O_3}$ is defined by, (*cf.* eq.(2.125))

$$u^*_{O_3} = \frac{1}{\rho_{O_3,NTP}} \int_0^z \rho_{O_3}(z)\, dz = \frac{1}{\rho_{O_3,NTP}} \int_0^p \rho_{O_3}(p')\, dp'\ , \qquad (2.141)$$

where ρ_{O_3} is the ozone density, q_{O_3} the ozone mixing ratio and $\rho_{O_3,NTP} = 2.144$ kg m^{-3} is the ozone density at NTP. In a discrete case, (2.141) can be written as,

$$u^*_{O_3,\ell} = u^*_{O_3,1} + \frac{1}{g\rho_{O_3,NTP}} \sum_{\ell'=1}^{\ell} q_{O_3,\ell'}(p_{\ell'+1} - p_{\ell'})\ , \quad \ell = 2, \ldots\ldots, LM+1 \qquad (2.142)$$

where $p_{\ell'}$ is the pressure at the upper surface of layer ℓ' , $q_{O_3,\ell'}$ the predicted ozone mixing ratio for layer ℓ' , and

$$u^*_{O_3,1} = \frac{1}{\rho_{O_3,NTP}} \int_{z_{0.5}}^{\infty} \rho_{O_3}(z)\, dz\ , \qquad (2.143)$$

is the effective ozone amount above the upper surface of layer 1 and $z_{0.5}$ is the height of the upper boundary. In calculating (2.143), we assume that the ozone number density $n_{O_3}(z)$ above the midlevel of the top layer decays exponentially with altitude following the mean ozone distribution by Krueger [1973]. Thus,

$$n_{O_3}(z) = n_{O_3}(z_1) \exp\left(\frac{z-z_1}{H}\right), \qquad z \ge z_1 \qquad (2.144)$$

where z_1 is the altitude of the midlevel of layer 1, and H = 4.35 km. Substituting (2.144) into (2.143) gives,

$$u^*_{O_3,1} = \frac{H \exp\left(-\frac{z_{0.5} - z_1}{H}\right) q_{O_3,1}\, p_{1.5}}{\rho_{O_3,NTP}\, R\, T_1}\ , \qquad (2.145)$$

where $p_{1.5}$ and T_1 are pressure and temperature at the midlevel of layer 1 respectively, and R is gas constant.

2.3.7 Cloudless atmosphere

The 'absorbed" part of the solar radiation S_0^a is absorbed only by the water vapor in the troposphere and at the earth's surface. The other absorption can be neglected. This means that the absorption by the water vapor in the stratosphere can be neglected in comparison to the "scattered" part absorption by ozone.

After neglecting the absorption by water vapor on the radiation

reflected by the earth's surface, the net downward flux of the "absorbed" part at the upper surface of layer ℓ, $S_{a,\ell}$, is

$$S_{a,\ell} = S_0^a , \qquad \ell = 1, 2,....., LS \tag{2.146}$$

$$S_{a,\ell} = S_0^a \left\{1 - A_{H_2O} [(u^*_{H_2O,\infty} - u^*_{H_2O,\ell}) M]\right\} , \quad \ell = LS+1,....., LM+1 \tag{2.147}$$

where A_{H_2O} is given by (2.137) and M is the magnification factor defined by (2.139). The absorption of solar radiation by water vapor in layer ℓ, $AS_{a,\ell}$, is therefore

$$AS_{a,\ell} = 0.0 , \qquad \ell = 1, 2,....., LS \tag{2.148}$$

$$AS_{a,\ell} = S_{a,\ell} - S_{a,\ell+1} \qquad \ell = LS+1,....., LM+1 \tag{2.149}$$

The absorption of the solar radiation absorbed at the earth's surface is,

$$AS_{a,LM+1} = (1 - \alpha_s) S_{a,LM+1} , \tag{2.150}$$

where α_s is the albedo of the surface. Originally, α_s is given as 0.14 for bare land, 0.07 for open ocean, 0.3 for frozen land, 0.4 for bare sea ice, 0.7 for snow-covered sea ice, 0.5 for melting snow and *min* (0.85, 0.7 + 0.15 x Z) for snow or ice, where Z is a height in km. Yamazaki [1989] found some improvements in model climate by using climatological data of surface albedo and ground wetness.

By neglecting the effect of Rayleigh scattering on ozone absorption above 200 mb, the downward flux and its absorption of the scattered part are,

$$S^{\downarrow}_{s,\ell} = S^s_0 \left\{1 - A_{O_3} (u^*_{O_3,\ell} M)\right\} , \qquad \ell = 1, 2,....., LS+2 \tag{2.151}$$

$$AS^{\downarrow}_{s,\ell} = S^{\downarrow}_{s,\ell} - S^{\downarrow}_{s,\ell+1} , \qquad \ell = 1, 2,....., LS+1 \tag{2.152}$$

$$AS^{\downarrow}_{s,\ell} = 0.0 , \qquad \ell = LS+2,....., LM \tag{2.153}$$

where the effective ozone $u^*_{O_3,\ell}$ is given by (2.142). By neglecting the effect of ozone absorption on Rayleigh scattering below 200 mb, the downward flux of the "scattered" part at the earth's surface $S^{\downarrow}_{s,LM+1}$ is,

$$S^{\downarrow}_{s,LM+1} = S^{\downarrow}_{s,LS+2} (1 - \alpha_0)/(1 - \alpha_0\alpha_s) , \tag{2.154}$$

where

$$\alpha_0 = 0.085 - 0.247 \log_{10} (\frac{p_s}{1000} \cos\zeta) , \tag{2.155}$$

is the albedo due to Rayleigh scattering (Coulson,1959) and p_s the surface pressure.

The "scattered" part of the solar radiation that is absorbed at the earth's surface is,

$$AS^{\downarrow}_{s,LM+1} = (1 - \alpha_s) S^{\downarrow}_{s,LM+1} , \tag{2.156}$$

The upward flux of the "scattered" part at LS+2, $S^{\uparrow}_{s,LS+2}$, is then

$$S^{\uparrow}_{s,LS+2} = S^{\downarrow}_{s,LS+2} - AS^{\downarrow}_{s,LM+1}$$

$$= S^{\downarrow}_{s,LS+2} \{1 - (1 - \alpha_s)(1 - \alpha_0)/(1 - \alpha_0\alpha_s)\} . \tag{2.157}$$

By neglecting the effect of Rayleigh scattering on ozone absorption above 200 mb, the absorption of upward flux of the "scattered" part in layer ℓ, $AS^{\uparrow}_{s,\ell}$, is

$$AS^{\uparrow}_{s,\ell} = S^{\uparrow}_{s,LS+2} \{A_{O_3} [u^*_{O_3,LS+2} M + 1.9 (u^*_{O_3,LS+2} - u^*_{O_3,\ell})]$$

$$- A_{O_3} [u^*_{O_3,LS+2} M + 1.9 (u^*_{O_3,LS+2} - u^*_{O_3,\ell+})]\} , \quad \ell = 1,....., LS+1 \tag{2.158}$$

$$AS^{\uparrow}_{s,\ell} = 0.0 , \qquad \ell = LS+2,....., LM \tag{2.159}$$

where the factor 1.9 is an average magnification factor for the diffuse upward radiation by Lacis and Hansen [1974].

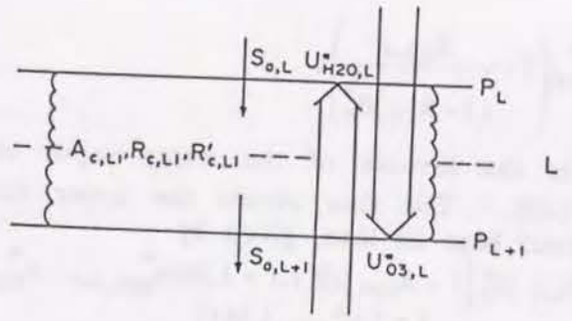

Figure 2.8: Schematic representation of a single cloud layer. Note that the effective amount of ozone $u^*_{O_3}$ for the solar radiation is defined between the bottom level of layer ℓ and top of the atmosphere, which differs from that of water vapor $u^*_{H_2O}$.

2.3.8 Cloudy atmosphere

Consider a single cloud located in layer L as shown in Fig.2.8. The flux of the "absorbed" part at the upper surface of layer $\ell \le L$, $S_{a,\ell}$, is given by (2.151) as,

$$S_{a,\ell} = S_0^a \left\{ 1 - A_{H_2O} \left[(u^*_{H_2O,\infty} - u^*_{H_2O,\ell}) M \right] \right\}. \quad \ell = LS+1, \ldots, L \qquad (2.160)$$

Letting A_{CL} and R_{CL} denote the absorptivity per unit pressure thickness and the reflectivity of cloud layer L, the flux of the "absorbed" part at the upper surface of layer L+1, $S_{a,L+1}$, is given by

$$S_{a,L+1} = [1 - R_{CL} - A_{CL}(p_{L+1} - p_L)] S_{a,L}, \qquad (2.161)$$

where the quantity in brackets represents the transmissivity of cloud layer L. In order to calculate the fluxes in the cloudless atmosphere beneath the cloud by (2.147), the total optical thickness from the top of the atmosphere to the upper surface of the layer under consideration is required. Katayama [1972] defined the equivalent total optical thickness of water vapor from the top of the atmosphere to the base of the cloud layer L, $\mathscr{L}_{L+1}$, by

$$(1 - R_{CL}) S_0^a \{ 1 - A_{H_2O}(\mathscr{L}_{L+1}) \} = S_{a,L+1}, \qquad (2.162)$$

hence

$$\mathscr{L}_{L+1} = A^{-1}_{H_2O} \left(1 - \frac{S_{a,L+1}}{(1 - R_{CL}) S_0^a} \right), \qquad (2.163)$$

where $A^{-1}_{H_2O}$ is the inverse of the water vapor absorptivity function given by (2.140). The flux across the upper surface of any layer beneath the cloud base is, then, given by

$$S_{a,\ell} = (1 - R_{C,L}) S_0^a \left\{ 1 - A_{H_2O} \left[\mathscr{L}_{L+1} + 1.66 (u^*_{H_2O,L+1} - u^*_{H_2O,\ell}) \right] \right\}, \quad \ell = L+2, \ldots, LM+1 \qquad (2.164)$$

where 1.66 is the diffusivity factor for diffuse radiation beneath the cloud. The absorption of solar radiation is

$$AS_{a,\ell} = \begin{cases} S_{a,\ell} - S_{a,\ell+1}, & \ell = LS+1, \ldots, LM \quad \text{but } \ell \neq L \\ (1 - R_{CL}) S_{a,L} - S_{a,L+1}, & \ell = L \end{cases} \qquad (2.165)$$

where R_{CL} is the reflectivity of cloud layer L for the "absorbed" part, and $S_{a,L}$, the solar radiation reflected from the cloud layer. The absorption of radiation reflected from the cloud layer is neglected. The "absorbed" part of the solar radiation that is absorbed at the earth's surface is given by (2.150).

In the case of "scattered" part of the solar radiation, equations (2.151), (2.152), (2.153), (2.156), (2.158), and (2.159) are unchanged. In equations (2.154) and (2.157), α_0 is replaced by α_c, the albedo of the cloudy atmosphere for the "scattered" part,

$$\alpha_c = 1 - (1 - R'_{CL})(1 - \alpha_0) \qquad (2.166)$$

where R'_{CL} is the reflectivity of cloud layer L for the "scattered" part. The values of R_{CL}, R'_{CL}, A_{CL}, and A'_{CL} are presented in Tokioka *et al.* [1984], which are assumed to be characterized by the respective properties of low, middle, or high clouds.

In the case of two or more contiguous cloud layers, each cloud layer within contiguous cloud layers is treated as a separate cloud for the solar radiation calculation like one of multiple clouds. As a result, the heating rate due to absorption of solar radiation at layer ℓ is given by,

$$\left(\frac{\partial T_\ell}{\partial t} \right)_{sr,\ell} = \frac{g(AS_{a,\ell} + AS^{\downarrow}_{s,\ell} + AS^{\uparrow}_{s,\ell})}{C_p (p_{\ell+1} - p_\ell)}, \qquad (2.167)$$

where p_ℓ is the pressure at the upper surface of layer ℓ.

Chapter 3

Numerical simulation

Motions of the atmosphere are governed by physical laws which can be solved numerically as an initial value problem by using electronic computers. The system of governing equations is called a *mathematical model* and when numerical approximations are applied to the system, it is termed a *numerical model.* A general circulation model (GCM) is one of the largest numerical models, which has been developed to simulate earth's atmosphere. Recent progress of climate simulations as well as numerical weather predictions have been made largely by the development of so called supercomputers. This chapter describes the supercomputer system and the simulated results of the Meteorological Research Institute general circulation model.

3.1 The super computer system

3.1.1 Hardware

There is no rigorous definition of a supercomputer, but one current notion is that a supercomputer is the biggest, fastest computer available at the moment. Conversely a conventional computer is a classical "Von Neuman" machines: sequential, scalar processors that can operate on a single pair of operands at a time, which originated from the work of Von Neuman in the mid-1940's. Some supercomputers accomplish many simultaneous operations by "vector" processing, that is, by using powerful instructions to feed arrays of operands through a "pipeline" or assembly line of operations.

The "vector" means an ordered list of items in a computer's memory, contained within a FORTRAN array. A simple vector is defined as having a starting address, a length, and a stride. Consider:

```
      DO 500 I = 1, N
         J = J * J / I
         K = K + 2
         A(I) = B(IB(I)) * C(K) + D(J)
500   CONTINUE
```


All of the vectors above have length N; A and C are simple vectors with strides of one and two, respectively; B and D are indirect address vectors.

The "pipeline" denotes a mechanism inside all supercomputers that allow new operands to begin processing in each clock cycle and moves partially completed operations along an assembly line inside the CPU (central processing unit), generally producing one result per clock cycle at the end of each pipeline. This pipeline concept is a streamlining of the conventional scalar processor, a recognition that the most intense use of a computer is almost always in a loop, doing the same operations to many different operands.

The computer system installed in the Meteorological Research Institute is a loosely coupled multi processor of two computers: HITAC M-280D as a global processor and S-810/10 a local processor. M-280D is a large general purpose computer with 16 MB (Megabyte = 10^6 byte) main memory. S-810/10 is a super computer with 32 MB main memory with a high speed array processor, which enables vector operation at high speed. The nominal maximum operation capacity is 315 MFLOPS (million floating-point operations per second).

The S-810/10 has several characteristics to realize high performances [Kodaka *et al.*, 1986]:

(a) Parallel pipeline processing, that is processing to make as many pipelined arithmetic units as possible operate in parallel.

(b) A high level of vectorization for programs through extended vector instructions. (Vectorization is the process whereby a compiler generates vector instructions for a loop. Also the process whereby a programmer restructures a program to cause the compiler to vectorize the important loops.)

(c) High speed scalar processing.

(d) Using extended storage.

Among them, the vector processing applicability is quite important for users to achieve optimal performance on a supercomputer. For example, let us see a simple example by Levesque and Williamson [1989]. we usually transform the matrix (or two dimensional vector in this case) algebra statement:

```
   A=B+C
```

into

```
            DO 1000 J = 1, NDIM2
               DO 1000 I = 1, NDIM1
                  A(I,J) = B(I,J) + C(I,J)
1000        CONTINUE
```

Most of us learned to work within the constraints of FORTRAN, and many know that it is more efficient on a conventional computer to write the matrix sum as above, rather than with the J and I loops reversed:

```
      DO 1010 I = 1, NDIM1
          DO 1010 J = 1, NDIM2
              A(I,J) = B(I,J) + C(I,J)
1010  CONTINUE
```

The efficiency maybe less than a factor two on conventional computers. However — on a supercomputer, depending on the dimensions of the arrays — loop 1000 may execute an order of magnitude than loop 1010. Therefore supercomputer users are required to program effectively especially relating to vectorization.

Generally scientific calculation program processing can be separated into three parts. The first is repeated operations that can be processed in the vector processing mode, vectorizable parts. The second is also repeated operations but not vectorizable, and the last is non-repeated operations. If we define T as the time in which a certain program is executed by the scalar processor, and T_v the time in which the vectorizable parts are executed, then the vectorization ratio can be defined as T_v/T. When the program is executed by the vector processor, the vectorized part is executed approximately several to one hundred times faster by vector processing than by scalar processing. As a result one of the most important approaches to increase the performance of the vector processor is to extend the vector processing applicability, that means increasing vectorization ratio T_v/T. Usually the analysis of large-scale scientific and technical calculation programs shows that it remains in only 55% of vectorization ratio to vectorize the four rules of arithmetic or macro-arithmetic such as inner product and vector sum. In order to increase vectorization ratio to more than 80%, it is necessary to vectorize conditional arithmetic (DO loops including IF statements), integer arithmetic, indirect indexed vector (list vector) arithmetic, *etc.* Table 3.1 shows the vectorizability of the S-810, which includes not only conventional vector operation but also first-order iteration operation, list vector operation for sparse matrix calculation, conditional operation, expand or compress operation and function (sin, exp) operation.

Table 3.1 S-810 Vectorizability from Kodaka *et al.*, [1986].

Operation Type	Example of Operation	Vectorizable
Arithmetic	$A_i = B_i * C_i + D_i$	YES
Sum / Inner Product	$S = S + A_i * B_i$	YES
First Order Iteration	$A_i = A_{i-1} * B_i + C_i$	YES
Integer / Logical	$N_i = L_i * M_i$	YES
Convert	$A_i = FLOAT(N_i)$	YES
List Vector	$A_{ji} = B_{ji} * C_{ki}$	YES
Conditional Arithmetic	IF $A_i < B_i$ THEN $C_i = D_i$ ELSE $C_i = E_i$	YES
Expand / Compress	WHERE $(A_i > B_i)$ PCACK $(C_i = D_i)$	YES
Search	$S = MAX(A_i)$	YES
Function	$A_i = SIN(B_i)$	YES
Unsuitable Data Reference	$A_i = B_{i-k} + B_i$	NO

3.1.2 Software

Software system is quite important to draw out the performance of hardware completely and use the machine effectively. The control program for the S-810 system is VOS3/HAP (Virtual Operating System 3/ High-speed Array Processor), which is the general purpose operating system. We use FORTRAN 77 programs written with standard language specification. Then, the FORT77HAP (a vectorizing compiler) compiles programs into vector instruction chains automatically. A compiler is a computer program that reads our program source code as data and translates it into machine code that can be read and interpreted as instructions and data understandable at the computer's hardware level. The compiler is useful for debugging, since diagnostic messages can point to the source statement and possibly even the instruction within it that caused a problem. However, the FORTRAN program of the general circulation model is so complex that we have to rewrite it to increase the vector processing performance. For this purpose, we use the Vectizer, a kind of analyzer for vectorization, which analyzes a FORTRAN

program and outputs the information to vectorize more DO loops than those in the original coding.

Figure 3.1 is the module structure list of the MRI GCM, which shows the model code flow through all control and computational levels of the program, where

MAIN	main program;
CNSTNT	defining constant parameters;
INPUT	preparing initial data;
HYDRST	calculation of hydrostatic equation;
SDET	calculation of earth-sun distance and solar zenith angle;
GMP	checking total air mass decrease which relates to roundoff error of the computer;
C3STEP	controlling physical process computation;
COMP3	computing physical process;
PBLCOE	computing coefficients that are used to interpolate variables in the PBL (Planetary Boundary Layer);
DRYCON	computing process of dry convection;
PROFIL	vertical interpolation of variables;
MLCONV	computing process of middle level convection;
LSPRCP	computing process of large scale precipitation;
STRTUS	computing process of stratus cloud;
PBLWIND	calculation of PBL wind;
CUP	computing process of penetrative cumulus convection;
UH2O	computing effective amount of water vapor;
SHRTW	shortwave radiation calculation;
OZONSS	computing the photochemical process of ozone;
LONGW	longwave radiation calculation;
PBL	computing process of PBL;
GROUND	computing ground process;
CUMFRC	cumulus friction calculation;
PBLFRC	PBL friction calculation;
GDRAG	computing gravity wave drag due to topography;
VADSH	calculation of vertical transport of water vapor;
VADO3	calculation of vertical transport of ozone;
DIFFH	calculation of horizontal diffusion of momentum;
C1STEP	controlling advective process calculation;
COMP1	advective process calculation;
OUTAPE	data output.

Program modules are called in order from top to bottom from higher-level routine. After some modification for vectorizing to the original program, it takes 34.61 seconds for a "one-hour simulation" with the current version of the MRI GCM. If we do all the calculation with the scalar processor, it takes 60.37 seconds. Note that "one-hour simulation"

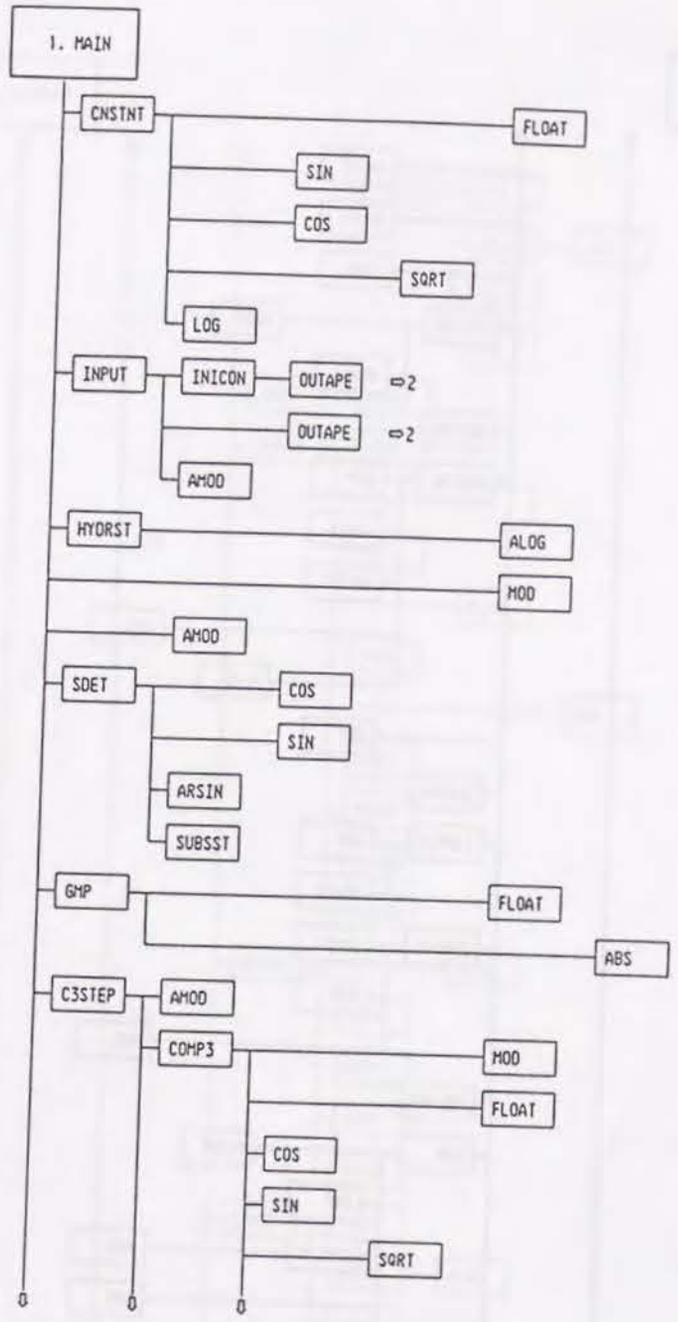

Figure 3.1: The module structure list of the MRI GCM.

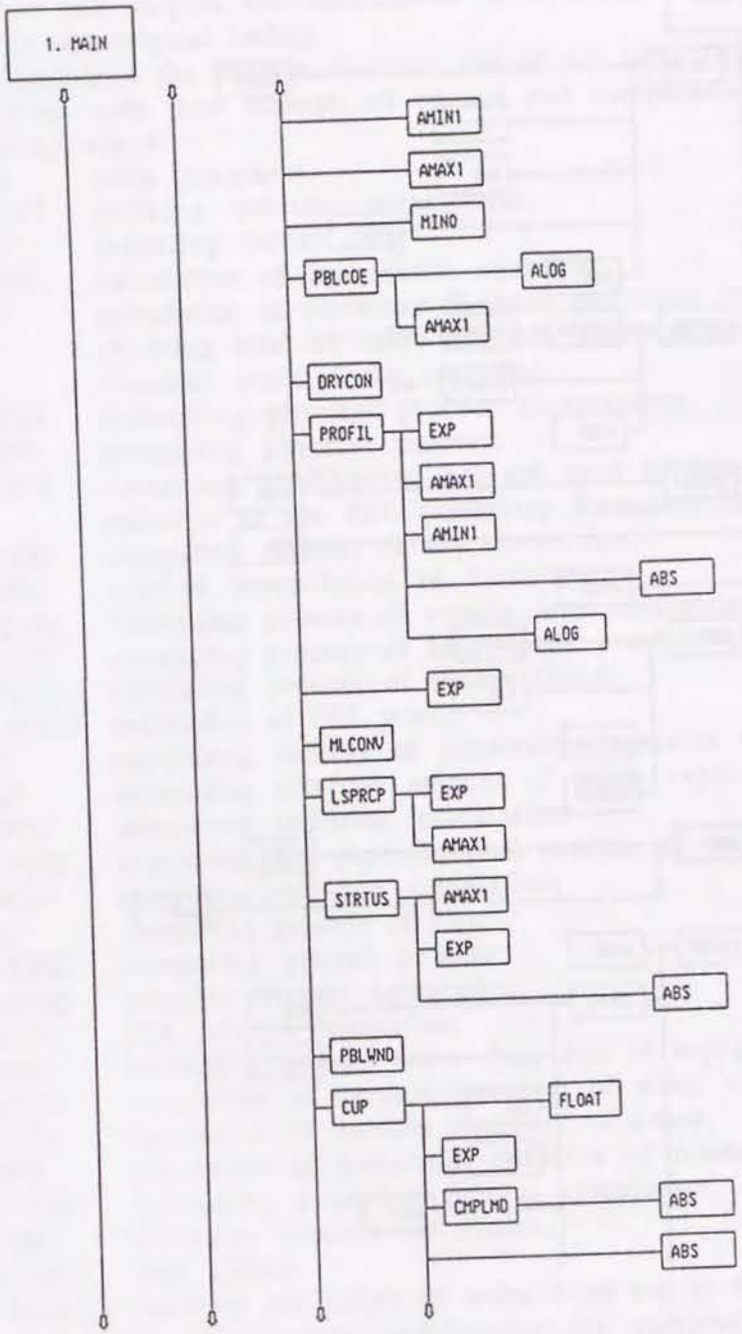

Figure 3.1 (cont.)

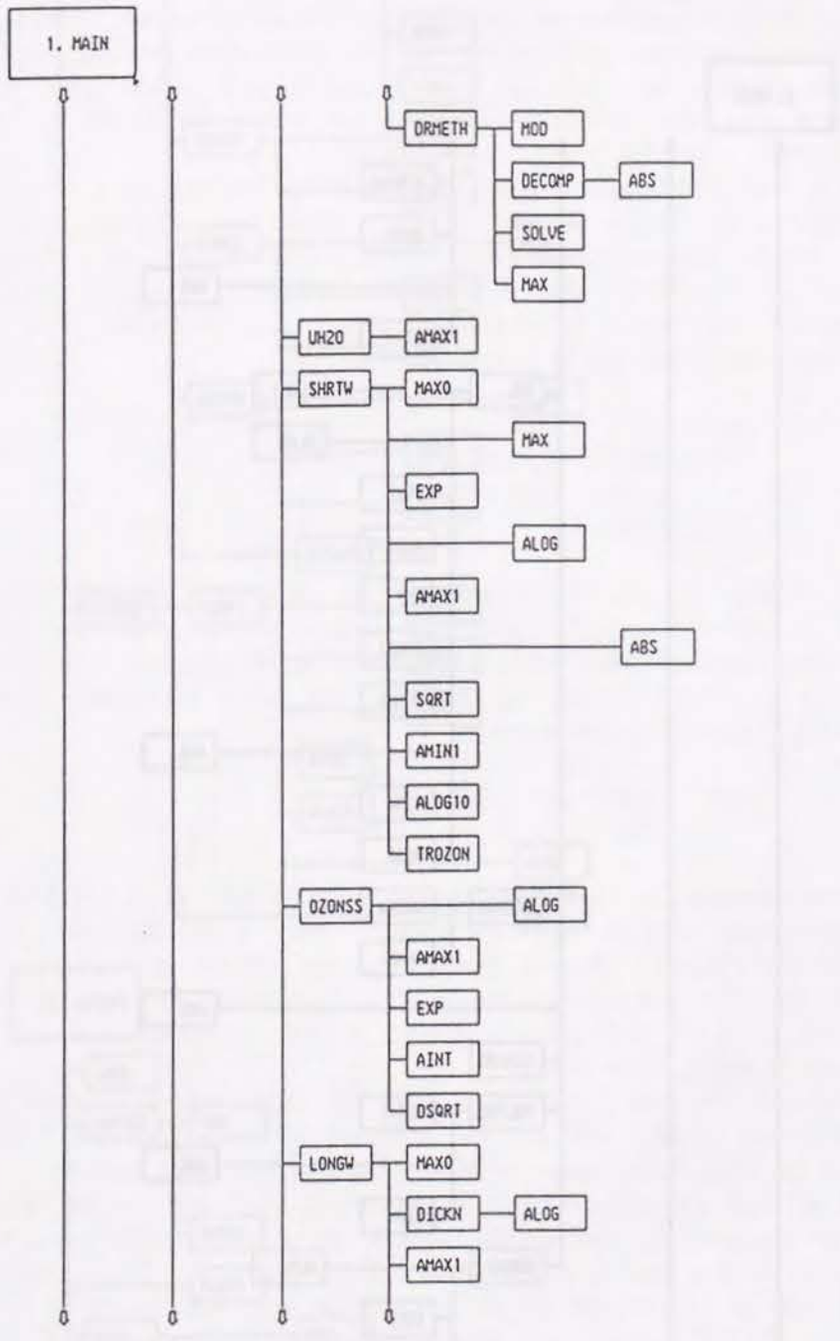

Figure 3.1 (cont.)

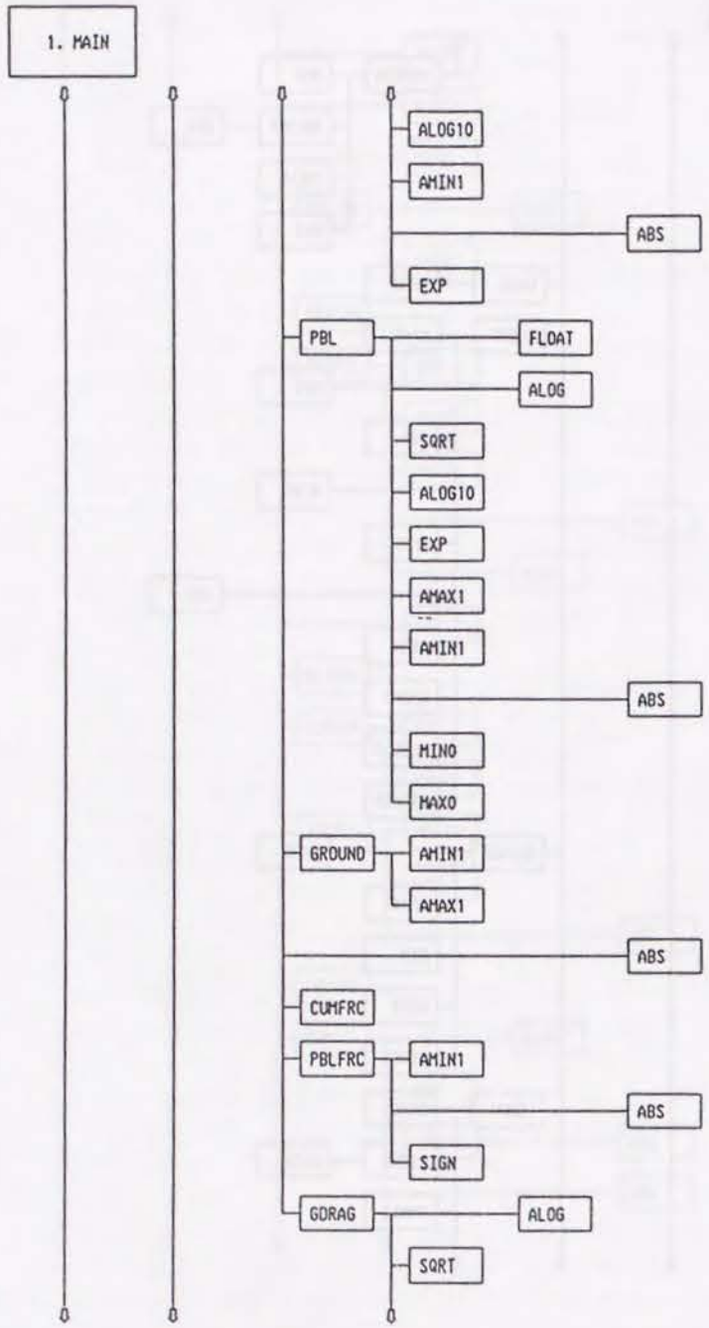

Figure 3.1 (cont.)

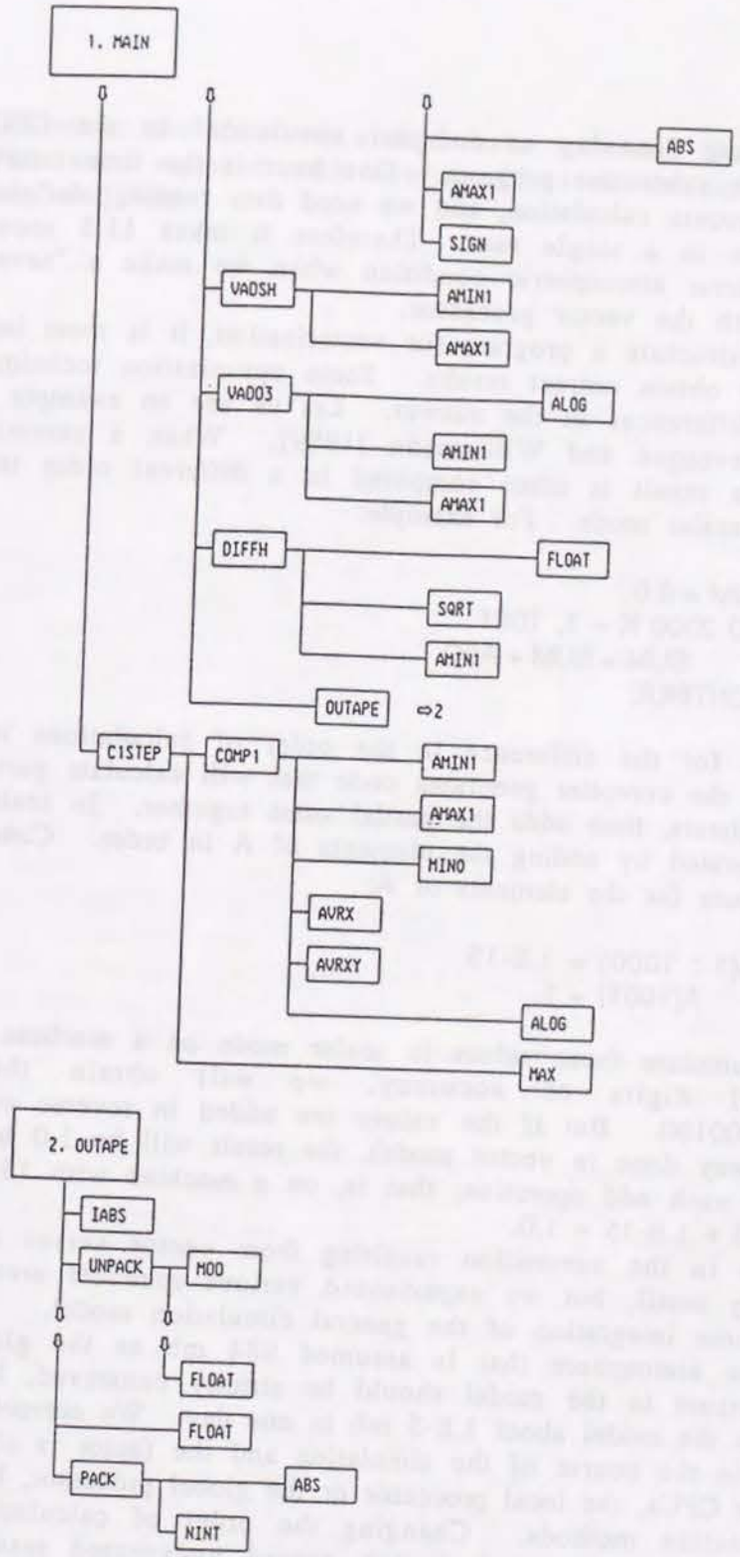

Figure 3.1 (cont.)

is different from "one-day or one-year simulation" in the CPU time portion of each subroutine program. One hour is the time interval for the physical process calculation, and we need data reading, defining, and writing process in a single run. Therefore it takes 11.5 seconds to simulate one hour atmospheric condition when we make a "several-day simulation" with the vector processor.

When we restructure a program for vectorization, it is most important to continue to obtain correct results. Some optimization techniques can cause slight differences in the answer. Let us see an example of this following Levesque and Williamson [1989]. When a summation is vectorized, the result is often computed in a different order than that performed in scalar mode. For example:

```
      SUM = 0.0
      DO 2000 K = 1, 1001
           SUM = SUM + A(K)
2000  CONTINUE
```

The reason for the difference in the order of calculations in vector mode is that the compiler generates code that will calculate partial sums in vector registers, then adds the partial sums together. In scalar mode, SUM is generated by adding the elements of A in order. Consider the following values for the elements of A:

```
A(1 : 1000) = 1.E-15
   A(1001) = 1.
```

If we accumulate these values in scalar mode on a machine that has 15 decimal digits of accuracy, we will obtain the result 1.00000000000100. But if the values are added in reverse order (this is not the way done in vector mode), the result will be 1.0 because of roundoff on each add operation; that is, on a machine with 15 digits of accuracy, 1.0 + 1.E-15 = 1.0.

Difference in the summation resulting from vector versus scalar are usually very small, but we experienced various roundoff errors in the course of time integration of the general circulation model. The total mass of the atmosphere that is assumed 984 mb as the global mean surface pressure in the model should be strictly conserved, however it decreases in the model about 1.E-5 mb in one day. We correct the value every day in the course of the simulation and the factor is changed not only by the CPUs, the local processor or the global processor, but also by the optimization methods. Changing the order of calculation in the complex DO loops for optimization caused unexpected results in the

calculation; therefore we should have to check the results whenever CPUs were replaced with new machines or the optimization methods were modified.

3.2 Model's January simulation

3.2.1 Introduction

In this section the model performance of the 12-layer version of the Meteorological Research Institute general circulation model (MRI GCM) are discussed. The preliminary results on the winter simulation is discussed in Tokioka and Yagai [1984], however this version of the model has serious westerly biases; the westerly jet in the stratosphere is too strong and the Aleutian low in the troposphere is too deep. Recently by incorporating orographic gravity wave drag parameterization, the above deficiency of the model is much improved (Yagai and Yamazaki, 1988), thus the improved results of the MRI GCM are presented below.

The orographic gravity wave drag parameterization is based on Palmer *et al.* [1986]; it is based on '"saturation" hypothesis by Lindzen [1981] and recent observations find gravity wave saturation not only in the mesosphere but also in the lower stratosphere and troposphere [Fritts *et al.*, 1988, Tsuda *et al.*, 1989]. Palmer *et al.* found westerly biases in the U. K. Met. Office model and proposed an orographically excited Internal Gravity Wave (IGW) drag parameterization to alleviate these biases. McFarlane [1987] also introduced a similar parameterization in the Canadian Climate Centre general circulation model and improved the systematic errors. Following to their methods, the surface drag due to the topography is expressed as,

$$\tau_s = \kappa \rho N u \cdot VAR \qquad (3.1)$$

where ρ is air density, N the Brunt-Väisälä frequency, and u is the lowest level wind vector. VAR is the variance of the subgrid scale orography calculated in the 4°x5° region by using 0.2°x0.25° data of topography. Figure 3.2 shows the standard deviation of topography, $\sqrt{VAR}$, used in this experiment. There are large value of VAR over high mountain ranges, such as the Tibetan Plateau and Rockies, and over relatively low mountains, such as the Anatolian Plateau (Turkey), the Iranian Plateau, and the Alps. The constant κ is a tunable parameter of which Palmer *et al.* [1986] adopted 2.5×10^{-5} m^{-1} and McFarlane [1987] adopted 0.8×10^{-5} m^{-1}; the choice of value is closely related to the vertical and horizontal resolution of the model since the magnitude of the wind **u** depends on the height of the lowest level, while the variance

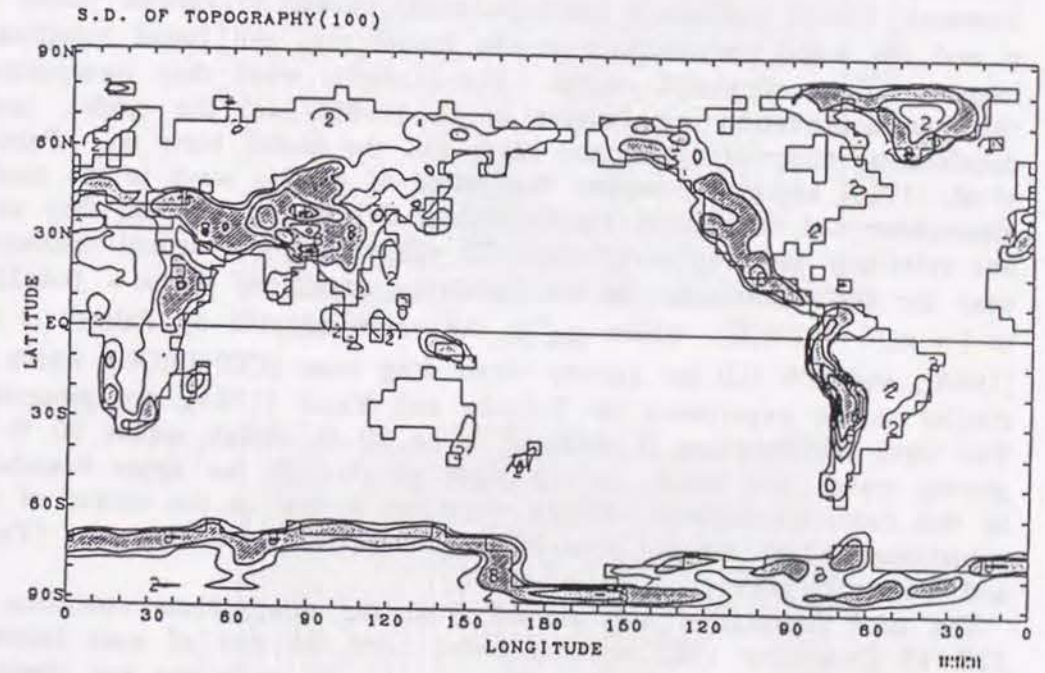

Figure 3.2: The standard deviation of topography normalized by 100 m and calculated in the 4°x5° region by using 0.2°x0.25° data set of topography. Contour intervals are 2, 4, 8, 12, and 16.

of topography VAR relates to the size of the grid.

It is known that gravity waves can propagate upward to the upper stratosphere and mesosphere, but it is not sure what part of gravity waves that reach the top layer escape through the upper boundary of the model. The situation is same to the model of which upper boundary is set to 0.0 mb in the pressure coordinate, since the effective upper boundary depends on its resolution near the top boundary. Yagai and Yamazaki [1988] performed six experiments related to various values of κ and the wave transmittance at the model top, and found significant impacts on the simulated results. For example, when they incorporated the parameterization by Palmer *et al.* [1986] into the model, large deceleration occurred at the top layer and the model blew up. Palmer *et al.* [1986] assumed complete dissipation of gravity wave in the model atmosphere and the British Meteorological Office model which they used has relatively low top level about 20 mb with high vertical resolution near the earth's surface. In the following, results of the $\kappa = 0.4 \times 10^{-5}$ $m^{-1} \approx \kappa_0/6$ (IGW/6), where κ_0 is the value adopted by Palmer *et al.* [1986], and $\kappa = 0.0$ no gravity wave drag case (CONTROL) which is similar to the experiment by Tokioka and Yagai [1984], are presented. The wave transmittance is assumed to be 90 %, which means 90 % of gravity waves that reach the top layer go through the upper boundary. In this case, stratospheric sudden warmings appear in the course of the experiment, which are not seen in the no gravity wave drag case (Yagai and Yamazaki [1991]).

The time integration was started from the atmospheric condition at 12Z 15 December 1982 and integrated until the end of next January. The sea surface temperature used in the experiment is the one observed during the corresponding winter(1982/83). The analyses were made for the last 31 days (January) of the experiment.

3.2.2 Zonal mean state

Zonal mean westerly wind and temperature cross-sections for January for CONTROL and IGW/6 together with the observation for January 1983 are shown in Figures 3.3 and 3.4, respectively. The observation is based on the U.S.A.NMC (National Meteorological Center) data and the wind above 50 mb is the "balance wind" (Randel,1987) obtained from the geopotential fields. In CONTROL, large systematic errors are seen in the upper troposphere and stratosphere in the northern hemisphere. The polar night jet is too strong and the maximum value reaches 120 ms^{-1} at the top level around 55°N. Being consistent with this, the polar night region stratospheric temperature in CONTROL is much colder than

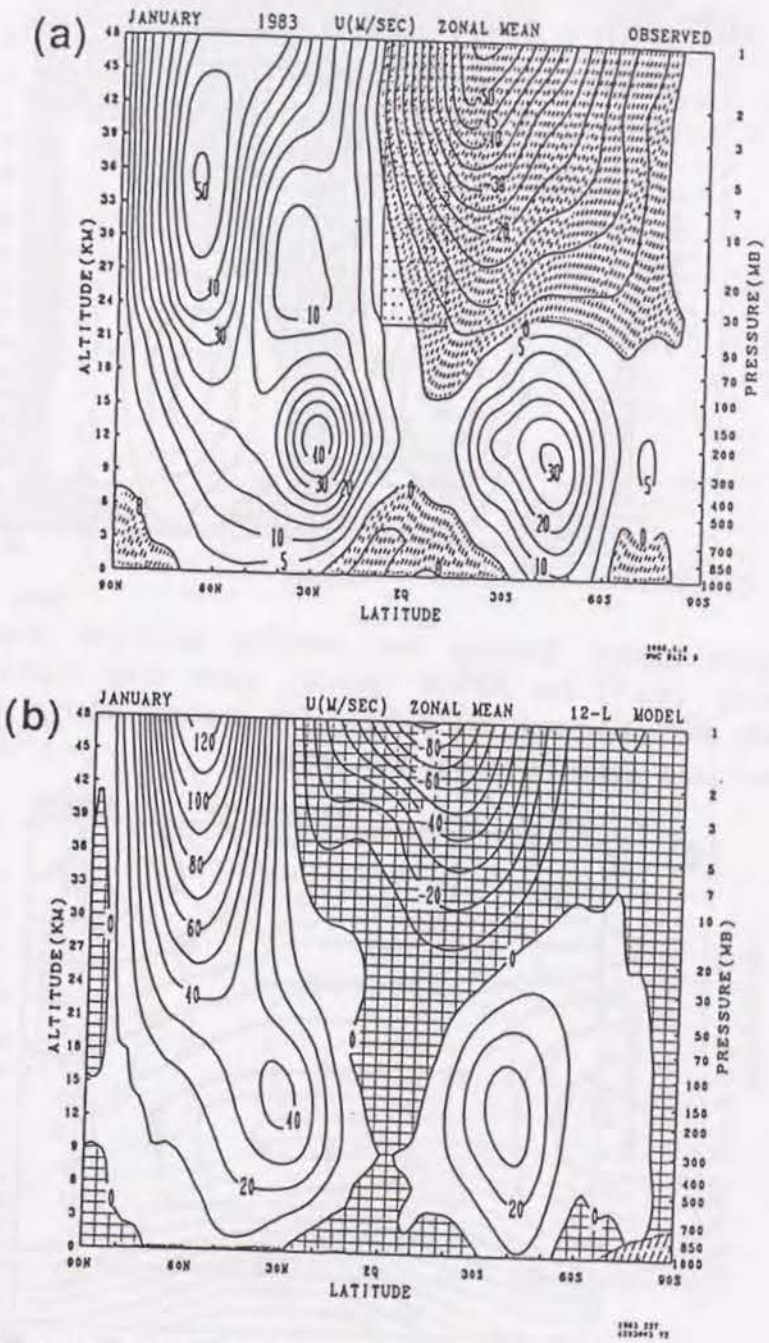

Figure 3.3: Zonally and monthly averaged westerly winds (ms^{-1}) for (a) January analysis for the year 1983 and (b) the CONTROL simulation. The contour interval is 5 ms^{-1} in the observation and 10 ms^{-1} in the simulation. Negative values are shaded.

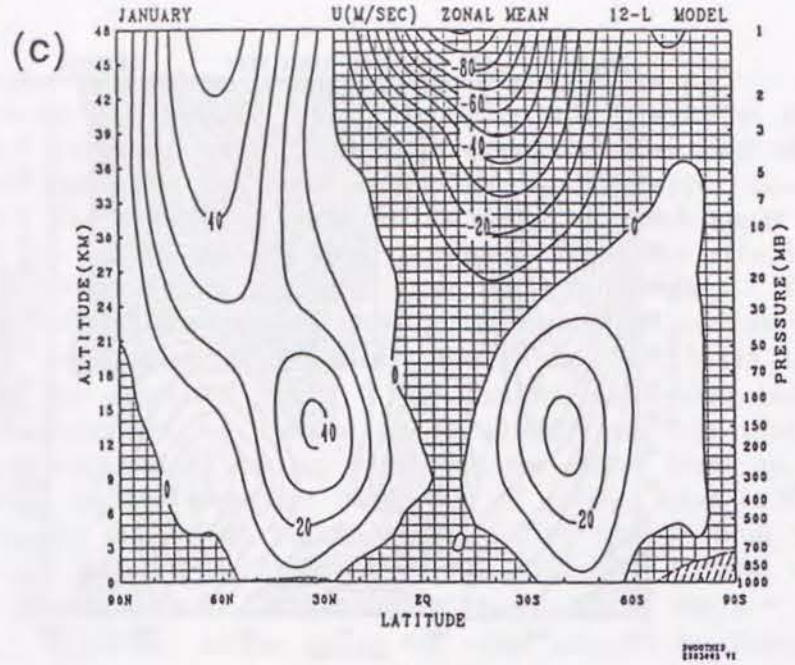

Figure 3.3(c): Zonally and monthly averaged westerly winds (ms^{-1}) for IGW/6 (gravity wave drag experiment with the parameter $\kappa \approx \kappa_0/6$). The contour interval is 10 ms^{-1} and negative values are shaded.

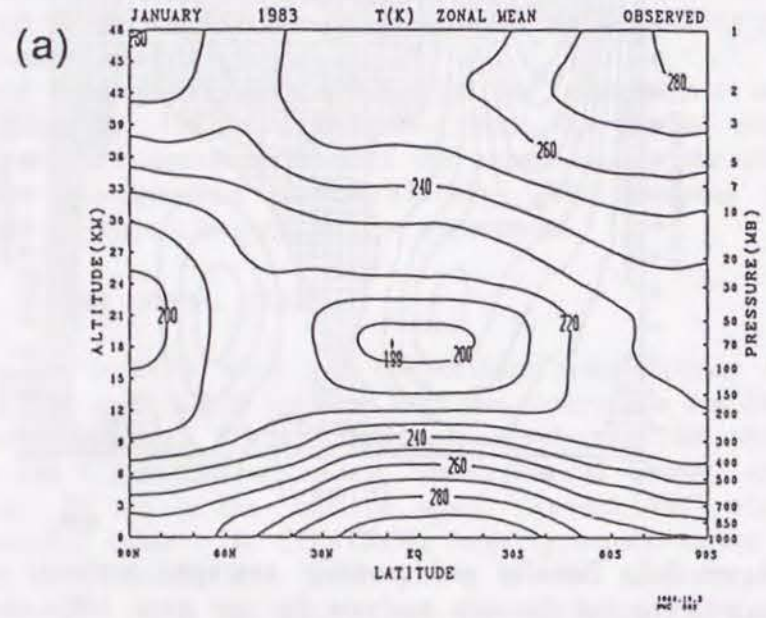

Figure 3.4(a): Zonally and monthly averaged temperature (K) for January analysis for the year 1983.

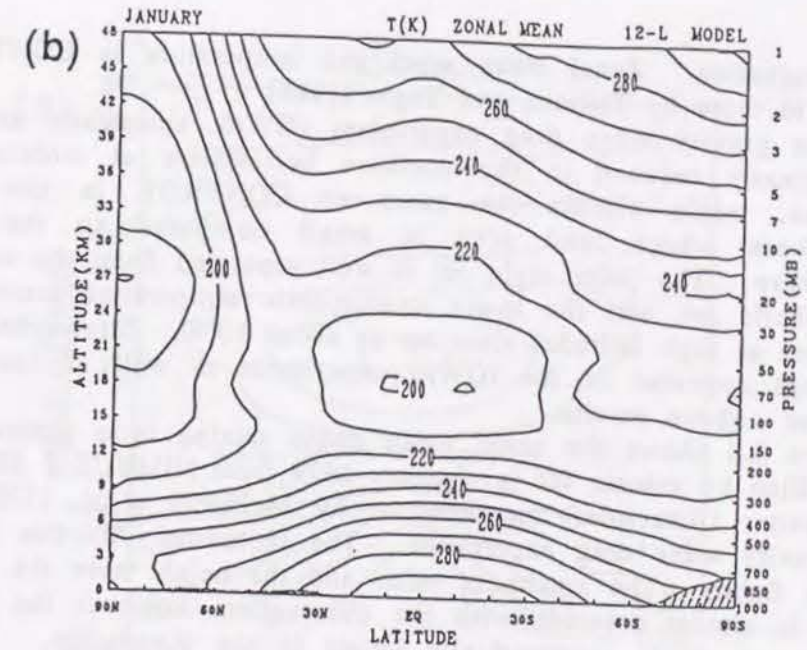

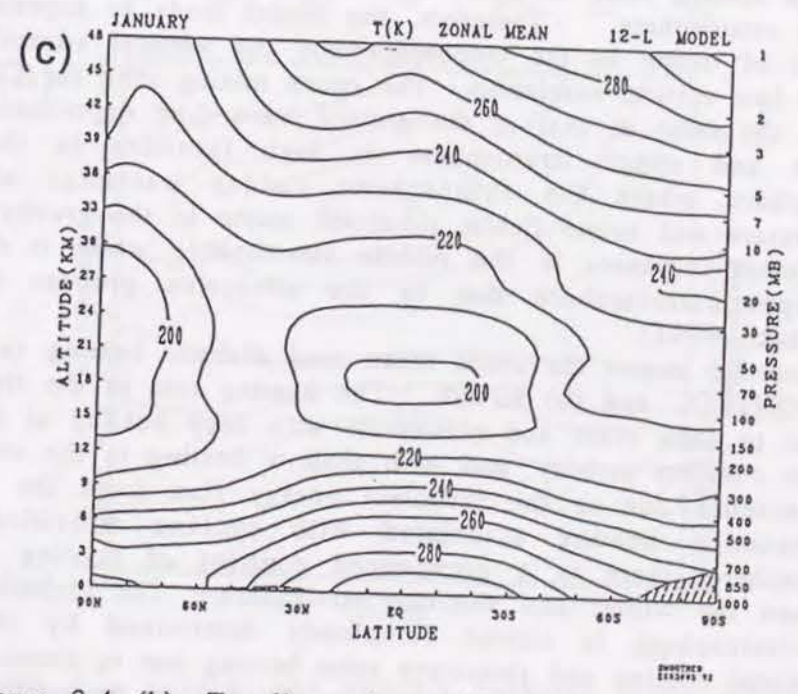

Figure 3.4 (b): Zonally and monthly averaged temperature (K) for the CONTROL simulation, and (c) IGW/6 The contour interval is 10°K.

the observation. Zonal mean wind and temperature in CONTROL are similar to those by Tokioka and Yagai [1984]

In the gravity wave drag experiment IGW/6, systematic errors have been greatly reduced in the northern hemisphere at middle to high latitudes, while almost the same as CONTROL in the southern hemisphere where land area is small compared to the northern hemisphere. The polar night jet is well separated from the mid-latitude tropospheric jet, and the lower stratospheric temperature around the 70 mb level at high latitudes rises up to about 10°K. Stratospheric sudden warmings appeared in the IGW/6 experiment as well as January 1983 reflected above results.

Figure 3.5 shows the zonal mean ozone mixing ratio (ppmv) in parts per million by volume for (a) January 1979 from NIMBUS 7 SBUV (Solar Backscatter Ultraviolet) measurement by McPeters *et al.*, [1984] and (b) the gravity wave drag experiment. The latitudinal direction is changed in this figure. The maximum value and the height over the equator 10 ppmv is almost coincide with the observation, however the value near the tropopause is systematically larger in the simulation. The model predicts mixing ratio of ozone which has large maximum value in the middle stratosphere. Therefore, the model tends to express excessive amount of ozone in the troposphere by the vertical advective process due to low vertical resolution. The ozone mixing ratio for CONTROL is almost the same as that of the gravity wave drag experiment except in middle and upper stratosphere at high latitudes in the northern hemisphere where the stratospheric sudden warmings affected the temperature and ozone fields; simulated ozone in the gravity wave drag experiment increases in the middle stratosphere while it decreases in the upper stratosphere due to the advective process (Yagai and Yamazaki, 1991).

Figure 3.6 shows the zonal mean total diabatic heating rate (K/d) for (a) CONTROL and (b) IGW/6. The heating rate in the troposphere is similar to each other and reasonable with deep heating at low latitudes due to cumulus activity, and with shallow heating in the subtropics and mid-latitudes due to the turbulent energy flux from the surface and condensation heating associated with cyclone activities. In the stratosphere, there is a pronounced contrast of cooling and heating between the winter and summer hemisphere. The diabatic heating in the stratosphere is almost completely determined by the longwave radiational cooling and shortwave solar heating due to ozone. In IGW/6, we can find large cooling, more than 4°K/day, in the polar night region in the upper stratosphere; this is caused by the larger longwave radiational cooling since the temperature in this region is higher in IGW/6 than in CONTROL by the stratospheric sudden warmings.

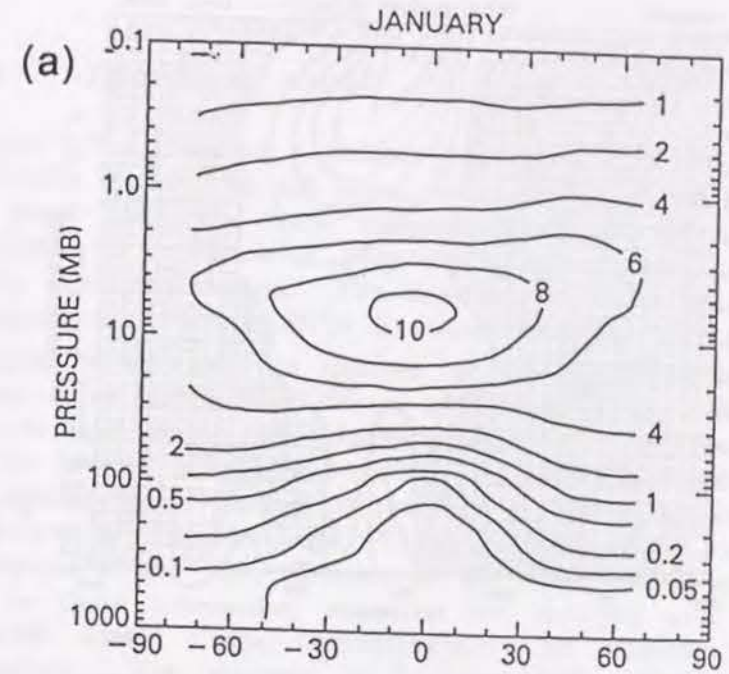

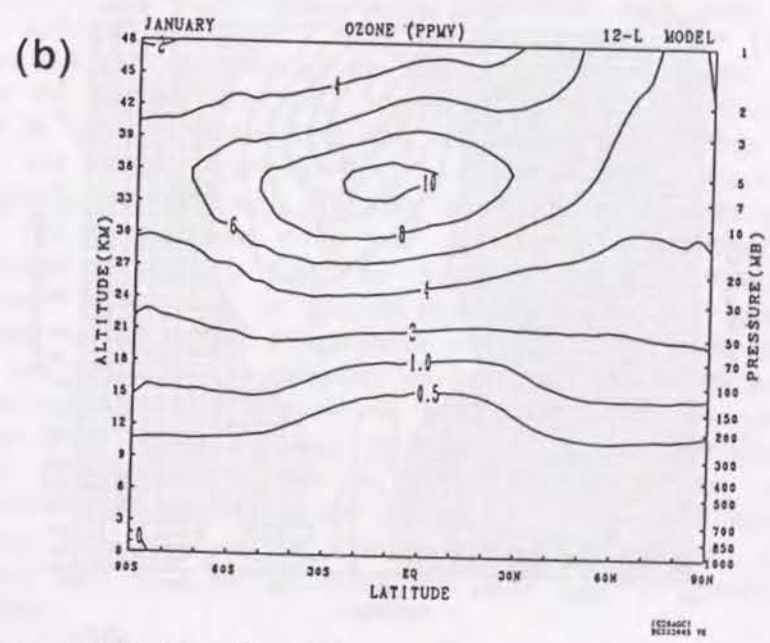

Figure 3.5: Zonally and monthly averaged ozone mixing ratio (ppmv) for (a) January 1979 from NIMBUS 7 SBUV measurement by McPeters *et al.*, [1984] and (b) the gravity wave drag experiment.

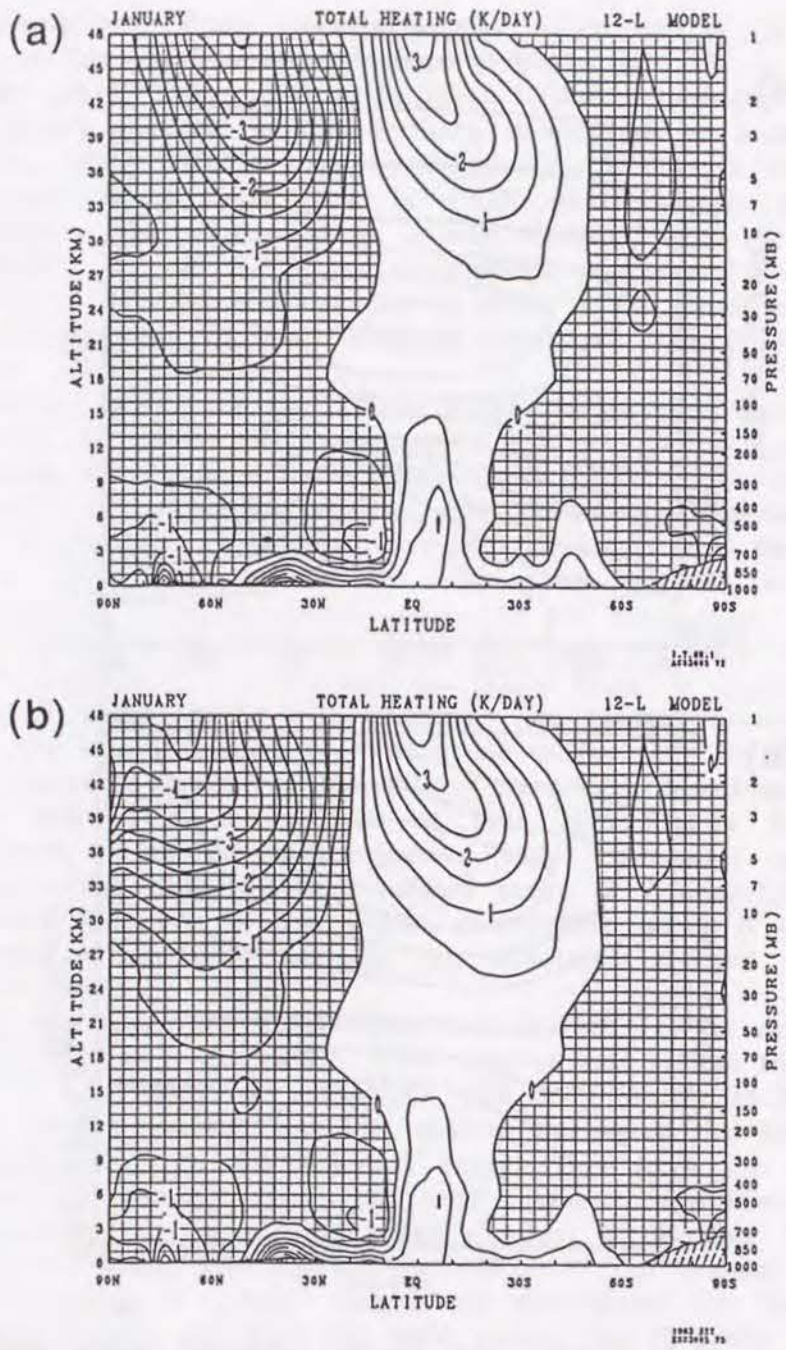

Figure 3.6: Zonally and monthly averaged total diabatic heating (K/day) for (a) the CONTROL simulation and (b) IGW/6. Regions of cooling are shaded.

3.2.3 Planetary waves

Figure 3.7 (a) shows a latitude-time section of the zonal wind for CONTROL at the 5.18 mb level, the model's second highest layer and with plots from the initial value, and Figure 3.7 (b) is the zonal wavenumber 1 amplitude of geopotential at the same level. Regions of easterly wind are shaded. The time-height section of the wavenumber 1 geopotential height at 70°N is shown in Figure 3.7 (c); the value is multiplied by $\sqrt{p/1000}$ to account for the density variation with height and the value larger than 100 m is shaded. The peak in geopotential amplitude that appears on 1 January at the 5.18 mb level can be traced from the lower troposphere beginning with 22 December. However, the peak appears on 11 January at the 5.18 mb level cannot be traced from the below. Tokioka and Yagai [1984] found such barotropic disturbances in the time variation of the amplitude of wavenumber 1 at 50°N in their simulation; most of the maxima and minima in the amplitude occur almost simultaneously at different levels in the stratosphere. The westerly jet is intensified with time and westerly biases appears.

Figure 3.8 (a), (b), and (c) are the same kind of figures as Figure 3.7 but for the gravity wave drag experiment IGW/6. The zonal mean wind profile is quite different from that of CONTROL. When the planetary wave, the zonal wavenumber 1 in this case, reached into the stratosphere intermittently, warming events occur in this period, during which the temperature rises and the zonal mean winds decreased. Transition to easterly flow at the 5.18 mb level occurs near 18 December. The peak in geopotential amplitude that appears near 30 December in the upper stratosphere can be traced from the below but others are not. It is interesting to note that the wind deceleration by the planetary wave 1 also occurs in CONTROL but it is suppressed by the westerly bias; strong westerly jet prevents to transmit planetary waves in the stratosphere. As a result, the maximum amplitude in geopotential that appears in the middle of December is more than 1000 m at the 5.18 mb level in IGW/6, while in CONTROL, the amplitude decreases with time and becomes less than 1000 m toward the end of December.

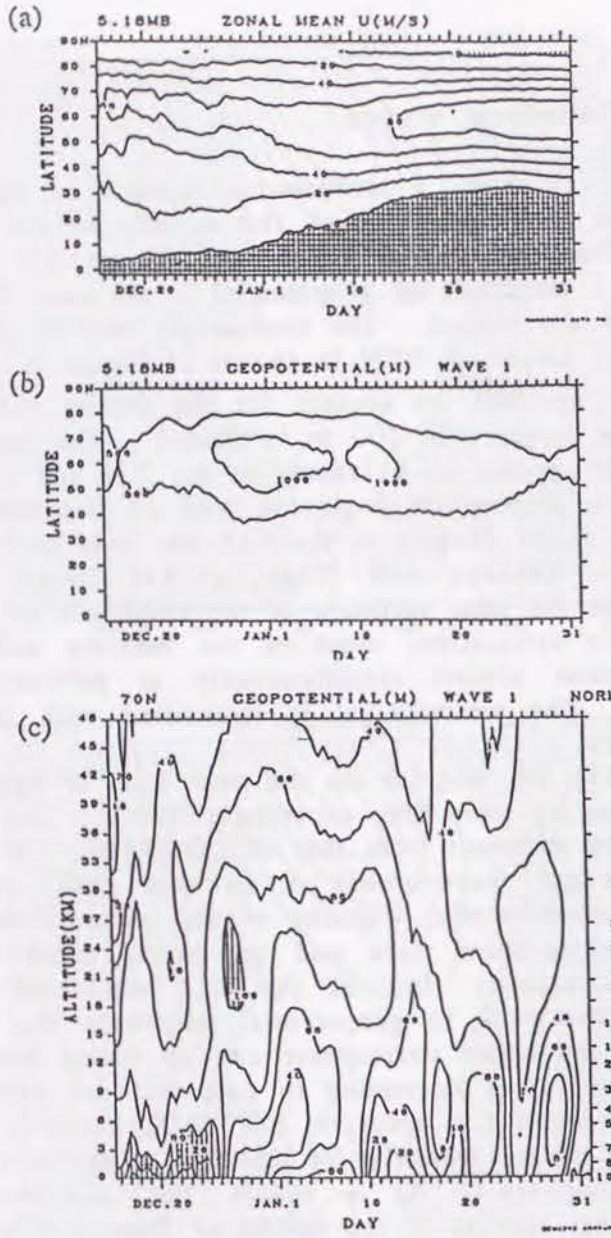

Figure 3.7: (a) Latitude-time section at 5.18 mb of the zonal wind (20 ms^{-1} contours) for CONTROL(κ=0). Negative values are shaded. (b) Latitude-time section at 5.18 m of wave-1 amplitude of geopotential height (m). (c) Time-height section of wave-1 amplitude of geopotential height multiplied by $\sqrt{p/1000}$ at 70°N. Values larger than 100 are shaded.

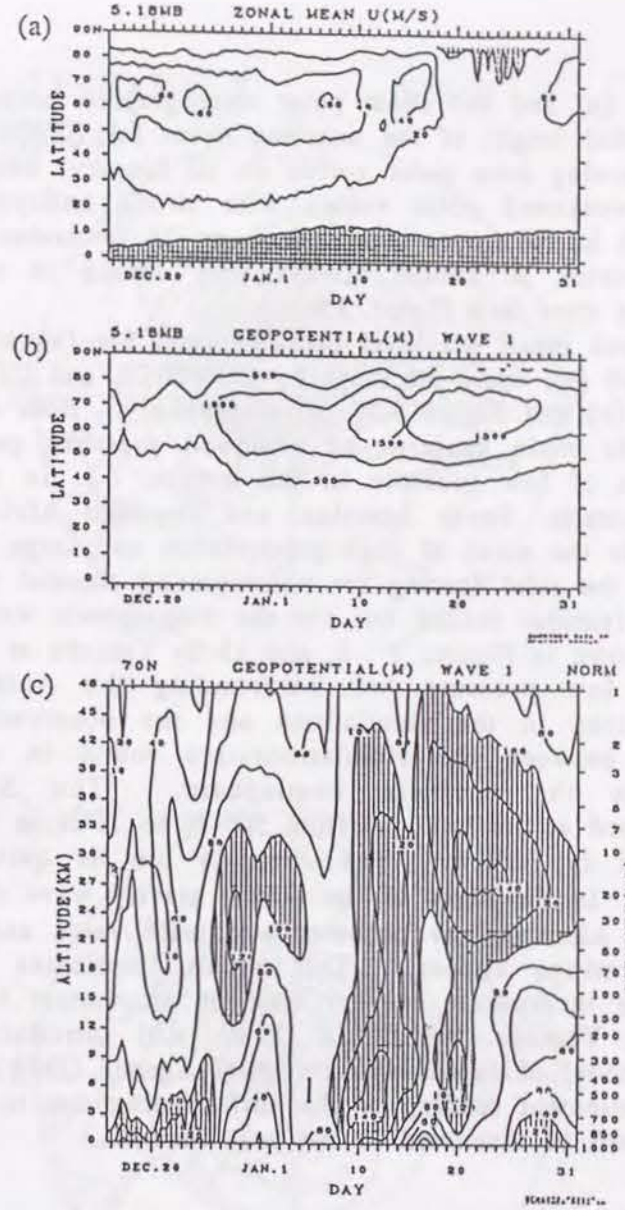

Figure 3.8: (a) Latitude-time section at the 5.18 mb level of the zonal wind (20 ms^{-1} contours) for the gravity wave drag experiment IGW/6. Negative values are shaded. (b) Latitude-time section at 5.18 m of wave-1 amplitude of geopotential height (m). (c) Time-height section of wave-1 amplitude of geopotential height multiplied by $\sqrt{p/1000}$ at 70°N. Values larger than 100 are shaded.

Figure 3.9 (a) and (b) show polar stereographic projections of the 10 mb geopotential height of the warming event for IGW/6. Figure 3.9 (a) is the prewarming deep polar vortex on 10 January, while Figure 3.9 (b) shows the weakened polar vortex with strong anticyclonic circulation, Aleutian high in the upper stratosphere, on 23 December. In CONTROL, the polar vortex is almost always very strong in this period, thus appearing the state like Figure 3.9 (a).

The observed mean sea level pressure field for January 1983 is shown in Figure 3.10 (a), while the maps by CONTROL and IGW/6 are shown in Figure 3.10 (b) and Figure 3.10 (c) respectively. Both of the simulations reproduce the main features of observed pressure patterns; there are three centers of low pressure in the tropics, *i.e.* in the north-western part of Australia, South America, and southern Africa. Those areas correspond to the areas of high precipitation and large heating, which is essential to the tidal forcing for nonmigrating thermal tides described in chapter 4 (similar results but for the tropospheric version of the MRI GCM are shown in Figures 7 , 8, and 15 by Tokioka *et al.*, 1985). There is a deep low pressure belt surrounding the Antarctica, which is commonly seen in the simulations and the observations. The large differences between the simulations are found in middle and high latitudes in the northern hemisphere. The Siberian high is underdeveloped at the latitudes from 50° N to 70°N in CONTROL, which is improved in IGW/6. The Aleutian low is quite intense in the simulations. In the cases of too strong gravity wave drag ($\kappa \geq \kappa_0/3$), the intensity of Aleutian low becomes a climate value and no stratospheric sudden warmings appear. This result implicates that it may be necessary to incorporate another sink of momentum in the troposphere as Iwasaki, Yamada, and Tada [1989, a,b] introduced in the global prediction model of Japan Meteorological Agency (JMA). Further trial of model improvement relating to the surface drag due to the subgrid scale orography will be discussed in the next section.

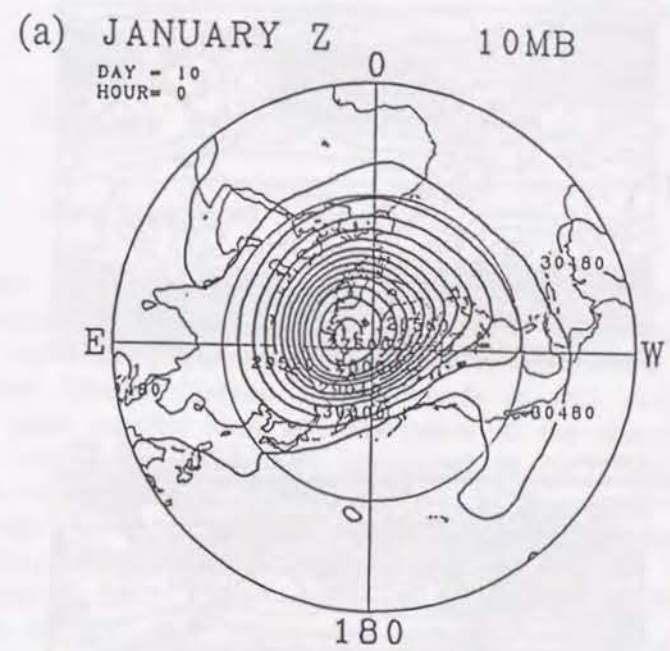

Figure 3.9: Horizontal map of geopotential field at 10 mb for $\kappa_0/6$ at (a) 10 January and (b) 23 January. Contour intervals are 240 m.

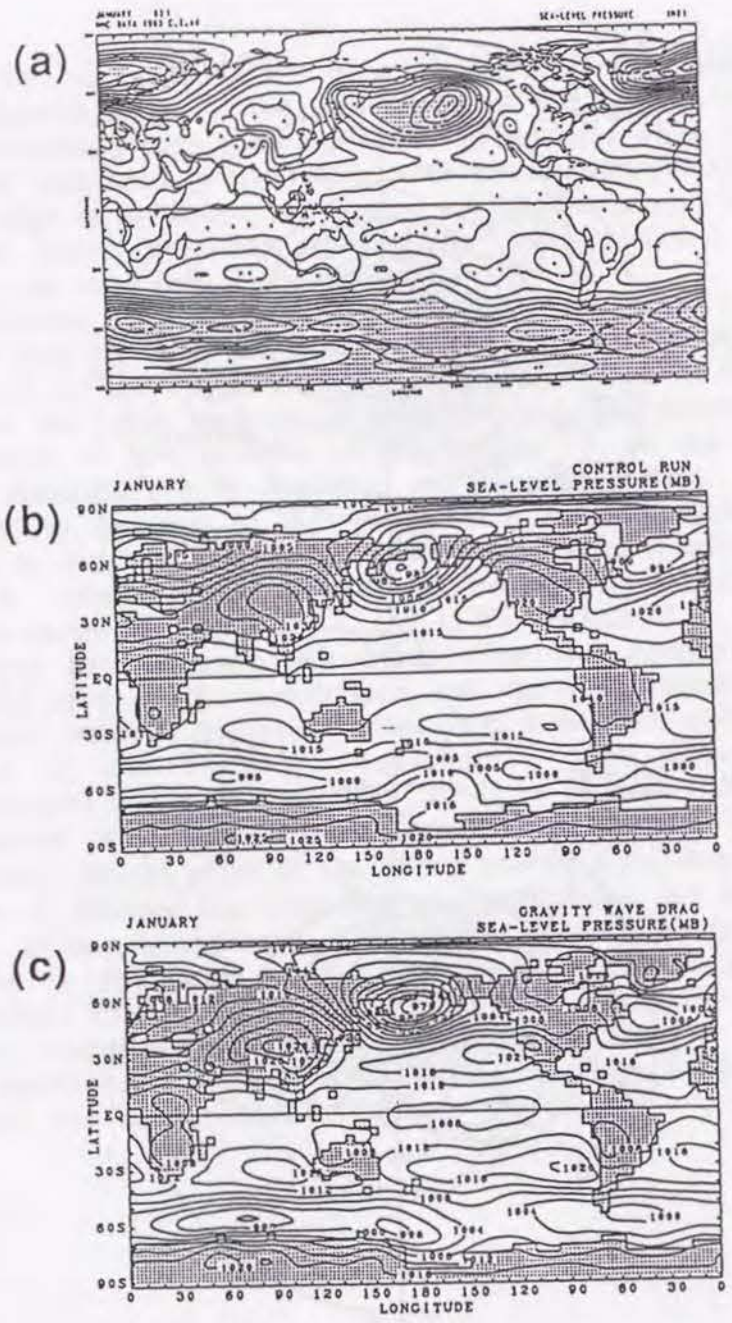

Figure 3.10: Horizontal map of sea level pressure field for (a) January analysis for the year 1983, (b) the CONTROL simulation, and (c) IGW/6. The contour interval is 4 mb in the observation and 5 mb in the simulations.

3.3 Model improvement trial

3.3.1 Introduction

As seen in the previous section, stratospheric circulation of the 12 layer version of the MRI GCM was greatly improved by incorporating gravity wave drag parameterization. However, the anticyclonic flow around the Tibetan Plateau at low levels is still very strong; it seems that we need another sink of momentum in the troposphere as Iwasaki, Yamada, and Tada [1989, a,b] introduced in the global prediction model of Japan Meteorological Agency (JMA). In this section, another trial of model improvement that also relates to sub-grid-scale topography and surface drag is discussed following Yagai and Tokioka [1987].

We still do not know much about the appropriate modeling for exchange of heat and momentum between the earth's surface and the atmosphere over the continents, especially when the planetary boundary layer (PBL) is stable. The absence of turbulence is shown theoretically when the bulk Richardson number of the PBL (R_i) is greater than 1/4. However, irregular surface conditions can cause turbulent motions even when $R_i > 1/4$. There are many irregularities within a grid box of several hundred kilometer square over the continents, *i.e.*, sub-grid-scale topography, variation of vegetation and of land use, *etc.*. In the numerical simulation of the January climate with the 5 layer (tropospheric) version of the MRI GCM-I, Tokioka *et al.* [1985] found that the model atmosphere feels a much smoother surface than it would be in the northern hemisphere. As a consequence, the simulated anticyclonic flow around the Tibetan Plateau is too strong, bringing dry and cold air along the eastern periphery of China, too strong easterly in the southern part of the Plateau, and thus causing enhanced evaporation over the Bay of Bengal and heavy precipitation over the equatorial Indian Ocean. The sea level pressure over both northwestern North America and Europe is lower than observation, partly due to intrusions without much weakening of low pressure disturbances onto the continents.

Deardorff's [1972] transfer coefficient is used in the MRI GCM-I to parameterize the surface stress and the surface energy flux. Cressman [1960] introduced the so called Cressman drag coefficient, which is roughly proportional to the large scale topography, to improve forecasts

with a barotropic model. In Deardorff's scheme, the surface drag coefficient is increased only by increasing the roughness length when the bulk Richardson number is fixed. However, even when the roughness length is increased by two orders of magnitude, the increased drag coefficient is small compared with the Cressman drag when the PBL is stable. Recently, Boer *et al.* [1984] and Sumi [1985] performed numerical experiments by using increased surface drag coefficient. The effects of increased surface drag are not separated clearly in those experiments since, simultaneously, Boer *et al.* [1984] included a parameterization of internal gravity wave breaking and Sumi [1985] introduced vertical eddy diffusions. The purpose of this study is to investigate the effect of the increased surface drag coefficient on the atmospheric circulation. we will discuss how the increased surface drag excites planetary-scale as well as regional changes.

3.3.2 Experimental design

The 5 layer (tropospheric) version of the MRI GCM-I that does not include gravity wave drag is used in this experiment. The model is described in chapter 2 and the diurnal variation of the solar insolation is included, however, the sun is fixed to the mean January position in this experiment. The distribution of sea surface temperature and sea ice are prescribed based on the climatological data.

We performed three experiments for this investigation. The first is the control experiment, D_0, where the model is integrated for 480 days. Selected results from this run are reported in Tokioka, Kitoh and Katayama [1986] and Tokioka and Noda [1986]. The second is an increased surface drag experiment, D_1, with the drag coefficient, C_D^1, given by,

$$C_D^1 = C_D\,(1 + \delta_m)\,. \qquad (3.2)$$

Here, C_D is the Deardorff's drag coefficient used in the control case (see Figure 8.3 of Tokioka *et al.*[1984]) and δ_m, is the standard deviation of sub-grid-scale topography normalized by 100 m and calculated in the 4°x5° region by using 0.2°x0.25° data of topography. Figure 3.2 shows the distribution δ_m that is used in the gravity wave drag experiment. Since δ_m, is not proportional to the large scale topography, C_D^1 and Cressman [1960] drag coefficient have different distributions.

The last experiment, D_2, is also the increased drag experiment, but the drag coefficient over land, C_D^2, is given by,

$$C_D^2 = C_D \cdot f(R_i) \qquad R_i \geq 0\,. \qquad (3.3)$$

Here, $f(R_i)^*$ is a function of the bulk Richardson number of the PBL, R_i. We do not know what kind of surface condition actually contributes to the increase of the drag coefficient over the continent. If the smaller scale irregularities than sub-grid-sale topographies counted in (3.2) contributes to the increase, the modification factor of C_D may rather be a uniform function of space. The C_D^2 is adopted with such a speculation in mind.

D_1 and D_2 are integrated for 60 days with the use of the same initial condition as that of D_0. The initial condition is taken from January 1 of an annual march time integration with the original MRI GCM-I. So the experiment in this section is free from the problems related to initialization.

The results of D_2 do not differ much from those of D_1 quantitatively as well as qualitatively in rough sense. Therefore most of the analyses and results in this section are confined to D_0 and D_1.

3.3.3 Impact of the increased C_D over the continents on the time mean fields

a. Surface stress and wind field

The effect of increased surface drag coefficient on the general circulation is studied at first. For this purpose, the analysis is performed for the data averaged over the last 30 days of integration.

The change of the surface stress causes changes in the flow. Figure 3.11(a) shows the mean surface stress vector in D_0. The wind vector at the lowest level is quite similar to the stress vector in Figure 3.11(a) but in the opposite direction. Figure 3.11(b) shows the stress vector difference between D_1 and D_0. The change of the surface stress depends on the changes of both the drag coefficient and the PBL wind. The increase of the drag coefficient is prescribed by equation (3.2), whereas the change of the PBL wind results not only from the local dynamical balance but also from the global circulation of the atmosphere. Figure 3.12 shows the 900 mb wind vector difference between D_1 and D_0, which gives us a good measure for the change of the PBL wind.

---

* $f(R_i)$ is defined as

$$f(R_i) = 1. + (1. - 0.28R_i)\,(1. + A \cdot R_i^{1.2}) \quad 0 \leq R_i < 5\,.$$

$$f(R_i) = 1., \quad 5 \leq R_i$$

where "A" is 3.0 for the moment and 4.0 for the energy flux. When $R_i < 0$, the original Deardorff's drag coefficient is adopted.

(a)

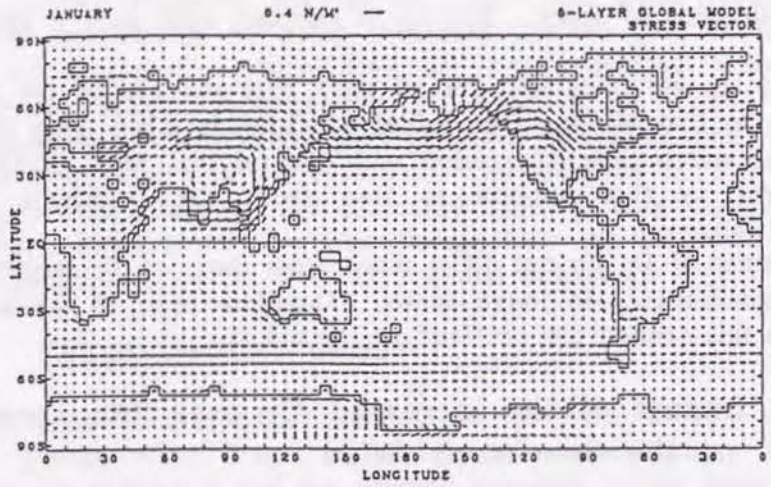

(b)

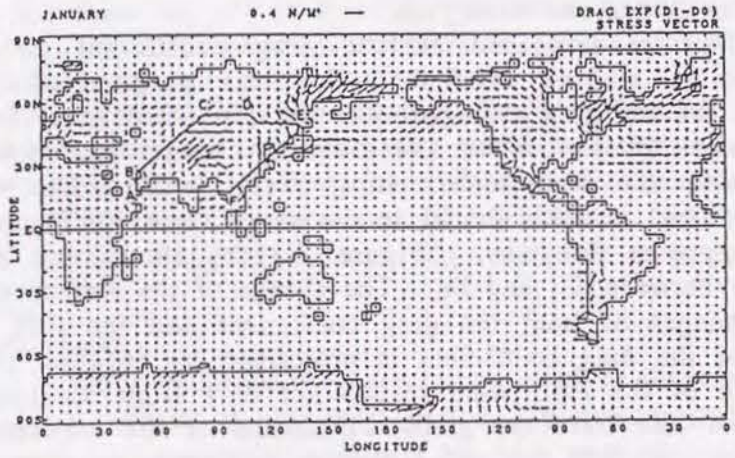

Figure 3.11: (a) Surface stress vector in D_0 averaged for the last 30 days (unit: Nm^{-2}). (b) The 30-day averaged difference, D_1-D_0, of the surface stress vector. Thick line indicates the adopted path in the Hovmöller diagram in Fig. 3.20 (a) and (b).

Comparison of Figure 3.11(b) and Figure 3.12 shows that, vector change occurs in the same direction where the 900 mb wind vector difference is relatively small, *e.g.* in the area along the northern periphery of the Tibetan Plateau. On the other hand, the change occurs in the opposite direction where the 900 mb wind vector difference is relatively large, *e.g.* in Canada and the eastern part of the United States. However, vectors in Figure 3.12 and Figure 3.11(a) are in good agreement, *i.e.* the low level wind speed is reduced over land in D_1. For example, the anticyclonic flow surrounding the Tibetan Plateau, which is too strong in D_0 (not shown), is substantially reduced in D_1. This causes the temperature rise near the central part of Indo-China Peninsula at 900 mb. There is a pronounced cyclonic flow over the North Atlantic in Figure 3.12. The Icelandic low is intensified and shifted southward in D_1.

Figure 3.13 shows the wind vector difference between D_1 and D_0 at 500 mb. A wave-train is seen originating from the north of the Indo-China Peninsula to the Pacific. This wave-train reduces the intensity of the too deep trough over the Indo-China Peninsula and too high ridge over south of Japan. The wave-train seems to be trapped equatorward of the poleward flank of the jet because the wave length of the wave-train is rather short (Hoskins and Karoly, 1981).

b Vorticity at 900 mb

Figure 3.14 shows the vorticity field at 900 mb in D_0 and the difference of the same quantity between D_1 and D_0. Positive area of the former is hatched in longitudinal direction and the negative area of the latter in latitudinal direction. The figure seems to be quite complicated, however, we can find some regularities in it. The non-shaded area indicates the weakening area of negative vorticity, and the cross-hatched area that of positive vorticity. The non-shaded and cross-hatched area over the continents cover 70 % of the entire continents and 88 % if we limit the counting for the area where the absolute value of vorticity is greater than $1.0\times10^{-5}\ s^{-1}$. They are distributed around the high mountain ranges such as the Tibetan Plateau, the Rockies, the Greenland, the Andes, *etc.*, *i.e.*, the vorticities are weakened by the increased surface drag around high mountains. This feature is seen below 700 mb levels although the correspondence decreases with height.

c Velocity potential at 900 mb and precipitation

Figure 3.15 shows the velocity potential field difference at 900 mb between D_1 and D_0. Arrows in Figures 3.15 correspond to the divergent

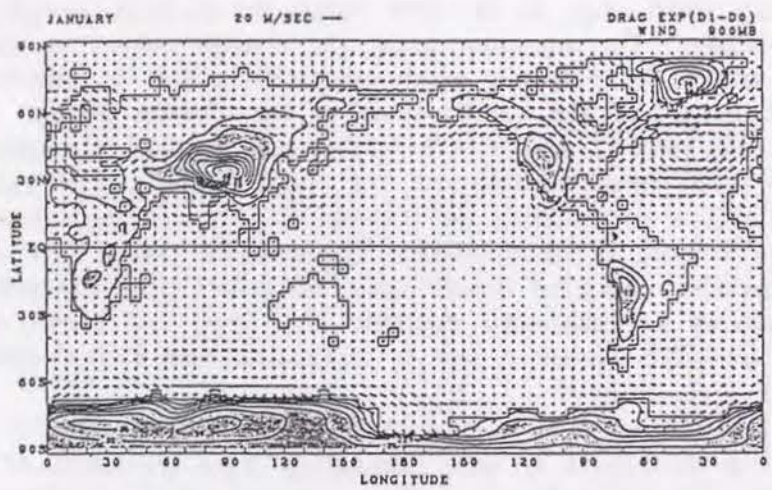

Figure 3.12: The 30-day averaged difference, D_1-D_0, of the wind vector at the 900 mb level. Topography distribution adopted for the model is also plotted (unit: 100 m).

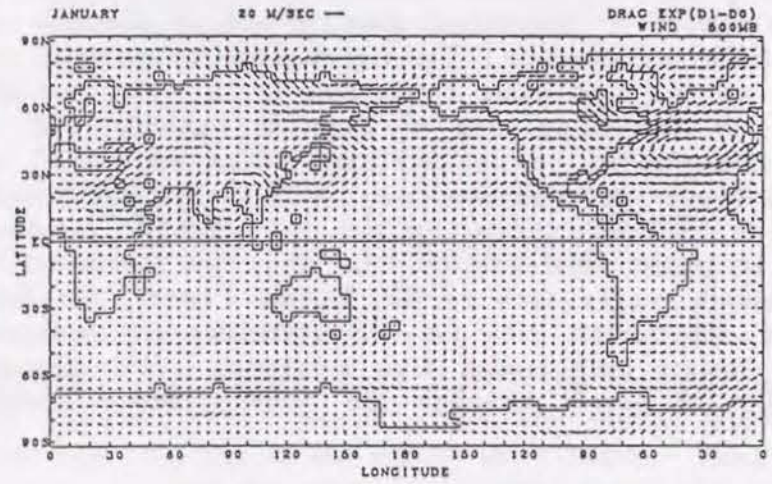

Figure 3.13: The 30-day averaged difference, D_1-D_0, of the wind vector at the 500 mb level.

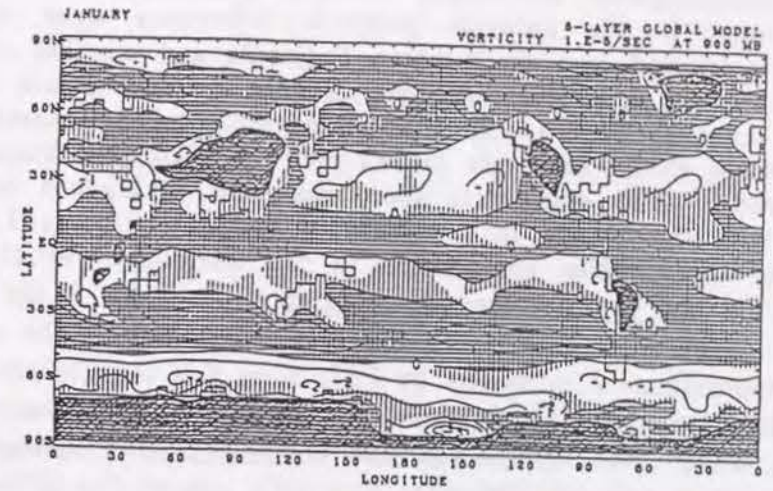

Figure 3.14: Vorticity at the 900 mb level for the control case averaged for the last 30 days (unit: 10^{-5}/sec). Contour interval is 0.5 and positive values are hatched in the longitudinal direction. The difference, D_1-D_0, is also hatched but in the latitudinal direction.

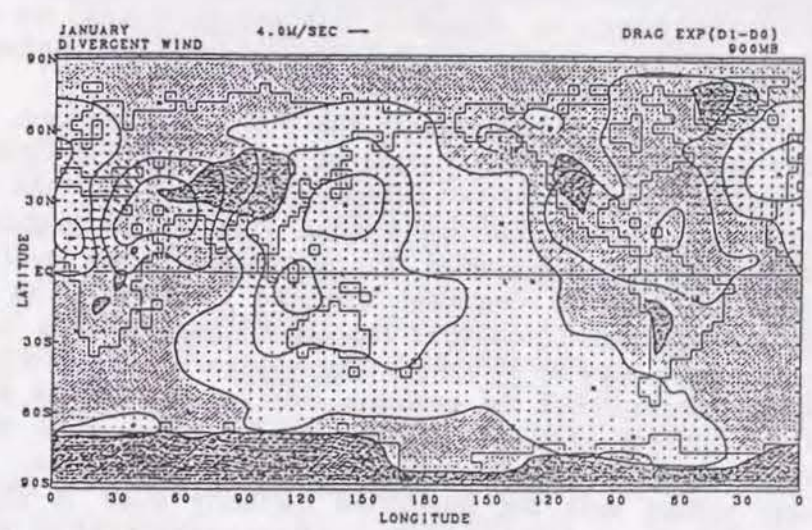

Figure 3.15: The 30-day averaged difference, D_1-D_0, of the velocity potential and the corresponding divergent wind. Contour interval of velocity potential is 10^{-6} m^2/sec.

winds. Although detailed distributions of small-scale divergence/convergence are found in wind vectors, we notice large-scale patterns in the velocity potential difference over Asia. A minimum is located over the Arabian Peninsula and maxima over south of Japan and the maritime continent. Those extreme values are more than five times as large as the standard deviation of the monthly means of the present model based on the 12-year run (Tokioka, Yamazaki and Kitoh, 1986). The change in the large-scale divergence is roughly balanced with the change in the vorticity budget. Figures 3.16 shows changes of three major components in the stationary vorticity budget between D_1 and D_0, i.e. the stretching term f·div ΔV, the planetary vorticity advection term $\beta \Delta v$ and the dissipative term. The dissipative term is approximately estimated by $K\Delta\zeta$. Here f is the Coriolis factor, β the planetary vorticity gradient in the northward direction, ΔV the horizontal wind vector difference, Δv the latitudinal component of ΔV, $\Delta\zeta$ the relative vorticity difference and K a constant (=1/5 day^{-1}). In Figure 3.16, each term is the sum of the components of the zonal wavenumber one to three averaged between 10°N and 30°N at 900 mb. It is confirmed that the vorticity balance of stationary waves of the zonal wavenumber one to three are almost attained among the three components in Figure 3.16. It is also confirmed that the stretching term in the vicinity of the Tibetan Plateau is consistent with the decrease of the anticyclonic flow around the Tibetan Plateau through the $\beta \Delta v$ term. The changes in the velocity potential at higher levels are almost confined in the vicinity of mountains. In another words, the effects of the increased surface drag on the velocity potential are confined almost below the 700 mb level.

In connection with the changes in the 900 mb divergence, we fined good correspondence with the changes in the precipitation field. Figure 3.17 shows the precipitation difference between D_1 and D_0. The divergence area centered on the Arabian Peninsula is associated with the precipitation decrease, while the convergence areas over south of Japan and the maritime continent with the increase. The maximum decrease in the precipitation over the central part of Asia corresponds to the divergence area at 800 mb. The changes of the precipitation on both the downstream and the upstream sides of the Tibetan Plateau are due to the changes in the large scale condensation, while that of the maritime continent to the changes in the cumulus convection. The latter is closely related with the intensified northerly wind in D_1 over the maritime continent (see Figure 3.12). All these changes in precipitation are in the same sense to reduce the model's systematic errors pointed out in Tokioka *et al.* [1985].

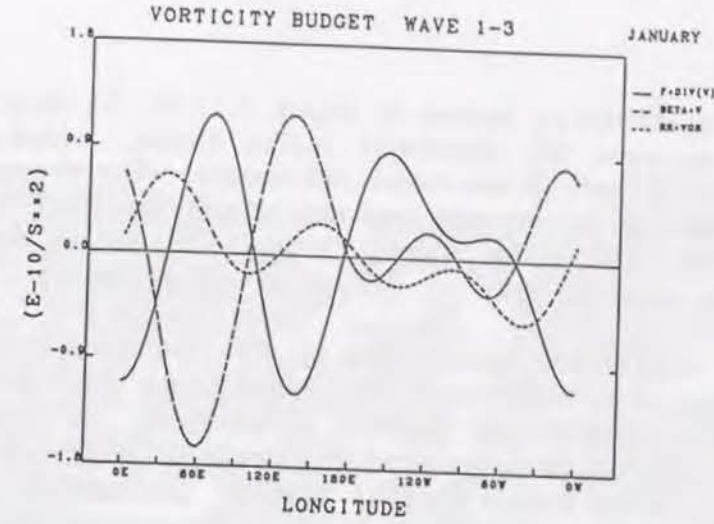

Figure 3.16: Difference in three major terms in the stationary vorticity budget equation between D_1 and D_0 at the 900 mb level. The thick line indicates the stretching term, long-dashed line the planetary vorticity advection, and the short-dashed line the dissipation term. The zonal wavenumber components from 1 to 3 are summed up and averaged between 10°N and 30°N for the last 30 days (unit: 10-10 s-2).

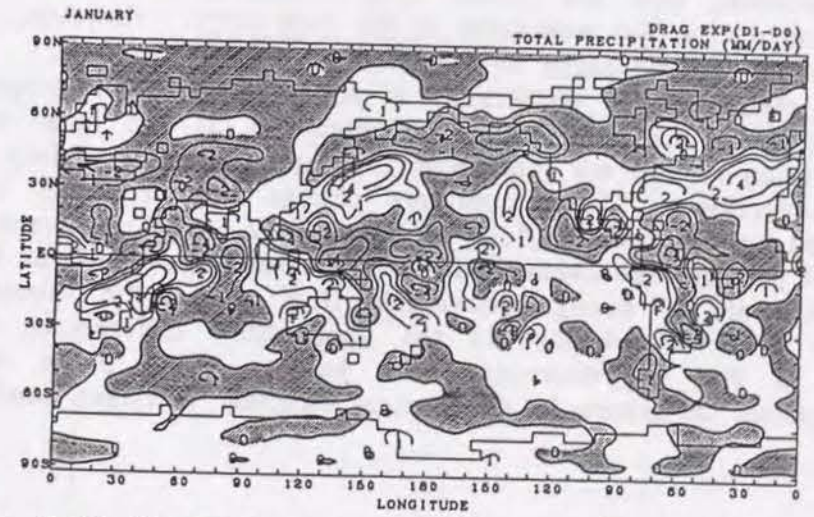

Figure 3.17: The 30-day averaged difference, D_1-D_0, of the total precipitation. Contour intervals are 0, ±1, ±2, ±4 mm/day and negative values are shaded.

The other interesting feature in Figure 3.17 is the large decrease of precipitation over the equatorial Indian Ocean, which is also an improvement of one of the model deficiencies. The decrease is due to the weakening of the dry and cold anticyclonic low level flow along the southern periphery of the Tibetan Plateau in D_1 and to the decrease of evaporation over the Bay of Bengal, as speculated by Tokioka *et al.* [1985].

Most of the features stated so far are also confirmed in D_2, however, some systematic differences are found over the area from the Mediterranean Sea to the northern periphery of the Tibetan Plateau, where transient disturbances tend to intrude in the eastward direction more often in D_2 than in D_1. As a result, precipitation increases and surface pressure decreases there in D_2. This implies one of important roles of sub-grid-scale topography around the Alps and the Iranian Peninsula in preventing the intrusion of transient disturbances from the west.

d Temperature at 900 mb

Figure 3.18 shows the temperature difference at 900 mb between D_1 and D_0. The geographical distribution of the temperature difference in Figure 3.18 is different from that of the similar experiment by Sumi [1985]. In his 72 hour forecast, the temperature is raised around Japan by increasing both the surface drag coefficient and the vertical eddy diffusion due to the weakening of the cold surge. However, in D_1, the temperature around Japan is decreased in the last 30 days.

The change of the temperature at 900 mb in the extratropics is well explained by the wind difference (Figure 3.12) and mean temperature distribution at 900 mb (not shown), as the change is mainly caused by the advection. The temperature change around Japan is strongly affected by the cyclonic flows in Figure 3.12. The temperature near the central part of Indo-China Peninsula is raised by as much as 8°K by the decrease of too strong anticyclonic flow around the Tibetan Plateau. Small scale disturbances in the temperature differences, dominantly seen at 900 mb decreases with height. The phase tilt of the temperature difference in the vertical direction is rather small.

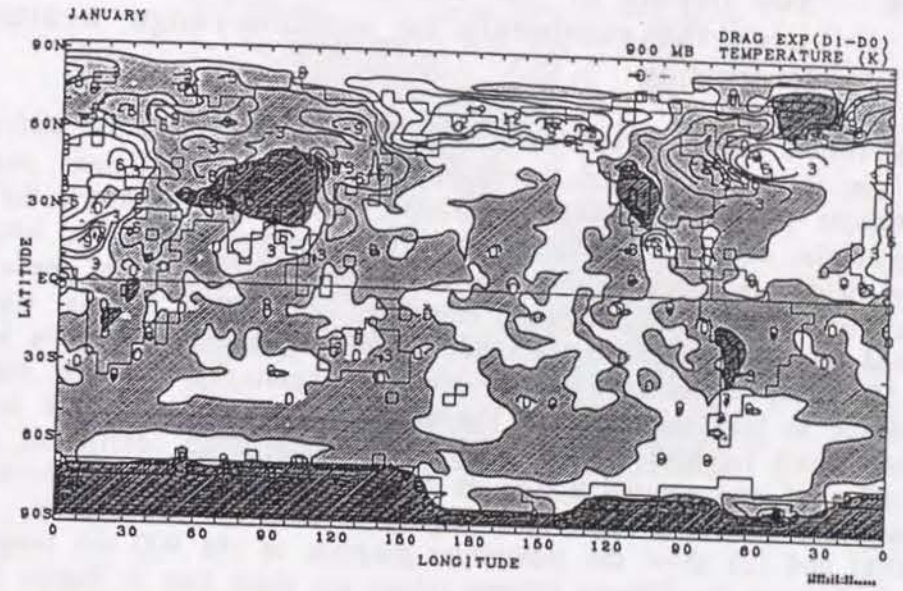

Figure 3.18: The 30-day averaged difference, D_1-D_0, of the temperature at the 900 mb level. The contour interval is 3°K and negative values are shaded.

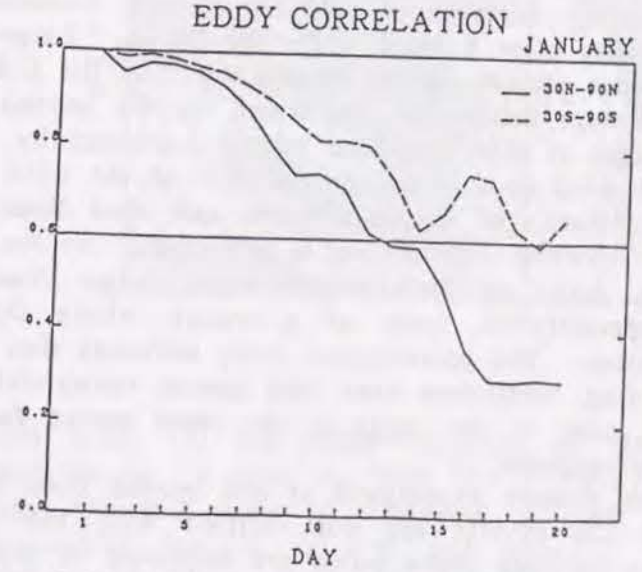

Figure 3.19: Eddy geopotential correlation at the 500 mb level between D_1 and D_0 for the first 20 days.

3.3.4 The impact of the increased drag coefficient over the continents on medium-range weather forecasting

The results for the first 20-day of D_0 and D_1 are specially analyzed to see the influence of the increased surface drag coefficient over the continents on medium-range forecasts. Figure 3.19 shows the eddy geopotential correlation at 500 mb level between D_0 and D_1, where the eddy fields are calculated as the deviation from the zonal mean state. Thick line shows the correlation calculated in 30°N-90°N area, while the dashed line the one calculated in 30°S-90°S. Correlation is quite high up to 10 days, especially in the southern hemisphere where the land coverage is less than that in the northern hemisphere. This indicates rather small impacts of the increased surface drag coefficient on the variation of geopotential eddies at 500 mb. However, the above result does not deny not a small local impact of it at the lower level. Figure 3.20(a) and (b) show the Hovmöller diagram of the 900 mb temperature of D_0 around the Tibetan Plateau (along the thick line in Figure 3.12(b)) and the same quantity but for the deviation of D_1 from that of D_0, respectively. 20-day averages are subtracted in Figure 3.20 (a) at each grid point. In this period, two major cyclonic disturbances passed the C-E zone in the eastward direction. We notice systematic positive deviation around the point F (the central part of the Indo-China Peninsula) due to the decrease of cold anticyclonic circulations around there, which appears after 8 hours from the initial. Large differences are established there already on the second day. In the C-E zone also, not small temperature differences are found on the second day. The temperature changes at this stage are mostly explained by the changes in the horizontal wind (mostly by the decrease of the wind velocity) at 900 mb. Phase velocity of the disturbances and wind directions are not much different between D_1 and D_0 at this stage. At the latter stage, changes in the paths of disturbances cause large changes in the temperature, especially in front of a trough where the effect of advection dominates. The present case study indicates that the increase of the surface drag coefficient over land causes substantial changes in the temperature, even in the range of the short period forecasting, in the low level atmosphere.

Of course, the present experiment is not started from the observed state, therefore the results are not verified with the observations. However, as the monthly mean states are improved in several respects in D_1 as stated in section 3.3.3, the surface drag coefficient adopted in D_1 may have some physical meanings.

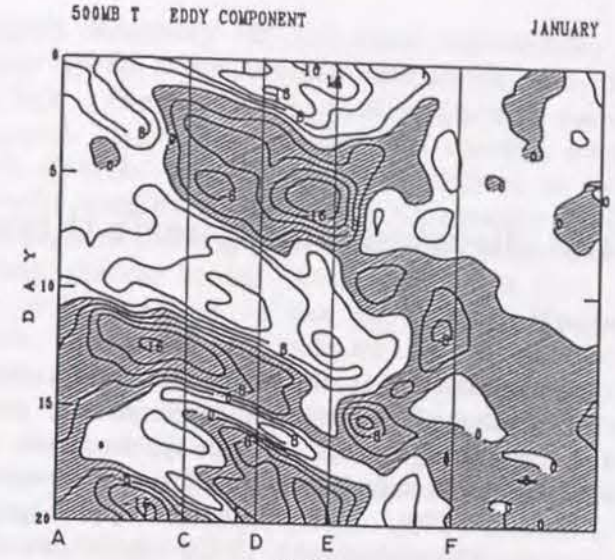

Figure 3.20: (a) Hovmöller diagram of the 900 mb temperature in D_0 along the thick line in Fig.3.12 (b). The 20-day averaged value is subtracted at each grid point. The contour interval is 4°K and negative values are shaded. (b) Same as in (a) but for the temperature difference, D_1-D_0.

Chapter 4

Simulated and observed atmospheric thermal tides

4.1 Introduction

It is known, theoretically, that the effect of longitudinal variation in the distribution of insolation absorption produces not only a component following the sun (migrating mode, or sun-synchronous mode), but also other components which do not move synchronously with the sun [e.g., *Chapman and Lindzen*, 1970]. Tropospheric water vapor has significant longitudinal variations [*Newell et al.*, 1972] which could create possible excitation of nonmigrating modes (or sun-asynchronous modes). Moreover, the diurnal cycle of Planetary Boundary Layer (PBL) depth is prominent over land, especially desert areas such as the Sahara, and less so over the ocean [*Suarez et al.*, 1983; *Tokioka et al.*, 1984 chapter 8]. These land-sea contrasts also excite nonmigrating modes.

Historically, the observational studies of the solar tide have used long term series of barometric measurements at many stations [*Haurwitz*, 1956, 1965; *Haurwitz and Cowley*, 1973]. Haurwitz and his coworkers calculated diurnal surface pressure oscillation $S_1(p)$ and semidiurnal surface pressure oscillation $S_2(p)$ of each station data, and then did a spherical harmonic analysis to see the geographical distribution of component waves. *Haurwitz and Cowley* [1973] showed larger diurnal surface pressure oscillation over land areas than over ocean areas and attributed it to nonmigrating modes. Then, they calculated spectrum distribution of wave amplitude of component waves. Note that the period of data they used was long enough to isolate diurnal variations from non-diurnal disturbances. However, the data distribution over the earth was uneven and the number of stations was insufficient especially at low latitudes in the southern hemisphere. Therefore, it may be useful to calculate diurnal variation of the sea level pressure field, spectrum distribution of wave amplitude and its latitudinal distribution, *etc.*, using the improved data sets.

Tokioka and Yagai [1984] found a dominant nonmigrating tidal mode in a general circulation (GCM) simulation in January. Its zonal wavenumber (m) is five and the mode propagates westward with the frequency of 1 day^{-1}, (f=-1, m=5)· The pair (f, m) characterizes waves

by their angular frequency $f\Omega$ and zonal wavenumber m, where Ω is the earth's angular speed. For diurnal oscillations, f=1, and for semidiurnal oscillations, f=2. The positive sign of f indicates eastward moving waves and the negative sign indicates westward moving waves.

Further more, *Tokioka and Yagai* [1987, referred to as TY87] pointed out that the Fourier amplitudes of actual topography at low latitude in the southern hemisphere have a clear peak at zonal wavenumber 4, which generates nonmigrating modes (f=-1, m=5) and (f=1, m=3) through the PBL and cumulus heating in the daytime. These results are quite understandable, since we can estimate almost all variables such as sea level pressure, geopotential height, temperature, diabatic heating, *etc.*, with sufficient quality in the model. However, it was very difficult to confirm the above results by using real data, since there were a small number of observations in time and space in the equatorial regions and southern hemisphere.

The First GARP (Global Atmospheric Research Program) Global Experiment (FGGE), also known as the Global Weather Experiment (GWE), which took place in 1979, provided an excellent opportunity to investigate circulations based on observational data in these areas. The GWE is organized by the World Meteorological Organization (WMO) and the International Council for Scientific Unions (ICSU) to study the dynamics of the transient behavior of the atmosphere with the aim of improving the accuracy and extending the range of useful weather forecasting. The GWE also provides a scientific basis for the World Weather Watch (WWW) program that is still undergoing as a basic programme of the World Meteorological Organization [see WMO, 1987].

Figure 4.1 shows a schematic representation of the data flow and observing system for the FGGE. The World Weather Watch basic observing systems contain surface based network, geostationary satellites, and operational polar orbiting satellites. Since the data coverage provided by the above system is not sufficient, especially in the equatorial tropics and southern hemisphere, the special observing techniques are carried out. The special observing systems contain aircraft , tropical wind observing ships (TWOS), constant-level balloons, drifting buoys, special aircraft, and research satellites. These data have been checked , assembled, and delivered to the two World Data Centres, as well as to the two organizations, the European Centre for Medium Range Weather Forecast (ECMWF) and the Geophysical Fluid Dynamics Laboratory (GFDL). Then, these data are transformed and divided into the following levels:

Level I. *Primary data.* These are instrument readings expressed in appropriate physical units and referred to specific times and locations on earth. An example is the radiation measurements in different

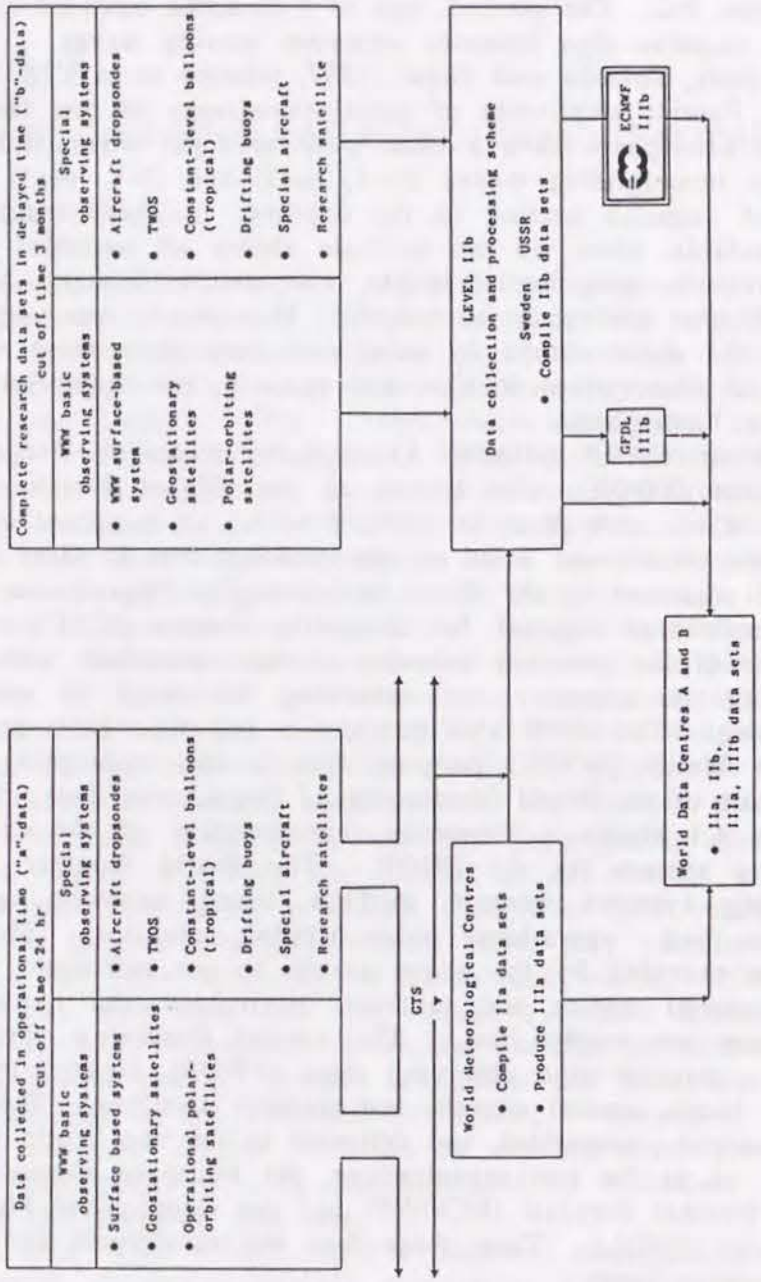

Figure 4.1: The overall data management during FGGE [*Bengtsson et al.*, 1982].

channels from satellites.

Level II. *Meteorological parameters.* These data are values of meteorological parameters at the place and time of observations. They may be obtained directly by the observations such as temperature, or they may be derived from level I data.

Level III. *Initial state parameters.* These are basic meteorological parameters at a regular array at grid points over the globe, which are determined from level II data through a process of four-dimensional assimilation; these are integrated systems of interpolation of meteorological data and numerical forecast process.

Global grid point data sets, so called FGGE Level IIIb data sets, are produced by the two organizations, ECMWF and GFDL. The label "b" denotes all the data collected within a three month cut-off period, while the real-time data are indicated by label "a". The climate data is labeled "c". The ECMWF FGGE IIIb data set includes sea level pressure, geopotential height, wind, temperature, and vertical velocity at 1000, 850, 700, 500, 400, 300, 250, 200, 150, 100, 70, 50, 30, 20, and 10 mb. The relative humidity is analyzed below 300 mb level, and all analyses are made with a horizontal resolution of 1.87°x1.87° latitude-longitude grid. The analyses 0000 GMT and 1200 GMT have been carried out through the year. During the first and second observation periods (SOP-1 and SOP-2) of FGGE which cover the periods 1 January - 5 March 1979 and 30 April - 7 July 1979, analyses have also archived at 0600 GMT and 1800 GMT.

The ECMWF operational model which was used to assimilate observed data and to produce the first-guess forecast, had no diurnal cycle. Therefore, diurnal variations appeared in the FGGE IIIb data sets are not artificially generated by the operational model, but are inherent in the observed data. It is expected that grid point values in the poorly observed area are strongly affected by the forecast values which depend on formulations of dynamical and physical processes of the model. In the stratosphere, where the number of observation is relatively small, the error in the divergent wind, which is caused by the lack of diurnal cycle in the forecast model, is pointed out in the FGGE data [Lönnberg and Hollingsworth, 1985]. An exception is the sea level pressure field which achieves dense data coverage even at low latitudes over ocean by utilizing ship data and buoy network [*Bengtsson et al.*, 1982].

Theoretical study of nonmigrating modes was performed by Kato, Tsuda and Watanabe [1982]. They assumed that the heat source of excitation was localized near the equator and found perturbations with generally short vertical wavelength around 10 km. However, their solution did not explain the dominance of the (f=-1, m=5) and (f=1, m=3)

modes over the possible nonmigrating modes. Recently, Tsuda and Kato [1989] calculated diurnal nonmigrating tides using the classical tidal theory with the heat source assumption localized only in the planetary boundary layer on land. Resulted pressure variations of nonmigrating tides agrees well with the observations by Haurwitz [1965]. Furthermore, horizontal wind velocities are about 2 to 3 m/sec near 20 km altitude with the vertical wavelength 2 to 5 km, which is consistent with ground-based radar observation [Fukao *et al.*, 1980; Tsuda *et al.*, 1985].

Forbes and Groves [1987] incorporated the excitation of nonmigrating modes, which are due to longitudinal variation in diurnal insolation absorption by tropospheric water vapor, to simulate diurnal propagating tides in the low-latitude middle atmosphere. Nevertheless, they did not consider the dominance of the (f=-1, m=5) and (f=1, m=3) modes.

Simulation of solar tides by the GCM was first made by Hunt and Manabe [1968], but, until recently, the study of solar tide by GCMs has been ignored. *Zwiers and Hamilton* [1986] simulated solar tides by the Canadian Climate Centre GCM, one of the sophisticated models, and showed a fairly realistic results compared to the available observations. They also discussed "rigid-lid" upper boundary condition problem which had been noted by *Chapman and Lindzen* [1970]. In the present study, the first special observation period (SOP-1: 10 January to 9 February 1979) of FGGE Level IIIb data sets produced by the ECMWF are analyzed and compared with the MRI (Meteorological Research Institute) GCM simulation. The results are also compared with the simulation by *Zwiers and Hamilton* [1986]. It will be shown that the FGGE data set, especially the sea level pressure field, has an advantage over the previous data sets in the analysis of tidal waves and the MRI GCM successfully simulated solar tides, migrating and nonmigrating modes, in the sea level pressure field.

4.2 The Model and the Observational Data

The model is described in chapter 2 and its performance is presented in chapter 3. The model corresponds to CONTROL in chapter 3, which has no gravity wave drag and simulates relatively strong westerly jet in the winter stratosphere. A long-term time integration was performed for the period from 1 October to 31 January. The data is taken from the last 31 days of the simulation, which is identical to that used in TY87, and sampled every six hours (0000, 0600, 1200 and 1800 GMT). To confirm the results, an hourly data is sampled for particular two days in the simulation.

The FGGE Level IIIb (SOP-1) data sets produced by ECMWF for the period of 10 January to 9 February 1979 are analyzed. Six-hour-interval global data in winter are only available with the FGGE data currently, and the sampling time is exactly the same as adopted in the model. The data on a 1.875°x1.875° latitude/longitude grid was interpolated to the 4°x5° grid points to be compared with the model results. The 31-day time series of data sampled every six hours, includes sea level pressure, geopotential height, and wind at 1000, 850, 700, 500, 400, 300, 250, 200, 150, 100, 70, 50, 30, 20, and 10 mb. Among these variables, the sea level pressure field is the most reliable and is based on a large number of observations, sufficient for use in this study [*Bengtsson et al.*, 1982]. Comparison of simulated and observed results are made for all these variables. However, we will present the results of an analysis by using the sea level pressure field in more detail in the next section.

Since the FGGE IIIb data is made by the analysis-initialization-prediction-cycle, there is a possibility that the tides appeared in the ECMWF FGGE IIIb data are strongly affected or even artificially generated by the ECMWF operational model. Fortunately, there is no possibility in this case (so called main IIIb data), because the ECMWF model that was used to produce FGGE IIIb data had no diurnal cycle. Moreover, the present simulation has no relation to the general circulation of the atmosphere in 1979; the sea surface temperatures are different from each other and the monthly mean variables are also different [see *Tokioka and Yagai*, 1984]. The MRI GCM and the ECMWF forecast model that was used to make FGGE data sets, are two independent models, although they are highly sophisticated and are state-of-the-art models. Therefore, we will restrict ourselves to discussion of the features which are common to "the GCM simulation" and "the FGGE IIIb data analysis". These common features of tides must be inherent in the observed data and must be worth discussing. Since horizontal and vertical structures of nonmigrating modes are not known and 31-day data period used in this study may be rather short to permit discussion of the statistical significance of the results, we will check the reliability of the results by intercomparison and interpretation of "the GCM simulation" and "the data analysis".

4.3 Simulation and Observation

4.3.1. Diurnal variation

To extract tidal modes from a data set sampled in every six hours, a

simple filtering and a Fourier decomposition operations following Tokioka and Yagai [1987] are used in this study. At first, data of the same time of day are averaged over a month and the monthly mean values are subtracted from them. Let us denote such data as a_L, where L is the Greenwich Standard Time and takes values of either 00, 06, 12 or 18. We know that tidal modes include a westward propagating diurnal mode of the zonal wavenumber one (f=-1, m=1), and a westward propagating semidiurnal mode of the zonal wavenumber two (f=-2, m=2). In the present model, an eastward propagating diurnal mode of the zonal wavenumber one (f=1, m=1) is also found. Therefore we introduce the following filtering operator;

$$b_1(a) = \{a_0(i) - a_0(i+36) - a_0(i+18) + a_0(i+54) - a_{12}(i) + a_{12}(i+36) + a_{18}(i+18) - a_{18}(i+54)\}/8 \quad (4.1)$$

$$b_2(a) = \{a_0(i) - a_0(i+18) + a_0(i+36) - a_0(i+54) - a_{06}(i) + a_{06}(i+18) - a_{06}(i+36) + a_{06}(i+54) + a_{12}(i) - a_{12}(i+18) + a_{12}(i+36) - a_{12}(i+54) - a_{18}(i) + a_{18}(i+18) - a_{18}(i+36) + a_{18}(i+54)\}/16 \quad (4.2)$$

$$b_3(a) = \{a_0(i) - a_0(i+36) + a_0(i+18) - a_0(i+54) - a_{12}(i) + a_{12}(i+36) - a_{18}(i+18) + a_{18}(i+54)\}/8 \quad (4.3)$$

$a_L(i)$ indicates the value of a_L at the longitudinal grid point "i". As the longitudinal grid size is 5°, "i" varies from 1 to 72. The response characteristics of b_1 is;

$$R_1(f,m) = (1 - e^{\hat{i}m\pi})(1 - e^{-\hat{i}f\pi})(1 - e^{\hat{i}(m-f)\pi/2})/8 \quad (4.4)$$

where $\hat{i}$ is an imaginary unit. The filter b_1 eliminates (f=-2, m=2) and (f=1, m=1) modes. The response characteristics of b_2 and b_3 are,

$$R_2(f,m) = (1 - e^{\hat{i}m\pi/2})(1 + e^{\hat{i}m\pi})(1 - e^{-\hat{i}f\pi/2})(1 + e^{\hat{i}(m-f)\pi})/16 \quad (4.5)$$

$$R_3(f,m) = (1 - e^{\hat{i}m\pi})(1 - e^{-\hat{i}f\pi})(1 + e^{\hat{i}(m+f)\pi/2})/8 \quad (4.6)$$

The filter b_2 eliminates (f=-1, m=1) and the filter b_3 eliminates (f=-1, m=1) and (f=-2, m=2). The perfect response pairs (f, m) to the filtering b_1, b_2 and b_3 are marked with b_1, b_2 and b_3 in Table 4.1, respectively. For example, $b_1(a)$ includes not only (f=-1, m=1) but also (f=3, m=1), (f=1, m=3), (f=-1, m=5),... Modes with a different zonal wavenumber are separated further by a Fourier decomposition of $b_1(a)$ in the longitudinal direction. The m=1 component of $b_1(a)$, for example, includes all oscillations of f=-1+4n (n=0, ±1, ±2, ...). Each mode can be separated with the help of special data sampled every hour.

Fortunately, we confirmed that the Fourier decomposition of $b_l(a)$ (l=1, 2, 3) in the longitudinal direction is enough, in practice, to isolate a single dominant mode (f, m).

Table 4.1 Perfect response pair of the zonal wavenumber "m" and frequency "f" (day^{-1}) to the filtering operator b_1, b_2 and b_3. The perfect response pair (f, m) to the operator b_i(i= 1, 2, 3) is marked with b_i [Tokioka and Yagai, 1987].

m \ f	−4	−3	−2	−1	0	1	2	3	4
1		b_3		b_1		b_3		b_1	
2			b_2				b_2		
3		b_1		b_3		b_1		b_3	
4									
5		b_3		b_1		b_3		b_1	

Figures 4.2*a* and 4.2*b* show the horizontal map of sea level pressure of the diurnal mode (f=-1, m=1) at 0600 GMT simulated with the MRI GCM-I, together with observations based on the FGGE IIIb (SOP-1) data. The maximum value is 0.8 mb and occurs at 6°S in the simulation, while 0.6 mb occurs at 14°N in the observations. The observed diurnal pressure oscillation by mode (f=-1, m=1) peaks at 0620 LT at low latitude, and the simulated phase lags behind the observation by 40 min. near the equator. (This is small compared to the interval of radiation calculation of one hour in the model.) It is interesting to note that modes with short meridional wavelengths appeared in latitudes near the poles both in the simulation and observations. The maximum value is 0.4 mb and occurs at 75°S in the simulation, which is in good agreement with the observations.

Figures 4.3*a* and 4.3*b* show the same as that of Figure 4.2, but for the semi-diurnal mode (f=-2, m=2). The maximum value is 1.0 mb and occurs at 10°N in the simulation, while 1.2 mb occurs at 6°N in the observations. The observed semi-diurnal pressure oscillation by the

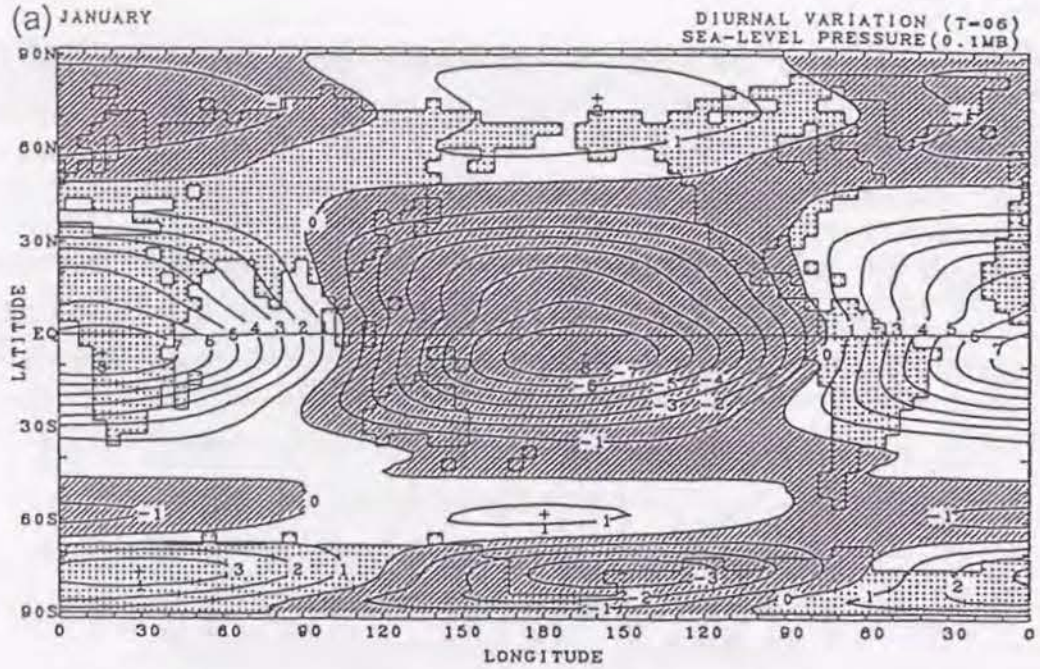

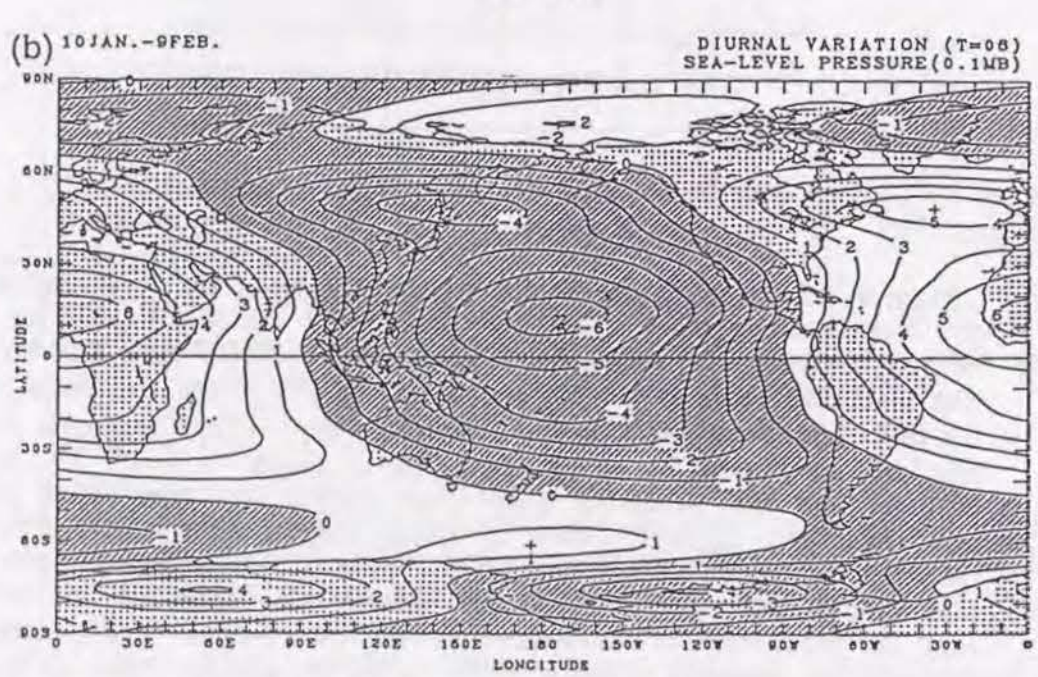

Figure 4.2: The horizontal map of sea level pressure field of the diurnal mode (f=-1, m=1) at 0600 GMT from (a) the GCM simulation and (b) FGGE IIIb(SOP-1) data analysis. The contour interval is 0.1 mb, and negative values are shaded.

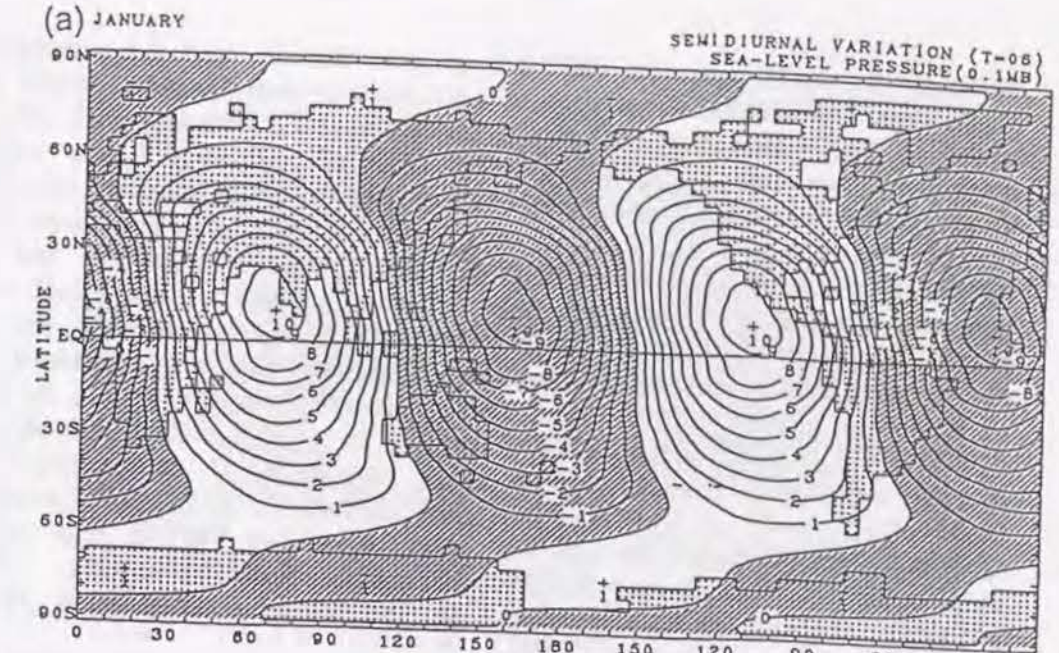

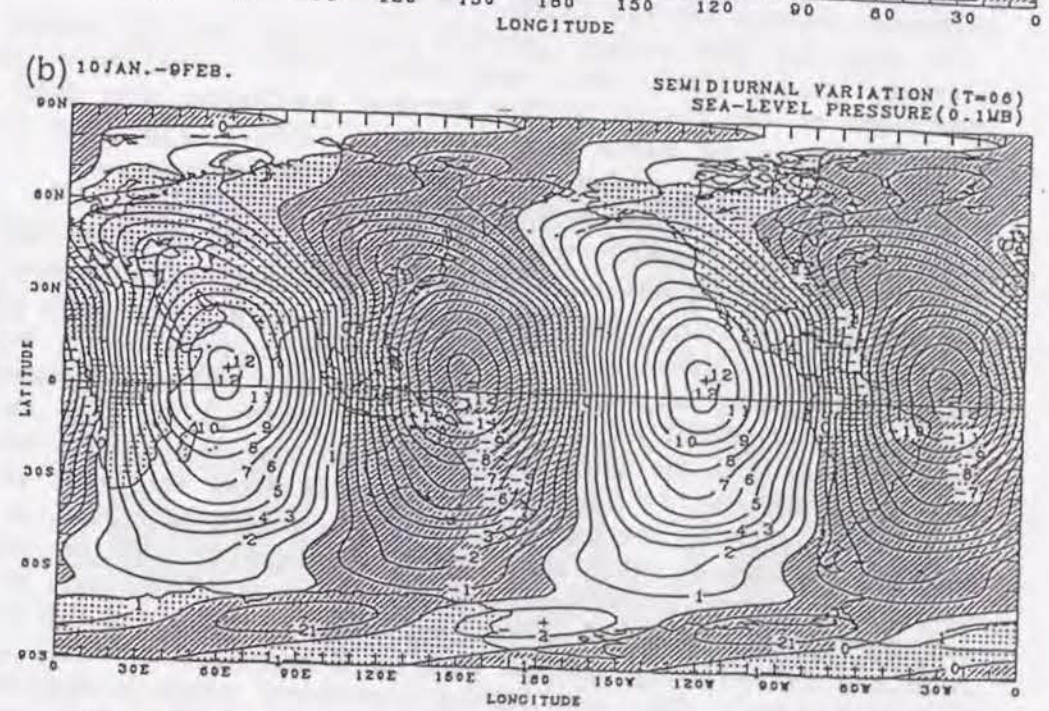

Figure 4.3: The horizontal map of sea level pressure field of the semi-diurnal mode (f=-2, m=2) at 0600 GMT from (a) the GCM simulation and (b) FGGE IIIb(SOP-1) data analysis. The contour interval is 0.1 mb, and negative values are shaded.

mode (f=-2, m=2) peaks at 1000 LT at low latitude, and the simulated phase lags behind the observation by 40 min. at low latitudes which is equal to the value for the mode (f=-1, m=1). Modes with short meridional wavelength also appeared near the poles in this case, although the maximum value in the simulation is much smaller than in the observations. As a result, the model fairly well simulates the migrating modes (f=-1, m=1) and (f=-2, m=2), both in amplitude and in phase in the sea level pressure field. The amplitude of the zonal and annual means of the diurnal surface pressure oscillation is ~0.6 mb at the equator, while that of the semidiurnal surface pressure oscillation is ~1.2 mb [*Haurwitz*, 1956, 1965]; these coincide with the results by the FGGE IIIb data set. The MRI GCM tends to have a large amplitude of the diurnal mode (f=-1, m=1) and a small amplitude of the semidiurnal mode (f=-2, m=2) at low latitudes. In contrast to this, the Canadian Climate Centre model by *Zwiers and Hamilton* [1986] had small amplitudes of diurnal and semidiurnal main migrating modes. The physical process parameterization of the model may cause these differences between the two GCMs.

The observed tidal surface pressure oscillations are due mainly to migrating modes (f=-1, m=1) and (f=-2, m=2). However, large amplitudes of the diurnal surface pressure oscillation over land are known, based on the station data [*Haurwitz*, 1965]. The value of the diurnal variation of a variable a at t_0 GMT is given by

$$b(t_0)=a(t_0)-\{a(t_0)+a(t_0+6)+a(t_0+12)+a(t_0+18)\}/4. \qquad (4.7)$$

where $a(t_0)$ is the monthly mean value averaged for the same time of day. Figures 4.4*a*-4.4*h* show the geographical distribution of $b(t_0)$ for the sea level pressure field at 0000, 0600, 1200, and 1800 GMT, together with the observations. No filtering schemes except 9-point weighted smoothing are used to plot these figures. These are compared with the observational results by *Haurwitz* [1956, 1965] who showed the amplitude and the phase of the diurnal and semi-diurnal surface pressure oscillations. Since data is sampled every six hours in this study, nonmigrating components of the semidiurnal tide are not separated. However, the geographical distribution of the diurnal barometric oscillation is much more irregular than that of the semidiurnal oscillation [*Haurwitz and Cowley*, 1973], and this is also confirmed by an hourly sampled data for a particular two days in the GCM simulation. The semi-diurnal component, which is analyzed in Figure 4.3, is apparent in these figures, and the strong tendency for the value to be larger over land than over ocean is evident in the observations and also in the simulation. Large negative values are seen along the margin of the American continents at 0000 GMT in the

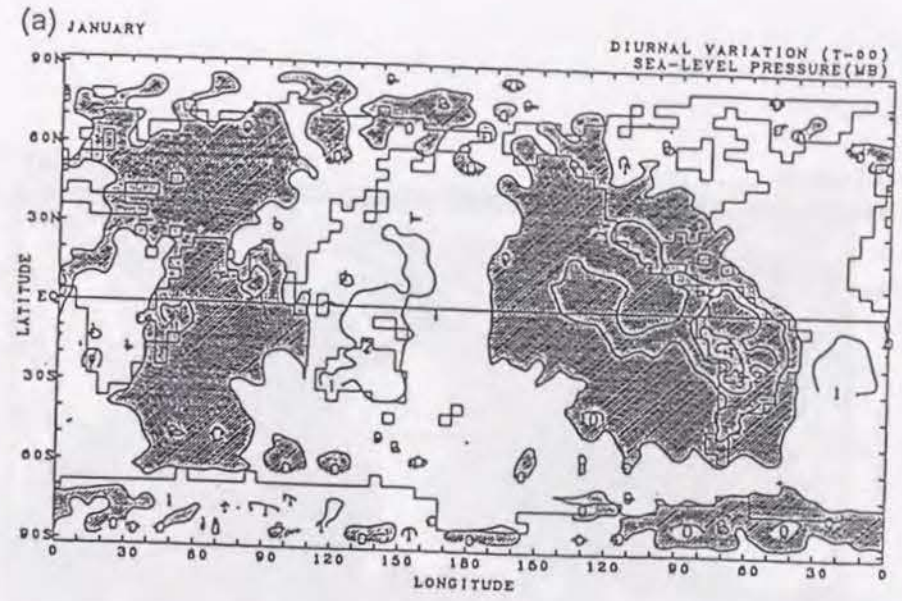

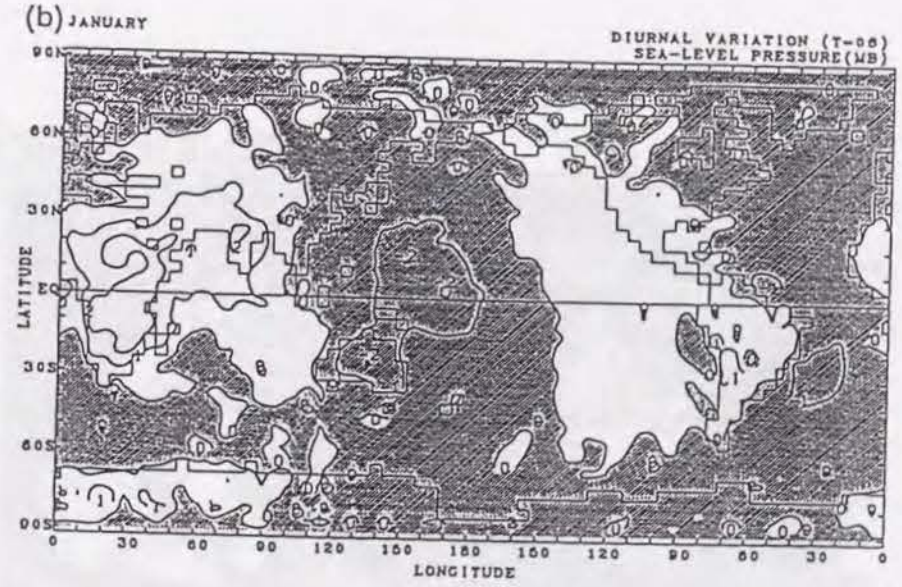

Figure 4.4: Diurnal variation of sea level pressure field at 0000, 0600, 1200, and 1800 GMT from the GCM simulation ((a), (b), (c), and (d)) and FGGE IIIb(SOP-1) data analysis ((e), (f), (g), and (h)). The contour interval is 1.0 mb, and negative values are shaded.

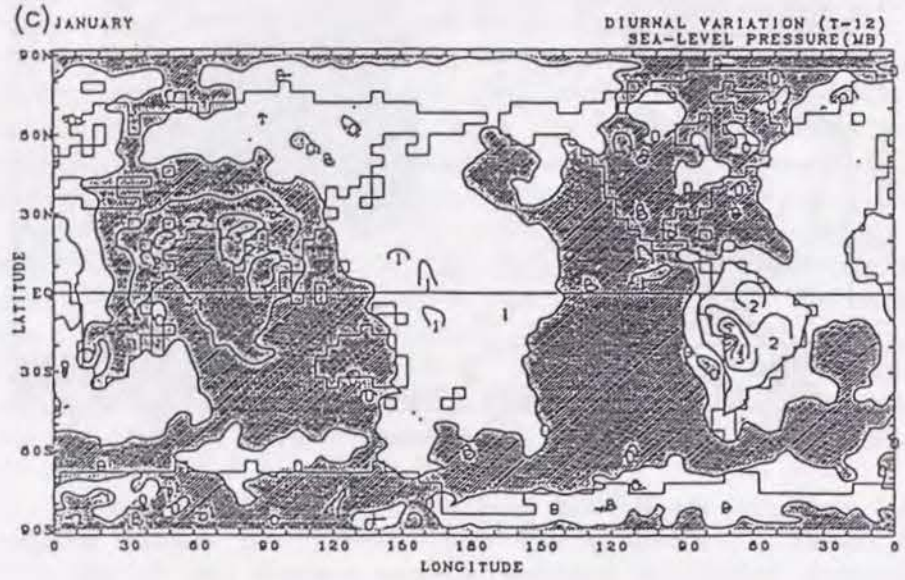

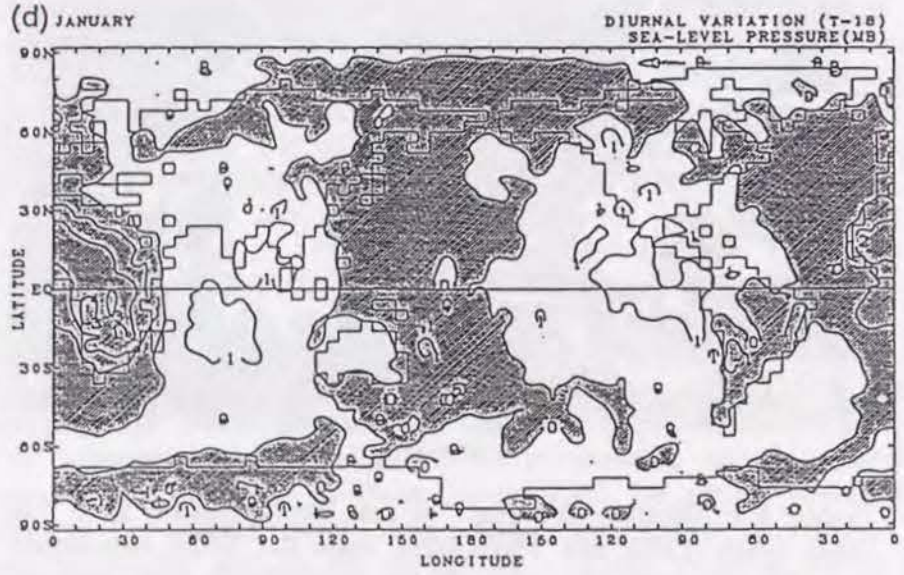

Figure 4.4 (cont.)

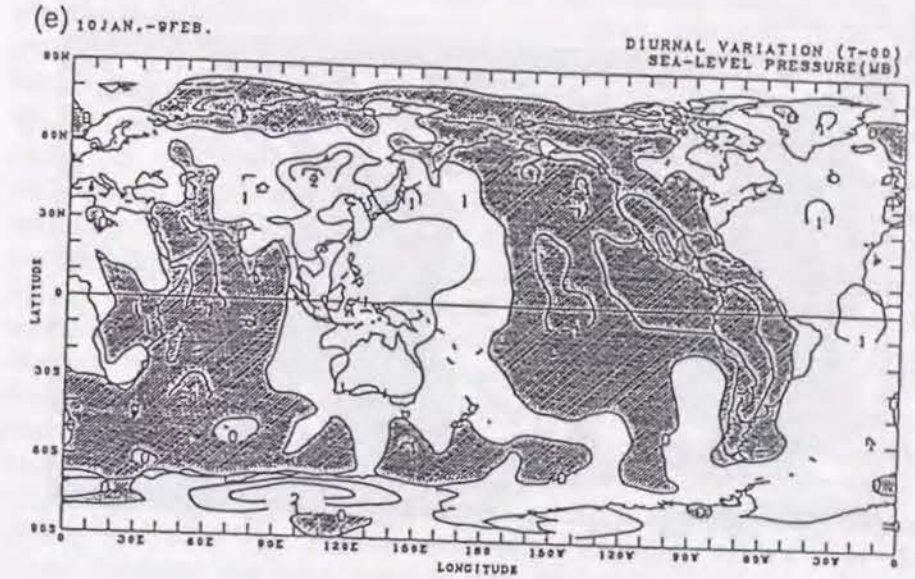

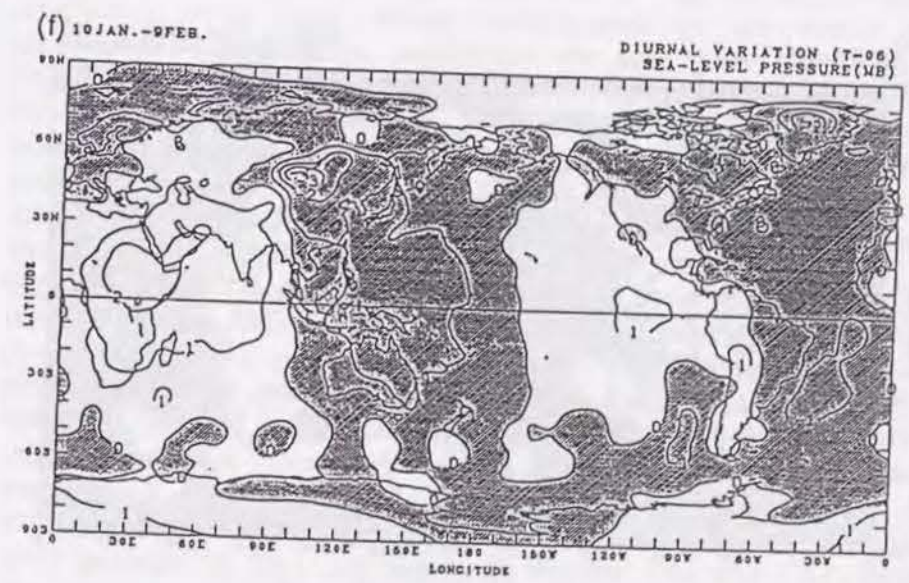

Figure 4.4 (cont.)

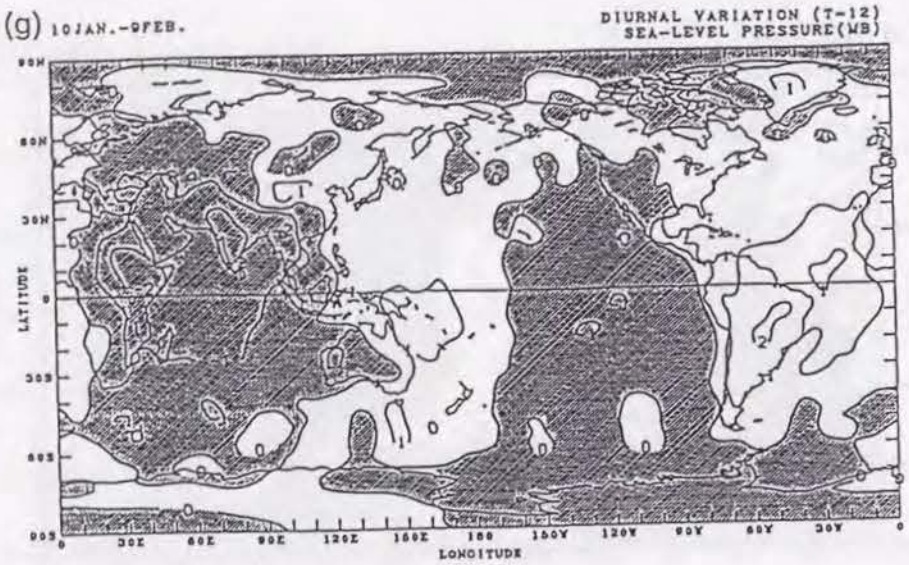

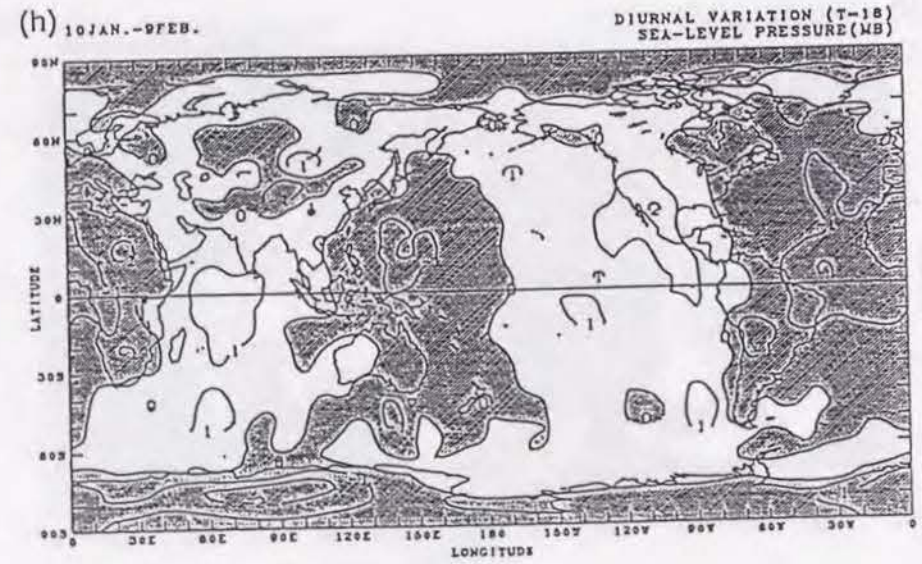

Figure 4.4 (cont.)

simulation and observations, but the absolute value of 4 mb in the simulation over the Andes is about three times as large as that in the observations. This large discrepancy is sometimes seen at high mountain areas and may be due to the vertical extrapolation procedure, which is used to calculate the sea level pressure from the surface pressure and the temperature. Note that the MRI GCM and the ECMWF forecast model adopt σ-coordinate system and the surface pressure, not the sea level pressure, is a prognostic variable. The lack of a diurnal cycle in the forecast model may reduce the amplitudes of diurnal variation at high mountain areas in the FGGE data, since forecast values which are used as first-guess values may be corrected little in the poorly observed area. At 0600 GMT in the simulation, large positive values are seen over the African continent and the Arabian Peninsula, which corresponds to the observations. These local maxima and minima do not move in synchrony with the sun; some of them move faster than the sun and others move in a direction opposite to the sun. For example, large negative values are seen over the Rockies and the Andes at 0000 GMT in the observations. At 1200 GMT, large positive values are seen only over the Andes. Then at 1800 GMT, large positive values are over the Rockies and large negative values over the Andes. These features are also seen in the simulation, and the absolute values in the simulation are again larger than those observed. *Zwiers and Hamilton* [1986] simulated diurnal and semi-diurnal tidal modes with the GCM and showed a large amplitude of the diurnal surface pressure oscillation over land, which corresponds to the result mentioned previously. These large amplitudes are seen over the south America, Australia , and Africa at low latitudes. Wavenumber 4 of topography is produced by these continents. Therefore clear peaks of nonmigrating modes (f=-1, m=5) and (f=1, m=3) will be seen in their simulation if they make such analysis. Figures 4.5*a* and 4.5*b* show the power spectra of sea level pressure in the space-time domain at 2°S together with the observations. As the analysis is based on data sampled every six hours, high frequency modes over |f|=2 are not covered. Three peaks are commonly seen between the simulation and observations at |f|=1, that is, (f=-1, m=1), (f=-1, m=5) and (f=1, m=3). TY87 found these peaks in the power spectra of the heating rate in the space time domain at 2°S, 700 mb, and 5.18 mb, respectively. They also confirmed these peaks by the analysis of the simulation data, sampled once every hour for a particular 2 days [see TY87, Figures 2 and 3]. To see the latitudinal distributions of power spectra, the wavenumber-latitude sections of sea level pressure at |f|=1 are shown in Figures 4.6*a* and 4.6*b* together with the simulation. The (f=-1, m=1) mode is the largest in almost all latitudes in the simulation and observations of which the horizontal

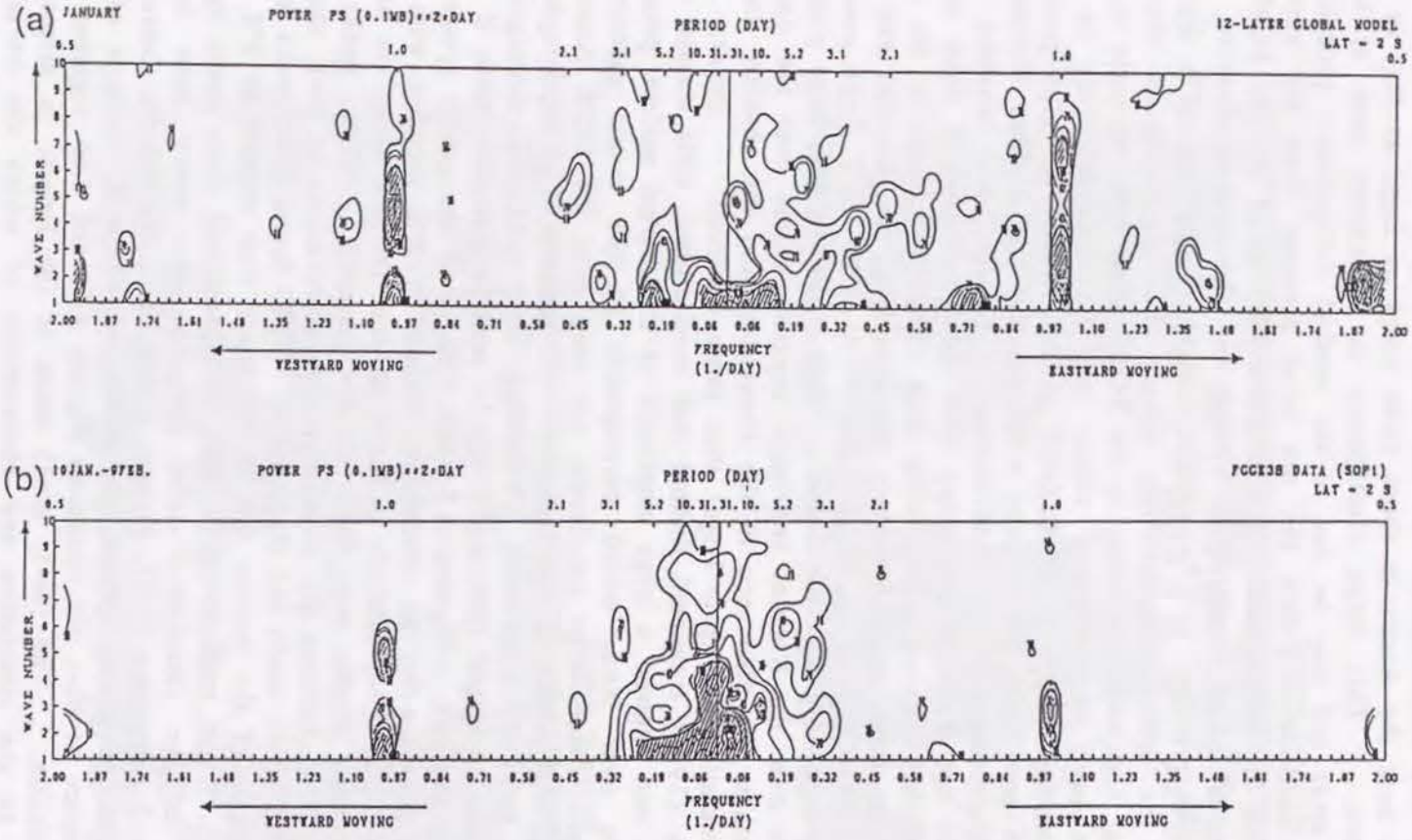

Figure 4.5: The power spectra of the sea level pressure field in the space-time domain at 2°S from (a) the GCM simulation and (b) FGGE IIIb(SOP-1) data analysis. The contours are 10, 20, 40, 80, 100, 200, 400, 800, and 1000 (0.1 mb)^2 day^{-1}. Values larger than 100 are shaded.

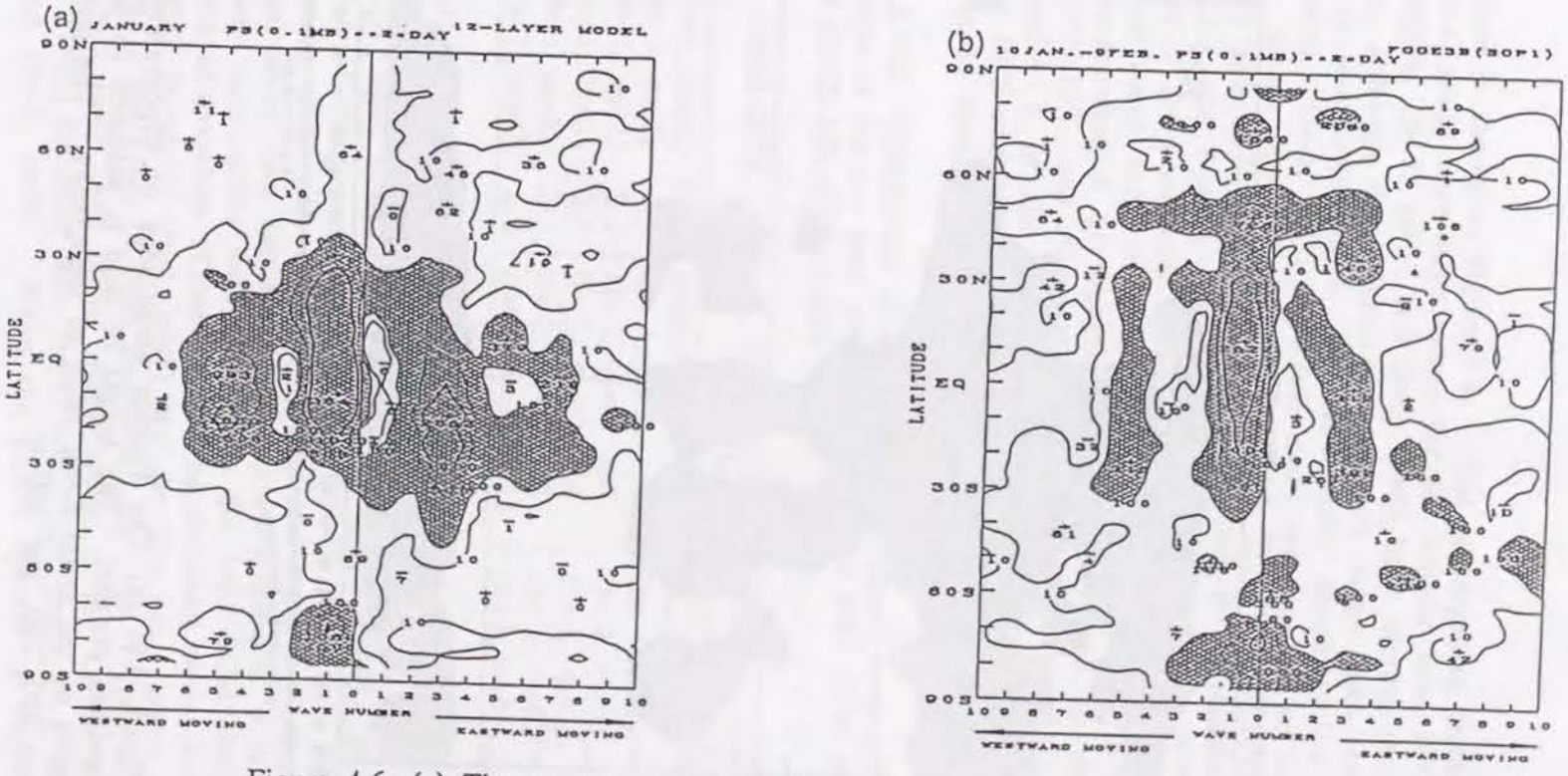

Figure 4.6: (a) The power spectra of the sea level pressure field in the latitude-wavenumber domain from the GCM simulation. The contours are 10, 100, 500, and 1000 (0.1 mb)^2 day^{-1}. Values larger than 100 are shaded. (b) Same as Figure 4.6(a) except for FGGE IIIb(SOP-1) data analysis.

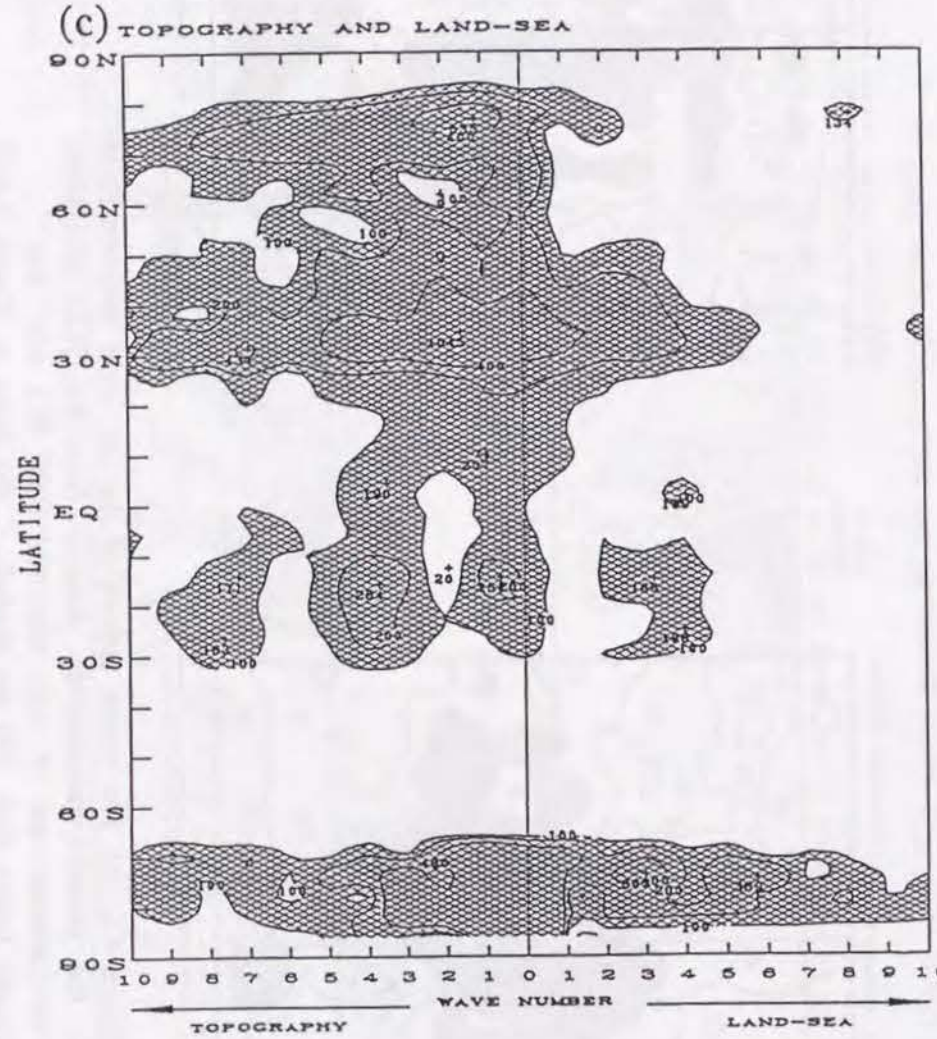

Figure 4.6: (c) The Fourier amplitudes of topography and land-sea contrast. The height of land is assumed to be the same as the zonal mean value of topography. The contours are 100, 200, and 400 m.

structure is shown in Figure 4.2. The nonmigrating mode (f=-1, m=5) and (f=1, m=3) have large values for the latitude band 10°N-30°S. In this region, (f=-1, m=5) and (f=1, m=3) have almost the same power spectra, although the simulated values are larger than those observed. This is consistent with the theoretical consideration (see TY87 Appendix); (f=-1, m=5) and (f=1, m=3) are expected to have the same power, since they are generated by the zonal wavenumber 4 of the land-sea distribution (or topography). To see the latitudinal distribution of forcing, the Fourier amplitude of topography in the zonal direction, and that of flat continents, of which height is assumed to be the same as the zonal mean value of actual topography, are shown in Figure 4.6*c*. The wavenumber 4 of topography has large values for the latitudinal band 10°N-30°S, and the maximum is positioned near 18°S, whereas the wavenumber 4 of flat continents (land-sea contrast) has large values between 10°S and 30°S. This corresponds to the size of the Australian continent in latitude.

TABLE 4.2. Comparison of the order of the global mean power spectra of the sea level pressure field in the MRI GCM simulation and FGGE IIIb (SOP-1) data analysis.

	MRI GCM	FGGE IIIb	Haurwitz and Cowley [1973]
1	(f=-1, m=1) 11.6	(f=-1, m=1) 9.5	(f=-1, m=1)
2	(f= 1, m=3) 4.7	(f= 1, m=3) 1.7	(f= 1, m=1)
3	(f=-1, m=2) 2.6	(f= 1, m=0) 1.4	(f= 1, m=3)
4	(f=-1, m=5) 2.6	(f=-1, m=5) 1.4	(f=-1, m=2)
5	(f= 1, m=2) 2.3	(f=-1, m=2) 1.3	(f= 1, m=0)
6	(f=-1, m=4) 1.6	(f= 1, m=1) 0.86	(f=-1, m=5)

Haurwitz and Cowley [1973] values are amplitudes.

Haurwitz and Cowley [1973, Figure 2] calculated "global" mean amplitudes of component waves of the surface pressure. Although the present study deals with the January case and their result was based on the annual mean data between 60°N and 60°S latitude, it is interesting to compare their results with those from the MRI GCM simulation and FGGE IIIb observations (Table 4.2). The dominant wave that Haurwitz and Cowley found, is (f=-1, m=1) and the five next largest component waves are, in the order of their amplitudes, (f=1, m=1), (f=1, m=3), (f=-1, m=2), (f=-1, m=0), and (f=-1, m=5), while in the earlier analysis by *Haurwitz* [1965] the order was (f=-1, m=2), (f=1, m=1), (f=1, m=3), (f=-1, m=3), and (f=-1, m=5). When the power spectra in Figure 4.6 are

averaged on a global basis, (f=-1, m=1) is also dominant in the present case. The four next largest components are (f=1, m=3), (f=-1, m=2), (f=-1, m=5), and (f=1, m=2) in the MRI GCM, and (f=1, m=3), (f=1, m=0), (f=-1, m=5), and (f=-1, m=2) in the FGGE IIIb data. The global mean power spectral of (f=1, m=3) in the GCM is rather larger than that of other component waves. The others are almost comparable in the GCM simulation and in the FGGE IIIb data analysis, although values are systematically larger in the simulation than in the data analysis. The disagreements in the order of the amplitudes will have to be clarified in the future study in connection with seasonal and year-to-year variations of tidal waves. For example, *Meisner and Arkin* [1987] analyzed diurnal variations of convective precipitation from the geostationary satellite data, and they found fluctuations occurred during the 1982-83 ENSO event. As a result, the present study almost supports the "global" mean amplitudes of component tidal waves by Haurwitz and Cowley.

4.3.2. Nonmigrating diurnal tide (f=-1, m=5)

The horizontal map of sea level pressure of the mode (f=-1, m=5) at 0600 GMT is shown in Figure 4.7 together with the observations. There is good agreement between the simulation and observations for the latitude band 60°N-50°S, where the power spectra have relatively large values. The maximum value is 0.4 mb in the simulation and 0.2 mb in the observations. Both of the maxima occur at around 20°S. Simulated and observed phases have common characteristic features with latitude; they have almost no phase tilt for the latitude band 0-40°S, while they have a southeast to northwest tilt for the latitude band 0-30°N, and a southwest to northeast tilt for the latitude band 30°N-50°N. As was pointed out in TY87, these features are also seen in the horizontal distribution of the zonal wavenumber 4 of topography shown in Figure 4.8. It is interesting to note that the phase tilt for the latitude band 40°S-30°N is also seen in Figures. 4.4*a* and 4.4*e* where large negative values are distributed along the margin of the American continents at 1200 GMT in the diurnal variation of sea level pressure field.

Figures 4.9*a* and 4.9*b* show the horizontal map of wind and geopotential field of (f=-1, m=5) at 0600 GMT and 900 mb, the lowest model level, together with the observation at 1000 mb. The same features in the phase are seen for the latitude band 40°S-30°N between the simulation and observations, although amplitudes of the wind and the geopotential are systematically larger in the simulation. The motion is intensified in the subtropics of the southern hemisphere, with

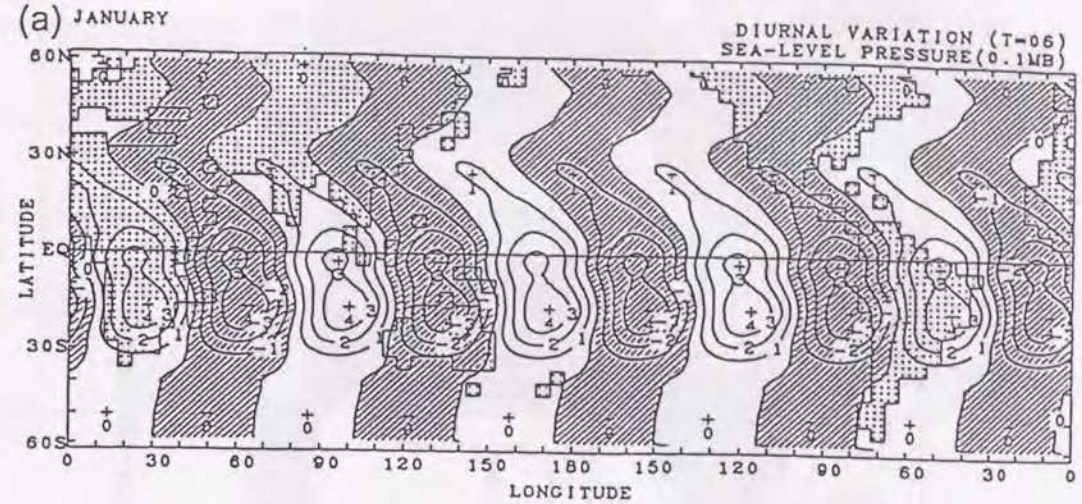

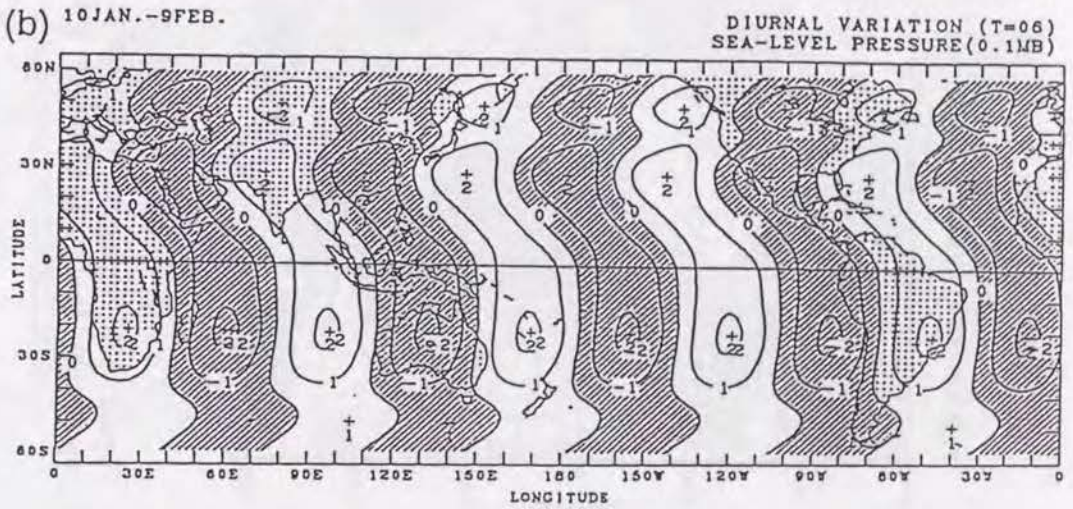

Figure 4.7: The horizontal map of sea level pressure field of the diurnal mode (f=-1, m=5) at 0600 GMT from (a) the GCM simulation and (b) FGGE IIIb(SOP-1) data analysis. The contour interval is 0.1 mb, and negative values are shaded.

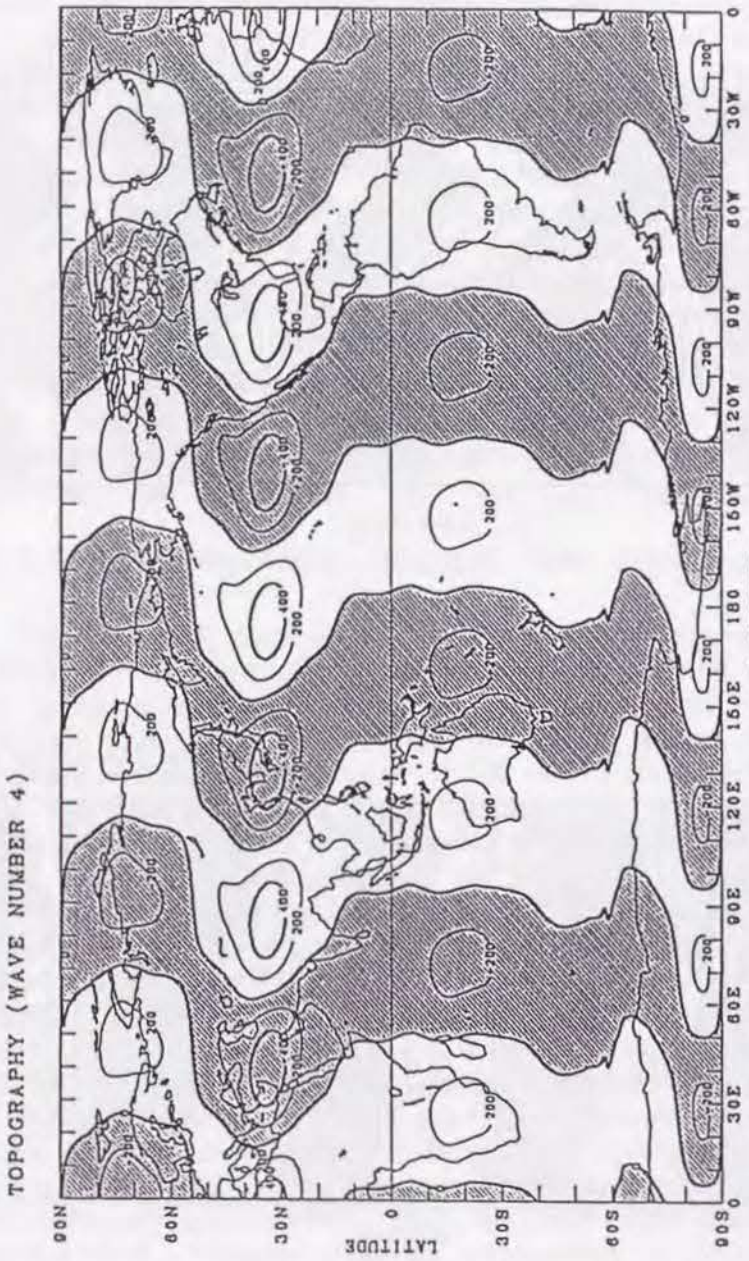

Figure 4.8: Horizontal distribution of the zonal wavenumber 4 of topography (unit: m) [Tokioka and Yagai, 1987].

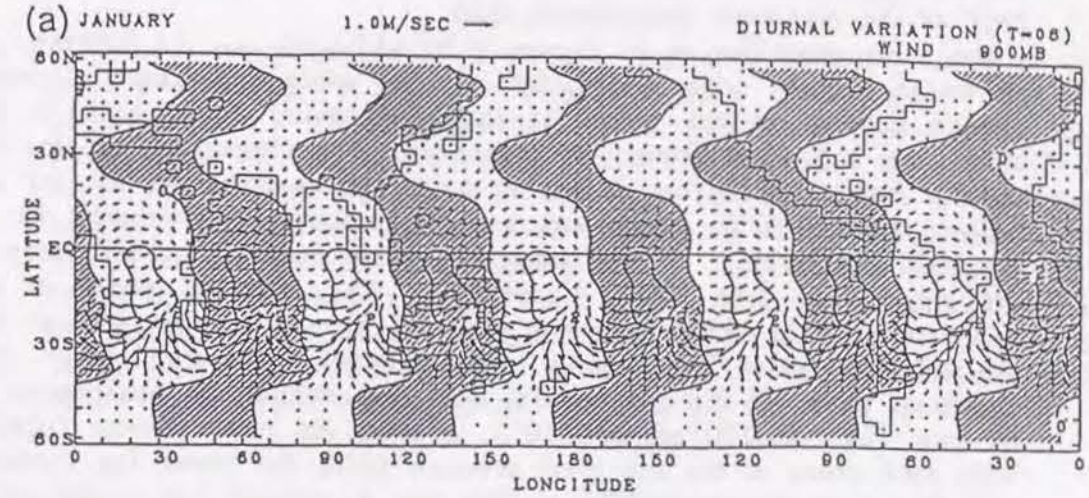

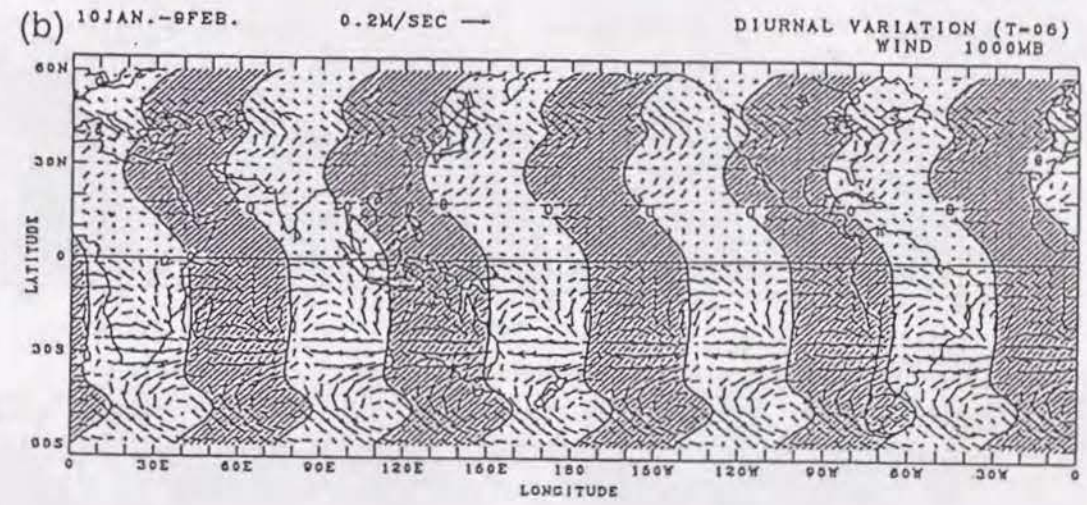

Figure 4.9: The horizontal map of wind and geopotential field of the mode (f=-1, m=5) at 0600 GMT from (a) the GCM simulation at the 900 mb level and (b) FGGE IIIb(SOP-1) data at the 1000 mb level. The contour interval of geopotential is 2.0 m, and negative values are shaded.

the convergence in the direction of movement and the divergence at the back of the maximum geopotential field.

The same quantities as in Figures 4.9*a* and 4.9*b*, but for 300 mb, are shown in Figures 4.10*a* and 4.10*b* In the upper troposphere a notable change appears in the phase of the geopotential field, both in the simulation and observations; the phase still has almost no tilt for the latitude band 0-30°S, but it has a southwest to northeast tilt for the latitude band 0-30°N, which contrasts to southeast to northwest tilt at the 1000 mb level. In the simulation, these features are also seen in the stratosphere (see TY87 Figure 19). The observed phase of the geopotential field shifts eastward with height and reaches 23° at 300 mb and 10°S, which is commonly seen but larger in the simulation. The simulated phase of the geopotential field lags behind the observation by 60 min. (15°) at 300 mb and 10°S, whereas the phase almost coincide with each other in the sea level pressure field; the phase lag increases with height in the troposphere. This may be mainly due to the coarse vertical resolution of the model. In the wind field, there is a correspondence between the simulation and observations only for the latitude band 0-20°S, but the amplitude is again much larger in the simulation.

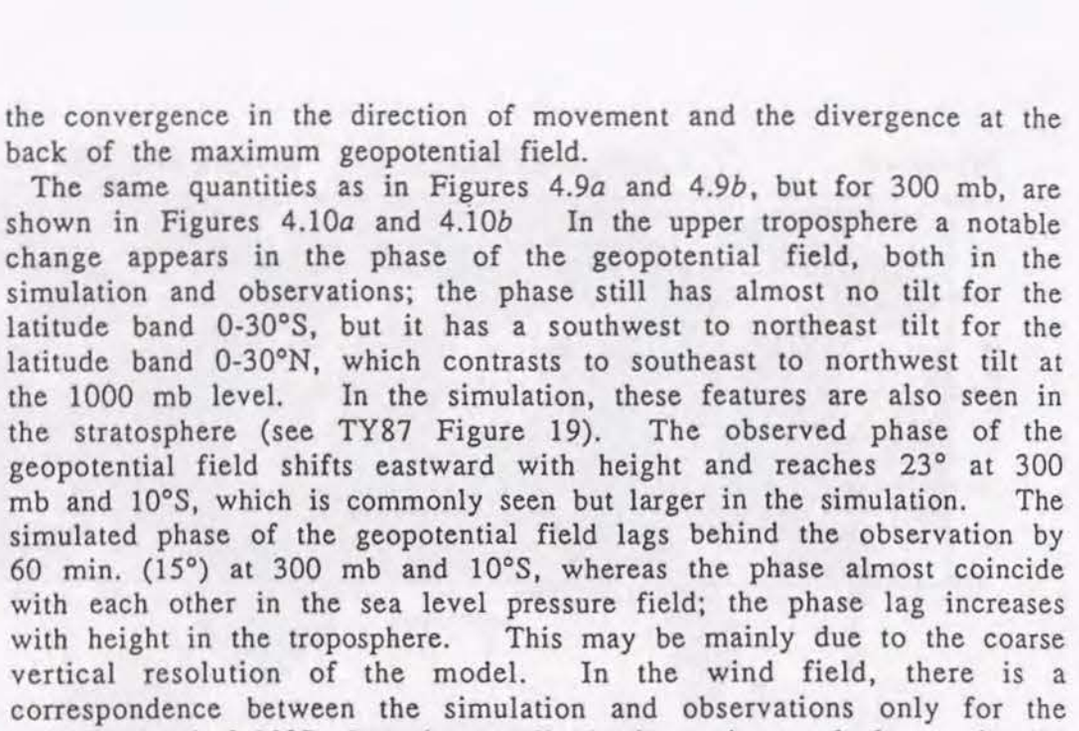

Figure 4.10: The same as in Fig.4.9 but at the 300 mb level.

4.3.3. Nonmigrating diurnal tide (f=1, m=3)

Figures 4.11*a* and 4.11*b* show the simulated horizontal map of sea level pressure of the mode (f=1, m=3) at 0600 GMT together with the observations. The simulation is in good agreement with the observations for the latitude band 40°S-10°N, whereas the mode (f=-1, m=5) has a correspondence between the simulation and observations within a much wider region. The maximum value is 0.5 mb in the simulation and 0.2 mb in the observations. Two maxima occur, at 22°S and 2°S, in the observation, while a single maximum occurs at 18°S in the simulation. The phase lags behind the observation by 40 min. at 20°S, which is almost the same as that for the migrating mode (f=-1, m=1) but is large when compared with that for the mode (f=-1, m=5).

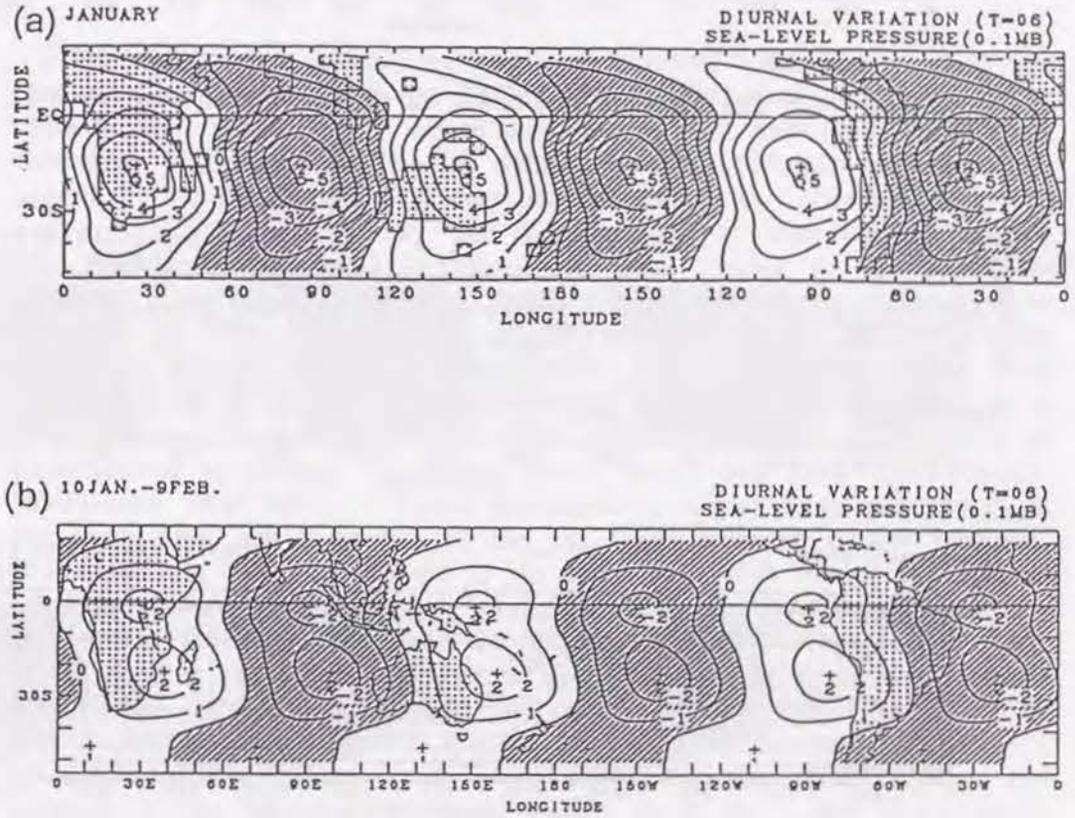

Figure 4.11: The same as in Fig.4.7 but for the mode (f=1, m=3).

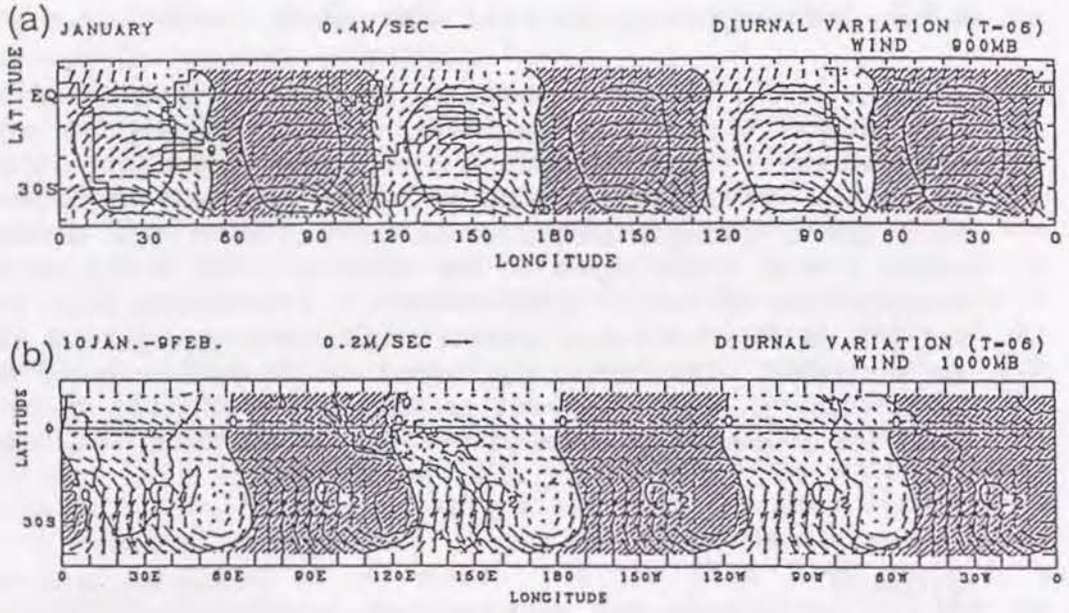

Figure 4.12: The same as in Fig.4.9 but for the mode (f=1, m=3).

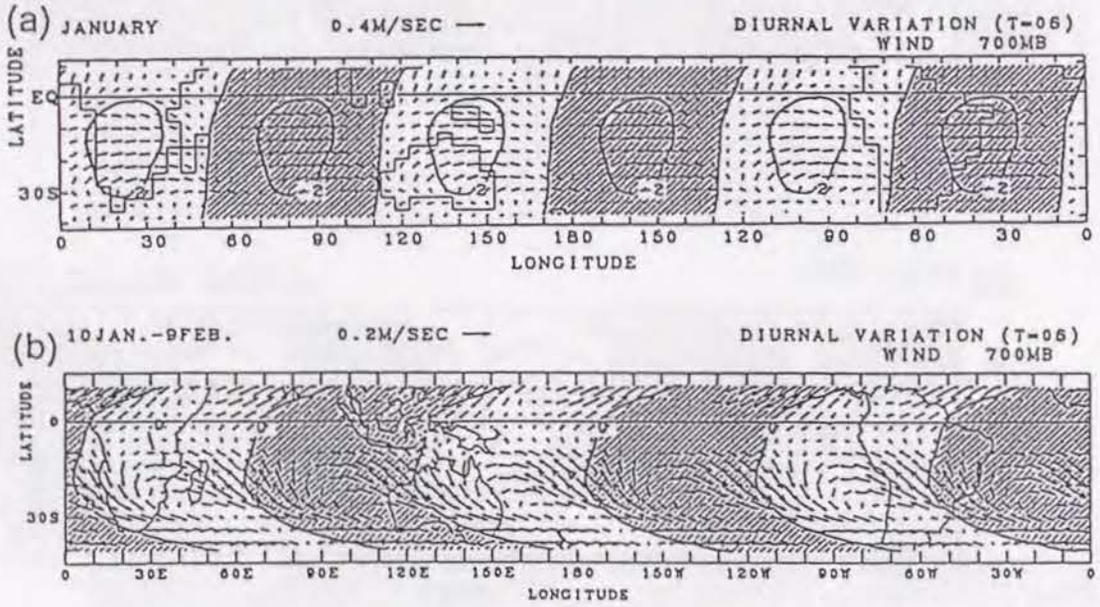

Figure 4.13: The same as in Fig.4.9 but for the mode (f=1, m=3) at the 700 mb level.

Figures 4.12*a* and 4.12*b* show the horizontal map of wind and geopotential field of (f=1, m=3) at 0600 GMT and 900 mb, the lowest model level, together with the observations at 1000 mb. A correspondence between the simulation and the observations is seen only for the latitude band 0-30°S in the geopotential field. The wind field of the FGGE IIIb (SOP-1) data at low latitudes seems to have quality problems. At upper levels we could find a correspondence only below the 700 mb level in the geopotential field (Figures 4.13*a* and 4.13*b*). Again, the amplitude of the geopotential is larger in the simulation than in the observations, and the wind field of the FGGE IIIb data is not good. This indicates that further analyses with improved observational data are needed in the wind field and also in the stratosphere with other variables. The phase lags behind the observation by 40 min., while the simulated and observed phase changes little with height.

4.4 Concluding Remarks

From the present results, nonmigrating thermal tides (f=-1, m=5) and (f=1, m=3) are detected in the FGGE IIIb (SOP-1) data and in the GCM simulation. The ECMWF operational model that had no diurnal cycle was used to produce FGGE IIIb data. Therefore, diurnal variations that appear in the FGGE IIIb data sets are inherent in the observed data, and not artificially generated by the four-dimensional assimilation process. The simulated horizontal structures of these modes in the sea level pressure field bear a striking similarity to the observations at low latitudes. This convinced us of the accuracy of the GCM and the analytical method adopted in this study, since the observed sea level pressure field is the most reliable among variables and is based on a large number of observations. Even at low latitudes, the number of observations is enough to resolve (f=-1, m=5) and (f=1, m=3) modes [*Bengtsson et.al* 1982]. These nonmigrating modes have clear peaks in the space-time power spectra of the sea level pressure at low latitudes. The maximum value of 0.2 mb is the same with both modes as expected from the theory, while the maximum value of the semidiurnal mode (f=-2, m=2) is 1.2 mb and that of the diurnal mode (f=-1, m=1) is 0.6 mb. These modes are closely related to the wavenumber 4 of the land-sea distribution (or topography) and are essentially the same that *Tokioka and Yagai* [1987] reported in the analysis of GCM simulation in January. In addition, the model fairly well simulated the phase, shape and strength of the background diurnal modes (f=-2, m=2) and (f=-1, m=1), in the sea level pressure field.

At the upper level of 300 mb, observed and simulated (f=-1, m=5) modes in the geopotential field have a phase shift for the latitude band 0-30°N with the height. The phase has a southeast to northwest tilt at 1000 mb while it has a southwest to northeast tilt at 300 mb. Conversely, no phase shift with height is apparent for the latitude band 0-30°S below the 300 mb level, where the phase axis is almost parallel to the longitudinal circle. For the mode (f=1, m=3) the simulation is in good agreement with the observations for the latitude band 40°S-10°N in the sea level pressure field, but a correspondence between the simulation and observations in the geopotential field is seen only below the 700 mb level for the latitude band 0-30°S. The wind field for the FGGE IIIb data produced by the ECMWF (not the final FGGE Level IIIb data set which became available in 1987) has quality problems so that the observed results for the wind field have to be reexamined with improved data set. On the other hand, the GCM wind field is consistent with the geopotential field.

The present study almost supports the result by *Haurwitz and Cowley* [1973], who calculated the "global" and annual mean amplitudes of component tidal waves in the surface pressure field. Further studies are needed to clarify seasonal and annual variations of tidal waves. Finally, nonmigrating thermal tides in the stratosphere will be detected in future, since the GCM used in this study simulated such modes (see Tokioka and Yagai, 1987).

Chapter 5

Summary and conclusions

An atmospheric general circulation model has been developed at the Meteorological Research Institute (MRI GCM) to simulate climate of the earth's atmosphere and study climatic variations. This thesis is concerned with the general circulation model and its application to the study of atmospheric thermal tides.

In chapter 1, general introduction is presented to describe the characteristics of the atmospheric general circulation and its modeling. The observational features of the general circulation of the atmosphere, especially the zonally averaged circulations and ozone distributions are discussed. Basic equations for modeling of the general circulation of the atmosphere are described with the physical process parameterizations. A short review of thermal tides of the atmosphere are also presented. Tokioka and Yagai [1987] analyzed the result of the GCM simulation in January and found detailed structure in the thermal forcings of diurnal and semidiurnal modes within the planetary boundary layer (PBL), which are not seen in the model by Forbes [1982a,b].

In chapter 2, the Meteorological Research Institute general circulation model (MRI GCM) is described, which is based on the University of California at Los Angels (UCLA) model, described by Arakawa and Mintz [1974] and Arakawa and Lamb [1977]. The MRI GCM has twelve vertical layers with the top level at 1 mb, and a horizontal resolution of 5° in longitude by 4° in latitude. Ozone photochemical process in the stratosphere and radiative process which includes the heating by incoming shortwave solar radiation and the cooling by infrared longwave radiation, are described in detail; ozone distribution in the stratosphere as well as water vapor in the troposphere and resulted radiative forcings are essential to the thermal tides in the atmosphere.

In chapter 3, the hardware and software of the supercomputer system installed in the Meteorological Research Institute are described. The supercomputer S-810/10 has several characteristics to realize high performances in hardware and software systems: parallel pipeline processing and a high level of vectorization for programs. The performance of the MRI GCM is also discussed in this chapter with emphasizing the effect of gravity wave drag. Without the gravity wave drag, had serious westerly biases; the westerly jet in the stratosphere is

too strong, the Aleutian low in the troposphere too deep, and no stratospheric sudden warmings appear in winter. The deficiencies are almost overcome by incorporating gravity wave drag which has pronounced effects on the circulations in the northern hemisphere. Since the model has its limitation, especially relating to the sub-grid scale topography, we made a model improvement trial by increasing surface drag coefficients in the tropospheric version of the MRI GCM (Yagai and Tokioka, 1987). As a result, several model shortcomings are refined: weakening of the too strong anticyclonic flow around the Tibetan Plateau at low levels, reduction of excessive evaporation over the Bay of Bengal, reduction of precipitation over the western part of Asia and over the equatorial Indian Ocean and increase of precipitation over the maritime continent.

In chapter 4, observed and simulated nonmigrating diurnal tides are presented. Non-migrating thermal tides, which do not move in synchrony with the sun, are detected in the analyses of FGGE (First GARP Global Experiment) Level IIIb data during the special observation period (SOP-1) of 10 January-9 February 1979. First is the westward moving diurnal mode with the zonal wavenumber 5, and the second a eastward moving diurnal mode with the zonal wavenumber 3. These modes are closely related to the wavenumber 4 of topography at low latitudes and have clear peaks in the space-time power spectra in the sea level pressure field. A maximum value of 0.2 mb is the same with both modes as expected from the theory, while maximum values of the background diurnal and semi-diurnal migrating modes are 0.6 mb and 1.2 mb, respectively. These non-migrating modes are essentially the same that *Tokioka and Yagai* [1987] reported in their analysis of GCM simulation in January.

By comparing FGGE IIIb data analysis and the GCM simulation, diurnal and semi-diurnal migrating modes are simulated well in the sea level pressure field and relatively well at the lower troposphere in the geopotential field. The simulated non-migrating modes have horizontal structures similar to those observed in the sea level pressure field which is the most reliable data and based on a large enough number of observations to detect these modes. In the geopotential field, horizontal structure of the non-migrating modes is identified in the troposphere at low latitudes by simulation and observation. The wind data is also analyzed but the correspondence between the simulation and observation is found only at the lowest level of westward moving wavenumber 5 mode. The present study almost supports the result by *Haurwitz and Cowley* [1973] who calculated the "global" and annual mean amplitudes of component tidal waves in the surface pressure field.

In the thesis, nonmigrating diurnal tides in the stratosphere are not discussed. The FGGE IIIb data has a quality problem in the stratosphere where the number of observation is relatively small, and the vertical resolution of the current model is not enough to simulate propagation of nonmigrating tides. Further studies are needed to clarify nonmigrating thermal tides in the stratosphere, seasonal and annual variations of tidal waves.

REFERENCES

Ackerman, M., Ultraviolet solar radiation related to mesospheric processes, *Mesospheric Models and Related Experiments*, Ed. G. Fiocco, Reidel, Dordrecht-Holland, 149-159, 1971.

Arakawa, A. and V. Lamb, Computational design of the basic dynamical processes of the UCLA general circulation model. *Methods in Computational Physics, Advances in Research and Application*, Vol. 17: *General circulation models of the atmosphere, Academic Press, Inc.*, 337 pp, 1977.

Arakawa, A. and Y. Mintz, The UCLA atmospheric general circulation model. Notes distributed at the workshop 25 March-4 April 1974, Dep. of Meteorology, University of California Los Angeles, 404 pp, 1974.

Bengtsson, L., Kanamitsu, M., Kallberg, P. and Uppala, S., FGGE 4-dimensional data assimilation at ECMWF. *Bull. Am. Met. Soc.* 63, 29-43, 1982.

Cess, R.D., G.L. Potter, J.P. Blanchet, G.J. Boer, S.J. Ghan, J.T. Kiehl, H.Le Treut, Z.-X. Li, X-Z. Liang, J.F.B. Mitchell, J.-J Morcrette, D.A. Randall, M.R. Riches, E. Roeckner, U. Schlese, A. Slingo, K.E. Taylor, W.M. Washington, R.T. Wetherald, and I. Yagai, : Interpretation of cloud-climate feedback as produced by 14 Atmospheric General Circulation Models. *Science*, 245, 513-516, 1989.

Cess, R.D., G.L. Potter, J.P. Blanchet, G.J. Boer, A.D. Del Genio, M. Déqué, V. Dymnikov, V. Galin, W.L. Gates, S.J. Ghan, J.T. Kiehl, A.A. Lacis, H.Le. Treut, Z.-X. Li, X.-Z. Liang, B.J. McAvaney, V.P. Meleshko, J.F.B. Mitchell, J.-J. Morcrette, D.A. Randall, L. Rikus, E. Roeckner, J.F. Royer, U. Schlese, D.A. Sheinin, A. Slingo, A.P. Sokolov, K.E. Taylor, W.M. Washington, R.T. Wetherald, I. Yagai, M.-H . Zhang, : Intercomparison and Interpretation of climate feedback processes in nineteen atmospheric general circulation models. *J. Geophys. Res.*, 95, 16601-16615, 1990.

Chapman, S. and R. S. Lindzen, *Atmospheric tides*, 200 pp, Reidel, Dordrecht-Holland, 1970.

Charney, J. G., Fjörtoft and J. von Neuman, Numerical integration of the barotropic vorticity equation. Tellus., 2, 237-254, 1950.

Charney, J. G., On the scale of atmospheric motions. *Geofys. Publikasjoner*, 17, 17 pp, 1948.

CIAP, T*he Natural Stratosphere of 1974, CIAP Monograph 1*. Ed. A. J. Grobecker, Department of Transportation, Climatic Impact Assessment Program, Washington, D.C., 1199 pp, 1974.

Coulson, K. L., Radiative flux from the top of a Rayleigh atmosphere, Ph.D. Thesis, Dep. of Meteorology, University of California Los Angeles, 176 pp, 1959.

Cunnold, D., F. Alyea, N. Phillips and R. Prinn, A three dimensional dynamical chemical model of atmospheric ozone. *J. Atmos. Sci.*, 32, 170-194, 1975.

Deardorff, J. W., Parameterization of the planetary boundary layer for use in general circulation models. *Mon. Wea. Rev.*, 100, 93-106, 1972.

Dickinson, R. E., Method of parameterization for infrared cooling between the altitudes of 30 and 70 kilometers. *J. Geophys. Res.*, 78, 4451-4457, 1973.

Elsasser, W.M., Atmospheric radiation tables, *Meteorological Monographs*, vol. 4, No. 23, American Meteorological Society, Boston, 43 pp, 1960.

Forbes, J. M., Atmospheric tides 1. Model description and results for the solar diurnal component. *J. Geophys. Res.*, 87, 5222-5240, 1982a.

Forbes, J. M., Atmospheric tides 2. The solar and lunar semidiurnal components. *J. Geophys. Res.*, 87, 5241-5252, 1982b.

Forbes, J. M., and H.B. Garrett, Theoretical studies of atmospheric tides. *Reviews of Geophysics and Space physics*, 17, NO. 8,1951-1981,

Forbes, J. M., and G.V. Groves Diurnal propagating tides in the low-latitude middle atmosphere. *J. Atmos. Terr. Phys.*, 49,153-164, 1987.

Fritts, D.C., and T. Tsuda, Observational evidence of a saturated gravity wave spectrum in the troposphere and lower stratosphere. *J. Atmos. Sci.*, 46, 1741-1759, 1988.

Fukao, S., T. Sato, N. Yamasaki, R.M. Harper and S. Kato, Radar measurement of tidal winds at stratospheric heights over Arecibo. *J. Atmos. Sci.*, 37,2540-2544, 1980.

Hare, F.K., The arctic. *Quart. J. Roy. Meteor. Soc.*, 94, 439-459, 1968.

Haltiner, G.J. and R.T. Williams, *Numerical Prediction and Dynamic Meteorology*, 477 pp, Wiley, New York, 1980.

Haurwitz, B., The geographical distribution of the solar semidiurnal pressure oscillation, *N. Y. Univ. Meteorol. Pap.*, 2(5), 36pp., 1956.

Haurwitz, B., The diurnal surface pressure oscillation, *Arch. Meteorol. Geophys. Bioklimato., Ser.* A., 14, 366-379, 1965.

Haurwitz, B. and A. D. Cowley, The diurnal and semidiurnal barometric oscillations, global distribution and annual variation, *Pure App. Geophys.*, 102, 193-222, 1973.

Holton, J.R., *The dynamic meteorology of the stratosphere and mesosphere, eteorological Monographs*, vol. 15, No. 37, American Meteorological Society, Boston, 218 pp, 1975.

Holton, J.R., *An introduction to dynamic meteorology*, Academic Press, Inc., 391 pp, 1979.

Hoskins, B.J., H.H. Hsu, I.N. James, M. Masutani, P.D. Sardeshmukh and G.H. White, Diagonostics of the global atmospheric circulation based on ECMWF analyses 1979-1989, WCRP - 27, WMO/TD - N0. 326, 1989.

Hsu, H.H., and Hoskins, B.J., Tidal fluctuations as seen in ECMWF data. *Quart. J. Roy. Meteor. Soc.*, 115, 247-1264, 1989.

Hunt, B., and S. Manabe, An investigation of thermal tidal oscillation in the earth's atmosphere using a general circulation model, *Mon. Wea. Rev., 96,* 753-766, 1968.

Iwasaki, T., S. Yamada and K. Tada, A parameterizations scheme of orographic gravity wave drag with two different vertical

partitionings Part I: Impacts on Medium range forecasts, *J. Meteor. Soc. Japan, 67,* 11-27, 1989.

Iwasaki, T., S. Yamada and K. Tada, A parameterizations scheme of orographic gravity wave drag with two different vertical partitionings Part II: Zonally averaged budget analyses based on transformed Eulerian mean method, *J. Meteor. Soc. Japan, 67,* 29-41, 1989.

Joseph, J. H., Calculation of radiative heating in numerical general circulation models. Technical report NO. 1, Dep. of Meteorology, University of California Los Angeles, 60 pp, 1966.

Joseph, J. H., On the calculation of solar radiation fluxes in the troposphere. *Solar Energy*, 13, 251-261, 1970.

Kasahara, A., Various vertical coordinate systems used for numerical weather prediction, *Mon. Wea. Rev., 102*, 509-522, 1974.

Katayama, A., A simplified scheme for computing radiative transfer in the troposphere. Technical report NO. 6, Dep. of Meteorology, University of California Los Angeles, 77 pp, 1972.

Kato, S., *Dynamics of the Upper Atmosphere*, D. Reidel, Dordrecht, 233 pp, 1980.

Kato, S., T. Tsuda and F. Watanabe, Thermal excitation of non-migrating tides. *J. Atmos. Terr. Phys. 44*, 131-146, 1982.

Kitoh, A. and K. Yamazaki, Impact of surface drag of islands in the maritime continent on the atmospheric general circulation. (aubmitted to *J. Meteor. Soc. Japan*), 1990.

Kodaka, T., S. Nagashima and K. Kawabe, Supercomputer HITACHI S-810 array processor system, *SUPERCOMPUTER Class VI System, Hardware and Software,* Ed. S. Fernbach, Elsevier, North-Holland, 1986.

Kockarts, G., Penetration of solar radiation in the Schuman-Runge bands of molecular oxygen, *Mesospheric Models and Related Experiments,* Ed. G. Fiocco, Reidel, Dordrecht-Holland, 160-176, 1971.

Krueger, A. J., The mean ozone distribution from several series of rocket soundings to 52 km at latitudes from 58°S to 64°N, *Pure and Appld. Geophys.*, 106-108, pp. 1272-1280, 1973.

Kung, E. C. and Tanaka, H., Energetics analysis of the global circulation during the special observation periods of FGGE. *J. Atmos. Sci.*, 40, 2575-2592, 1983.

Lacis, A. A., and J. E. Hansen, A parameterization for the absorption of solar radiation in the earth's atmosphere. *J. Atmos. Sci.*, 31, 118-133, 1974.

Levesque, J. M., and J. W. Williamson, *A Guidebook to FORTRAN on SUPERCOMPUTERS, Academic Press, Inc.*, 218 pp, 1989.

Lindzen, R.S., On the theory of the diurnal tide. *Mon. Wea. Rev.*, 94, 295-301, 1966.

Lindzen, R.S., Thermally driven diurnal tide in the atmosphere. *Quart. J. Roy. Meteor. Soc.*, 86, 9707-9714, 1981.

Lindzen, R.S., Turbulence and stress due to gravity wave and tidal breakdown. *J. Geophys. Res.*, 94, 6341-6356, 1989.

Lönnberg P., and A. Hollingsworth, The statistical structure of short range forecast errors as determined from radiosonde data, part II; Covariance of height and wind errors. In p*roceedings of ECMWF Seminar 1984*, Vol. II, 71-124, 1985

McFarlane, N. A., The effect of orographically excited gravity wave drag on the General Circulation of the lower Stratosphere and Troposhere. *J. Atmos. Sci.*, 44,1775-1800, 1987.

Manabe, S., and F. Möller, On the radiative equilibrium and heat balance of the atmosphere, *Mon. Wea. Rev.*, 89, 503-532, 1961.

Masuda, K., Meridional heat transport by the atmosphere and the ocean: analysis of FGGE data. Tellus., 40A, 285-302, 1988.

McClatchey, R. A., R. W. Fenn, J. E. A. Selby, F. E. Volz, and J. S. Goring, Optical properties of the atmosphere, AFCRL 72-0497, 108 pp, 1972.

McElroy, M. B., S. C. Wofsy, J. E. Penner and J. C. McConnell: Atmospheric ozone: Possible impact of stratospheric aviation. *J. Atmos. Sci.*, 31, 287-303, 1974.

Meisner, B. N., and P. Arkin, Spatial and annual variation in the diurnal cycle of large-scale tropical convective cloudiness and precipitation,

Mon. Wea. Rev., 115, 20092032, 1987.

Murgatroyd, R.J., The structure and dynamics of the stratosphere. The Global Circulation of the Atmosphere, G.A. Corby, Ed., London, Roy. Meteor. Soc., 159-195, 1969.

Nagatani, M.N., A.J. Miller, K.W. Johnson and M.E. Gelman: An eight-year climatology of meteorological and SBUV ozone data. NOAA Technical report NWS 40, National Oceanic and Atmospheric Administration, 125 pp, 1988.

Newell, R. E., J. W. Kidson, D. G. Vincent and G. J. Boer, *The General Circulation of the Tropical Atmosphere and Interactions with Extratropical Latitudes*, Vol. 1. The MIT Press, 371 pp., 1972.

Palmer, T. N., G. J. Shuttts and R. Swinbank, Alleviation of a systematic westerly bias in general circulation and numerical weather prediction models through an orographic gravity drag parameterization. *Quart. J. Roy. Meteor. Soc.*, 112, 1001-1039, 1986.

Phillips, N. A., The general circulation of the atmosphere: A numerical experiment. *Quart. J. Roy. Meteor. Soc.*, 82, 123-164 1956.

Phillips, N. A., A coordinate system having some special advantages for numerical forecasting, *J. Meteor., 14*, 184-185, 1957.

Randel, W. J., The evaluation of winds from geopotential height data in the stratosphere. *J. Atmos. Sci.*, 44, 3097-3120, 1987.

Randel, W. J., and B. Boville, Observations of a major stratospheric warmings during December 1987. *J. Atmos. Sci.*, 44, 2179-2186, 1987.

Reed, R.J., M.J. Oard and M. Sieminski, A comparison of observed and theoretical diurnal tidal motions between 30 and 60 km, *Mon. Wea. Rev., 97*, 456-459, 1969.

Rodgers, C. D., The radiative heat budget of the troposphere and lower stratosphere, Planetary Circulation Project, Dep. of Meteorology, MIT, Rep. No. 2, 99 pp, 1967.

Schlesinger, A numerical simulation of the general circulation of atmospheric ozone. *Ph.D. dissertation*, University of California Los Angeles, 1976.

Schlesinger, M.E. and Y. Mintz, Numerical simulation of ozone production, transport and distribution with a global atmospheric general circulation model. *J. Atmos. Sci.*, 36, 1325-1361, 1979.

Schutz, C., and W.L. Gates, Global Climatic Data for Surface, 800 mb, 400 mb: January. R-915-ARPA, The Rand Corporation, Santa Monica, 50 pp, 1971.

Simmons, A.J. and L. Bengtsson, Atmospheric general circulation models: their design and use for climate studies, *The Global Climate*, Ed. J.T. Houghton, Cambridge, 37-62, 1984

Suarez, M.J., A. Arakawa, and D.A. Randall, The Parameterization of the Planetary Boundary Layer in the UCLA General Circulation Model: Formulation and Results. *Mon. Wea. Rev., 111*,2224-2243, 1983.

Tokioka, T., Some considerations on vertical differencing, *J. Meteor. Soc. Japan*, 56, 98-111, 1978.

Tokioka, T. and I. Yagai, On the January simulation of stratospheric circulations with the MRI general circulation model : Preliminary results. *Dynamics of the Middle Atmosphere*, Ed. J. R. Holton and T. Matsuno, Reidel, Dordrecht-Holland, 527-537, 1984.

Tokioka, T. and I. Yagai, Atmospheric tides appearing in a global atmospheric general circulation model *J. Meteor. Soc. Japan*, 65, 423-438, 1987.

Tokioka, T., K. Yamazaki, I. Yagai, and A. Kitoh, A description of the Meteorological Research Institute atmospheric general circulation model (MRI.GCM-I). *Technical Report of the Meteorological Research Institute, No 13*, Meteorol. Res. Inst., Tsukuba, 249 pp., 1984.

Tokioka, T., A. Kitoh, I. Yagai, and K. Yamazaki, A simulation of the tropospheric general circulation with the MRI atmospheric general circulation model Part I: The January performance. *J. Meteor. Soc. Japan, 63*, 749-778, 1985.

Tsuda, T. and S. Kato, Diurnal non-migrating tides excited by a differential heating due to land-sea distribution, *J. Meteor. Soc. Japan, 67*, 43-55, 1989.

Tsuda, T., T. Inoue, D.C. Fritts, T.E. VanZandt, S. Kato, T. Sato, and S. Fukao, MST radar observations of a saturated gravity wave spectrum. *J. Atmos. Sci.*, 46, 2440-2447, 1989.

Tsuda, T., K. Hirose, S. Kato and M.P. Sulzer, Some findings on correlation between the stratospheric echo power and the wind shear observed by the Arecibo UHF radar. *Radio Sci.*, 20, 1503-1508, 1985.

U.S. National Academy of Sciences, *Understanding Climatic Change*, Washington, DC, 239 pp, 1975.

Volland, H., *Atmospheric Tidal and Planetary Waves* . Kluwer Academic Pub., Dordrecht, 348 pp, 1988.

Washington, W.M. and C.L. Parkinson, *An introduction to three-dimensional climate modeling*, 422 pp, Oxford University Press, Oxford-England, 1986.

World Meteorological Organization, The World Weather Watch program 1988-1997 Second WMO long-term plan Part II, volume 1, 252 pp, WMO-No. 691, 1987.

Yagai, I.and T. Tokioka, The effect of increased surface drag over the continents in January.Short- and Medium-range Numerical Weather Prediction, *Collection of Papers* Presented at the WMO/IUGG NWP Symposium, Tokyo, 4-8 August 1986, 409-419, 1987.

Yagai, I. and K. Yamazaki, Effect of internal gravity wave drag on the 12-layer MRI GCM January simulation. CAS/JSC Working Group on Numerical Experimentation, Extended Abstracts of Papers Presented at the WMO Workshop on Systematic Errors in Models of the Atmosphere, Toronto, Canada, 19-23 September 1988, 226- 233, 1988.

Yagai, I. and K. Yamazaki, Stratospheric sudden warmings simulated by the MRI GCM with a gravity wave drag parameterization. to be submitted, 1991.

Yagai, I., Non-migrating thermal tides detected in data analysis and a GCM simulation. *J. Geophys. Res.*, 94, 6341-6356, 1989.

Yamamoto, G., On the radiation chart. Sci. Rept. Tohoku Univ., S. 5, *Geophysics*, 4, 9-23, 1952.

Yamazaki, K.,, A study of the impact of soil moisture and surface albedo changes on global climate using the MRI GCM-I *J. Meteor. Soc. Japan*,

67, 123-146, 1989.

Zwiers, F., and K. Hamilton, Simulation of Solar Tides in the Canadian Climate Centre General Circulation Model. *J. Geophys. Res.*, 91, 11,877-11,896, 1986.